Mechanistic Studies of NO Reduction in Dinuclear Metalloproteins

By

Takahiro Hayashi

A DISSERTATION

Presented to the Division of Environmental and Biomolecular Systems
and the Oregon Health and Science University
School of Medicine
In partial fulfillment of
the requirements for the degree of

Doctor of Philosophy

March 2011

Division of Environmental and Biomolecular Systems
School of Medicine
Oregon Health and Science University

CERTIFICATE OF APPROVAL

This is to certify that the Ph.D. dissertation of
Takahiro Hayashi
has been approved

Pierre Moënne-Loccoz, Ph.D., Dissertation Advisor
Associate Professor

Ninian J. Blackburn, Ph.D.
Professor

Peter Zuber, Ph.D.
Professor

Victoria J. DeRose, Ph.D.
Professor, University of Oregon

TABLE OF CONTENTS

LIST OF TABLES

LIST OF FIGURES

ACKNOWLEDGEMENTS

I would like to begin with thanking my research advisor, Dr. Pierre Moënne-Loccoz for his patience, advice, and support during my graduate studies. My achievements during graduate school would have been impossible without him. Further, outside of the laboratory, his hospitality and friendship were greater than I ever could have expected. I would also like to thank Erik Yukl for his helpful discussions and great friendship. I also wish to thank Drs. Nobuhumi Nakamura and Michiko Nakano for their guidance and hospitality.

My research in the Moënne-Loccoz lab would have been impossible without our collaborators in the group of Profs. James Fee (The Scripps), Donald Kurtz Jr. (UTSA), Yi Lu (UIUC), Bob Gennis (UIUC), Simon de Vries (Delft), Michiko Nakano (OHSU), Stephen Lippard (MIT), David Goldberg (JHU), Paul Ortiz de Montellano (UCSF), and Mario Rivera (UK). They have been amazing collaborators throughout my graduate studies and definitely influenced my career. I am also grateful to Profs. Pierre Moënne-Loccoz, Peter Zuber, James Whitterker, and Ninian Blackburn as well as the entire faculty of the Division of Environmental and Biomolecular systems, for their instructions in biochemistry and molecular biology. I must also thank my committee members, Profs. Pierre Moënne-Loccoz, Ninian Blackburn, Peter Zuber, and Victoria DeRose for carefully reviewing my dissertation. Finally, I wish to thank my family and friends for their emotional supports during my graduate studies.

ABSTRACT

Mechanistic Studies of NO Reduction in Dinuclear Metalloproteins

Takahiro Hayashi, B.S.

Doctor of Philosophy
Division of Environmental and Biomolecular Systems within
School of Medicine, Oregon Health and Science University

March 2011
Thesis Advisor: Pierre Moënne-Loccoz

The ultimate goal of this research is to define the mechanisms by which metalloproteins reduce NO to N_2O. This reaction is an obligate step in bacterial denitrification, and it also provides microorganisms resistance to nitrosative stresses. We have characterized two prominent families of enzymes that catalyze this reaction.

Terminal oxidases are members of heme/copper oxidase superfamily and are evolutionally related to denitrifying heme/non-heme NO reductase enzymes (NORs). Despite differences in recognized function and active site metal composition, these enzymes exhibit cross reactivity with NORs showing oxidase activity and several terminal oxidases capable of reducing NO to N_2O. Here, we use low temperature photolysis combined with UV-vis, FTIR, resonance Raman (RR), and EPR spectroscopies to determine how NO interacts with the metal centers of cytochrome ba_3 from *Thermus thermophilus*, bo_3 from *Escherichia coli*, and bioengineered models of NORs in myoglobin scaffold. Our results show that in all cases, the first NO molecule binds to the heme iron(II) and that the binding of a second NO to the distal metal center is not an essential step of the NO reductase activity. Indeed, while a side-on copper-nitrosyl complex can be trapped in ba_3, none of the enzymes studied show the formation of an end-on distal metal-NO complex. Thus, the role of the distal metal center is proposed to be limited to the stabilization of a heme-hyponitrite species via electrostatic interaction.

This NO reduction mechanism is described as a *cis*-heme reaction route and is supported by theoretical calculations.

We also investigated the NO reductase activity of flavodiiron proteins (FDPs) using UV-vis, FTIR, RR, and EPR spectroscopies. The close vicinity of the flavin mononucleotide cofactor (FMN) to the diiron site has led to the proposal of a super-reduction mechanism where $[Fe^{II}\text{-}NO]_2$ complex is reduced by FMN. To distinguish the role that FMN and diiron center play in catalysis, we prepared an FMN-free FDP (deflavo-FDP). Our experiments show that the reduced diiron center in deflavo-FDP is capable of a single reducing turnover of NO to N_2O. Furthermore, stoichiometric addition of NO to the reduced deflavo-FDP as well as holo-FDP results in the formation of a diiron-mononitrosyl complex $Fe^{II} \bullet Fe^{II}\text{-}NO$ as the first intermediate in the catalysis. These results support a catalytic route for NO reductase in FDPs where the diiron site reduces NO to N_2O and the role of the FMN cofactor is to reduce the oxidized diiron site.

CHAPTER 1
NO DETOXIFICATION BY METALLOPROTEINS

1.1 NO detoxification in biology

Nitric oxide (NO) is a gaseous molecule that plays important roles in a number of physiological processes, including vasodilatation, neurotransmission, and host immune response to infection (Marletta and Spiering, 2003). NO is also an intermediate species during denitrification, a process catalyzed by denitrifying microorganisms in which nitrate and nitrite are converted to dinitrogen gas (eq. 1.1) (Watmough *et al.*, 1999).

$$NO_3^- \rightarrow NO_2^- \rightarrow NO \rightarrow N_2O \rightarrow N_2 \qquad \text{(eq 1.1)}$$

NO contains an unpaired electron, making it a free radical species. Although NO is not very reactive toward most biomolecules, it reacts rapidly with transition metals and other radicals such as superoxide (O_2^-) (Beckman and Koppenol, 1996). The ability of NO to form stable complexes with metalloproteins can lead to pathological effects. For example, cytochrome c oxidase (CcO) is known to react with NO to form a stable nitrosyl complex, resulting in inhibition of the cellular respiration system (Brunori *et al.*, 2006). Reaction of NO with O_2^- forms peroxynitrite ($OONO^-$), a highly toxic oxidant which causes nitration of lipid, DNA, and proteins (Goldstein and Merenyi, 2008).

In vivo, NO is formed either by NO synthase (NOS), which converts the amino acid arginine to citrulline and NO (Alderton *et al.*, 2001), or by the denitrifying enzyme nitrite reductase (NIR), which reduces NO_2^- to NO (Averill, 1996). Some bacteria are regularly exposed to NO either as it is produced by the inducible NOS (iNOS) of the host immune response, or as NO is release by the nitrogen cycle. In response, bacteria have developed a variety of defensive mechanisms in order to prevent build-up of toxic concentration of NO and formation of peroxynitrite species (Chakravortty and Hensel, 2003). One way to efficiently remove NO from the environment is to detoxifying NO by converting it to none-reactive species, either nitrate (NO_3^-) or nitrous oxide (N_2O) via NO dioxygenation or NO reduction, respectively.

The cellular conversion of NO to nitrate under aerobic conditions is mediated by the *hmpA*-encoded protein flavohemoglobin as well as other hemoglobin-like proteins (Gardner *et al.*, 1998; Cruz-Ramos *et al.*, 2002). These proteins contain a heme cofactor which binds dioxygen (O_2) to form a stable heme-superoxo species. Like superoxide, the heme-superoxo reacts very efficiently with NO to quantitatively produce NO_3^- and Fe^{3+} heme according to eq. 1.2.

$$NO + Fe^{II}\text{-}O_2 \rightarrow NO_3^- + Fe^{III} \qquad \text{(eq. 1.2)}$$

Under anaerobic condition, on the other hand, NO is converted to N_2O via an NO reductase reaction (eq. 1.3).

$$NO + 2\ H^+ + 2\ e^- \rightarrow N_2O + H_2O \qquad \text{(eq. 1.3)}$$

This reaction is mediated by two families of enzymes: 1) *norB*-encoded heme/non-heme NO reductases (NORs) and heme-copper terminal oxidases (HCOs) (Householder *et al.*, 2000; Stevanin *et al.*, 2005), and 2) *norV*-encoded flavodiiron proteins (FDPs) (Gardner and Gardner, 2002; Gardner *et al.*, 2002). This thesis focuses on these anaerobic NO detoxifying systems.

1.2 NO reductase enzymes

The NO reductase enzymes NORs, HCOs, and FDPs share no structural homology. In fact, NORs and HCOs are integral membrane proteins (Wasser *et al.*, 2002) whereas FDPs are cytoplasmic soluble proteins (Kurtz, 2007). Despite these structural differences, these enzymes have in common a dinuclear metal active site, where the reduction of two NO molecules to N_2O takes place (Girsch and de Vries, 1997; Frazao *et al.*, 2000; Soulimane *et al.*, 2000). Additionally, these enzymes are also capable of catalyzing the four electron reduction of O_2 to H_2O (Fujiwara and Fukumori, 1996; Butler *et al.*, 2002; Gomes *et al.*, 2002). While NORs and HCOs possess heme/non-heme and heme/copper dinuclear metal center (Wasser *et al.*, 2002), FDPs possess symmetric carboxylate bridged non-heme diiron center (Frazao *et al.*, 2000). Metal-metal distances in heme/non-heme diiron and heme/copper centers have been observed to range between ≤3.5 and 5.1 Å (Moënne-Loccoz *et al.*, 2000; Soulimane *et al.*, 2000; Liu *et al.*, 2009) and between 3.2 and 3.6 Å in the non-heme diiron center of FDPs (Di Matteo *et al.*, 2008). These variations in the metal-metal distances reflect the oxidation and ligation

states of the dinuclear metal clusters, and in all cases the two metals show evidence of magnetic coupling which renders their characterization by magnetic spectroscopic more complex (Girsch and de Vries, 1997; Silaghi-Dumitrescu *et al.*, 2003).

1.2.1 Heme-copper oxidases (HCOs) and NO reductases (NORs)

Introduction

Heme-copper oxidases (HCOs) are terminal oxidases present in the respiratory chain of bacteria and eukaryotic mitochondria. HCOs utilize O_2 as terminal electron acceptor and catalyze the four electron reduction of O_2 to H_2O to generate a proton gradient that is used for ATP production (eq. 1.4 and Figure 1.1).

$$O_2 + 8\ H^+_{in} + 4\ e^- \rightarrow 2\ H_2O + 4\ H^+_{out} \qquad \text{(eq. 1.4)}$$

NO reductases (NORs) are evolutionarily related to heme-copper oxidases but their role is to reduce NO to N_2O as part of the respiratory chain of denitrifying bacteria. While the reduction of O_2 by HCOs is electrogenic, i.e., that the chemical reaction generates an electrochemical gradient across the membrane, the reduction of NO by NOR is not, presumably as coupled proton pumping is lacking and the two electrons and two protons involved in the reaction originate from the same side of the membrane (Wasser *et al.*, 2002).

Despite their difference in recognized function, NORs and HCOs exhibit cross reactivity with NORs showing oxidase activity and several terminal oxidases (i.e., cytochrome ba_3, bo_3, and cbb_3) being capable of reducing NO to N_2O (Fujiwara and Fukumori, 1996; Butler *et al.*, 2002). The NO reductase activity of HCOs is significantly lower than that of denitrifying NORs (Table 1.1), and thus, this activity may not have physiological relevance. In contrast, the oxidase activity of denitrifying NO reductases found in some pathogenic bacteria, such as *Pseudomonas aeruginosa*, *Neisseria gonorrhoeae*, and *Neisseria meningitidis*, have been proposed to play an important roles in microbial infections as these microorganisms adaptation from aerobic to anaerobic respiration (Householder *et al.*, 2000; Anjum *et al.*, 2002; Hassett *et al.*, 2002). Furthermore, the levels of expression of the NORs are upregulated by exposure to NO

and provide resistance to the mammalian immune response (Householder *et al.*, 2000; Anjum *et al.*, 2002; Stevanin *et al.*, 2005).

Table 1.1. NO reductase activity of HCOs and NORs

Type of enzyme	**Organism**	**NOR activity[*] / mol NO/mol [E] • min**
NOR (cNOR)	*P. denitrificans*	~1400
cbb_3	*P. stutzeri*	20
ba_3	*T. thermophilus*	0.5
bo_3	*E. coli*	0.3
aa_3	Bovine	ND[†]
aa_3	*R. sphaeroides*	ND[†]

[*]NOR activity at [NO] = 5 μM. [†]Not detected.

Crystal structures

Although X-ray crystal structures are available for many of HCOs, including the mitochondrial aa_3-type (Figure 1.1) (Tsukihara *et al.*, 1996), bacterial aa_3-type from *P. denitrificans* (Iwata *et al.*, 1995) and *R. sphaeroides* (Svensson-Ek *et al.*, 2002), the ba_3-type from *T. thermophilus* (Soulimane *et al.*, 2000), the bo_3-type from *E. coli* (Abramson *et al.*, 2000), and the cbb_3-type from *P. stutzeri* (Buschmann *et al.*, 2010), there is no X-ray crystal structure or NMR solution structure currently available for bacterial NORs. Nevertheless, sequence alignments, hydropathy plots, and homology modeling have predicted that the major subunit common for all the NORs, norB, is structurally homologous to subunit I of HCOs (Wasser *et al.*, 2002; Reimann *et al.*, 2007).

All the six histidine residues that ligate the metal centers in HCOs (two axial His of the low-spin heme, one axial His of the high-spin heme, and three His of Cu_B) are consistently conserved in NORs. These histidines are presumed to coordinate the low-spin heme-*b*, the high-spin heme-b_3, and the non-heme iron Fe_B center in place of Cu_B. In HCOs, a strictly conserved tyrosine residue covalently attached to one of the three histidines of Cu_B is thought to play both structural and functional roles in O_2 reduction (Figure 1.1), as Tyr-variants in bacterial aa_3 and bo_3 HCOs show altered histidine ligation

to the high-spin heme and loss of Cu_B (Thomas *et al.*, 1994; Das *et al.*, 1998). Consequently, these mutants exhibit less than 1 % of the wild-type activity (Mogi *et al.*, 1998). The cross-link tyrosine has also been proposed to form a radical as it participates in electron transfer and O-O bond cleavage during catalysis (Proshlyakov *et al.*, 2000).

In NORs, several conserved glutamate residues have been predicted to locate in the vicinity of the catalytic diiron active site. Mutation of the conserved glutamate residues does not affect enzyme stability or cofactor composition but the variants retain less than 5% of NO reductase activity (Butland *et al.*, 2001). These observations suggest that the glutamate residues might serve as additional ligands to the non-heme Fe_B center and/or proton donor during catalysis. Computational calculations also support the participation of glutamate in the coordination sphere of Fe_B, as an octahedral coordination with three histidines, one glutamate, and one water molecule, provides more energetically feasible reaction coordinates than a tetrahedral coordination with three histidines (Blomberg *et al.*, 2006).

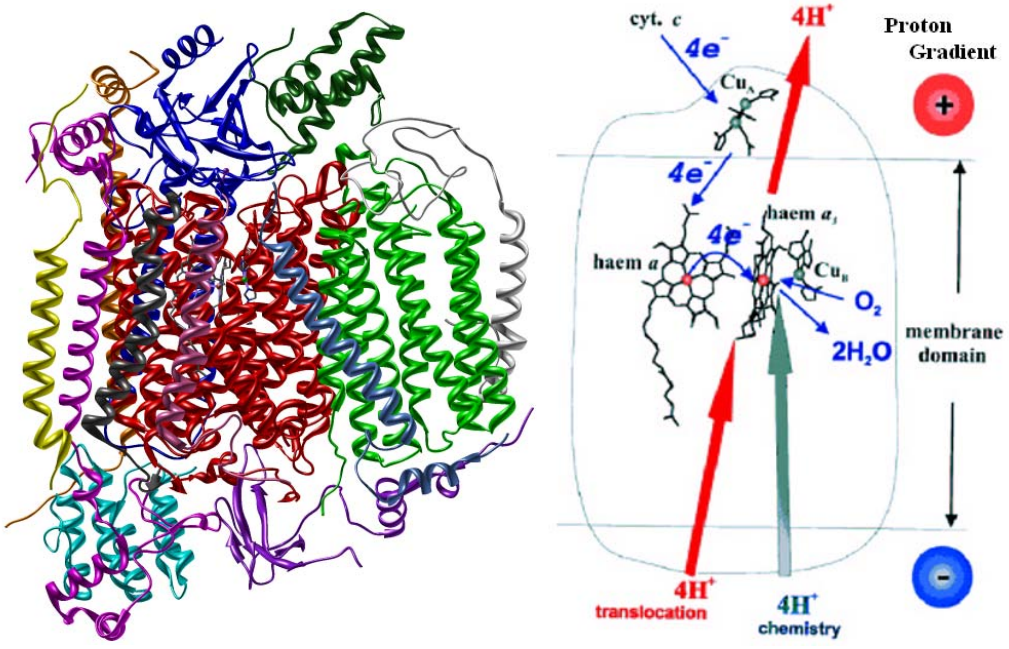

Figure 1.1 Overall structure (left) and the metal cofactors (Cu_A center, low-spin heme, and high-spin heme/copper center) (right) of bovine heart cytochrome *c* oxidase (PDB code: 2DYR).

1.2.2 Flavodiiron proteins (FDPs)

Introduction

The other family of enzymes that play a dominant role in NO detoxification is that of flavodiiron proteins (FDPs) (Saraiva *et al.*, 2004). FDPs are widespread among bacteria, archaea, and some protozoan pathogens, and their roles have been shown to protect these microorganisms against nitrosative as well as oxidative stresses by reductively scavenging NO and O_2 according to Figure 1.2 (Gardner *et al.*, 2002; Gomes *et al.*, 2002; Kurtz, 2007; Di Matteo *et al.*, 2008).

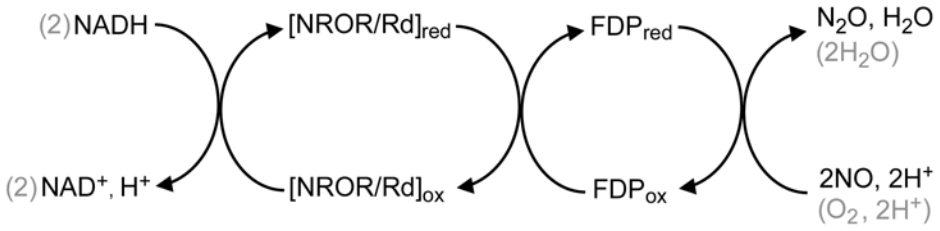

Figure 1.2 Schematic representation of electron transfer chain coupling NADH oxidation to O_2 or NO reduction by FDP. Rd; rebredoxin, NROR; NADH: rubredoxin oxidoreductase.

Turnover numbers for NO reduction are comparable in several FDPs to those reported for denitrifying NORs (Gomes *et al.*, 2002; Silaghi-Dumitrescu *et al.*, 2003). The relative levels of NADH:O_2 reductase vs NADH:NO reductase activities (at saturating NROR/Rd) vary significantly among FDPs, but these variations have yet to be correlated with specific structural features (Kurtz, 2007). This bifunctionality exhibited by FDPs is reminiscent of the cross-reactivity observed with HCOs and NORs.

Crystal structures

FDPs are soluble cytoplasmic enzymes that are unrelated to the membrane-bound denitrifying NORs. The minimum functional unit of all structurally characterized FDPs is a ‘head-to-tail’ homodimer (Figure 1.3) (Frazao *et al.*, 2000; Silaghi-Dumitrescu *et al.*, 2005; Di Matteo *et al.*, 2008). The N-terminal domain of each subunit contains a non-

heme diiron site (Fe1-Fe2 distance 3.2-3.6 Å), while the C-terminal domain binds a flavin mononucleotide (FMN) cofactor ~5 Å away from the diiron site in the opposite subunit (Figure 1.3). In almost all structurally characterized FDPs, each iron of the diiron site contains two histidine ligands and one terminal monodentate carboxylate ligand from either aspartate or glutamate. Bridging aspartate carboxylate and oxo/hydroxo ligands complete the diiron coordination sphere resulting in two 5-coordinate irons. While the diiron sites of FDPs are reminiscent of those of the non-heme carboxylate-bridged diiron proteins, including subunit R2 of ribonucleotide reductase (Nordlund *et al.*, 1990; Voegtli *et al.*, 2003), the hydroxylase component of soluble methane monooxygenase (MMOH) (Rosenzweig *et al.*, 1993; Whittington and Lippard, 2001), and the Δ^9-stearoyl-acyl carrier protein desaturase (Δ9D) (Lindqvist *et al.*, 1996), there is no detectable amino acid sequence homology between any of these latter enzymes and FDPs.

An obvious inference from the structures is that diatomic substrate O_2 or NO diffuses into this pocket and binds to the sixth iron coordination sites during enzymatic turnover. Minimal O_2R and NOR mechanisms would involve formation of diferrous-substrate complexes which lead to reductive formation of either water from O_2 or N_2O from NO.

Figure 1.3 Overall structure (left) and zoom-in on the diiron center (right) of FDP from *Moorella thermoacetica* (PDB code: 1YCF).

1.3 Metal-nitrosyl chemistry

As mentioned above, NO-detoxification is mediated by metalloproteins that contain iron and copper ions. The reaction of NO with these metals has been the subject of intense investigation as NO has been used as an O_2 analog to study the O_2-chemistry of iron- and copper-containing enzymes and model complexes. Under ambient conditions, NO usually binds to these metals in an N-terminal fashion (i.e., M-N-O), although side-on geometry (η^2-NO) has also been observed (Tocheva *et al.*, 2004; Antonyuk *et al.*, 2005). The binding of NO to a metal involves donation of electron density from the σ-orbital of the N atom lone pair to the metal d-orbitals (σ-bonding) and back-donation from the metal d-orbitals to the π^*-orbitals of the NO group (back-bonding). According to the notion of Enemark and Feltham, the principle bonding scheme of metal-nitrosyl complexes are expressed as $\{M(NO)_n\}^x$, in which *n* is the number of NO group(s) and *x* the number of electrons associated with the metal d- and NO π^*-orbitals (Enemark and Feltham, 1974).

Iron-nitrosyl complexes may exist as $\{FeNO\}^6$, $\{FeNO\}^7$, or $\{FeNO\}^8$ and may correspond to $Fe^{II}(NO^+)$, $Fe^{II}(NO^\bullet)$, or $Fe^{II}(NO^-)$ electronic structure, respectively. Changes in the electronic structure of $\{FeNO\}^7$ species, for example, may vary between $[Fe^{III}\text{-}NO^-] \leftrightarrow [Fe^{II}\text{-}NO^\bullet] \leftrightarrow [Fe^{I}\text{-}NO^+]$ configurations. Most non-heme $\{FeNO\}^7$ are Fe^{III} high-spin species with electron transfer to the NO group which adopts an NO^- electronic structure with two unpaired π^* electrons (Zhang *et al.*, 1992; Brown *et al.*, 1995). On the other hand, heme $\{FeNO\}^7$ are exclusively low-spin species and described as heme Fe^{II} coordinated by $NO^\bullet$ (radical), thus formulated as $[Fe^{II}\text{-}NO^\bullet]$ (Li *et al.*, 2002). An $[Fe^{I}\text{-}NO^+]$ extreme has not been reported yet, but recent experimental and theoretical data suggest that 5-coordinate heme $\{FeNO\}^7$ species exhibit some $[Fe^{I}\text{-}NO^+]$ character (Praneeth *et al.*, 2005; Praneeth *et al.*, 2006). These different electronic structures of $\{FeNO\}^7$ will lead to very different spectroscopic properties, and most importantly, different reactivities. Thus, a clear definition of electronic structures of iron-nitrosyl species would be important to elucidate NO reduction mechanisms.

The two-electron reduction of NO to N_2O by metalloproteins involves binding of two NO molecules to active site followed by the N-N bond formation between the two NO units as the central step of catalysis. The NO reduction mechanism for fungal

cytochrome P450 NO reductase (P450nor) is well defined. This protein contains a heme cofactor which binds NO to form a stable heme $\{FeNO\}^6$ species as the first intermediate. In the presence of reducing agents, the $\{FeNO\}^6$ species undergoes two electron reduction to form $\{FeNO\}^8$ which can then react with NO to quantitatively produce N_2O, H_2O, and Fe^{III} heme according to eq. 1.5 (Shiro *et al.*, 1995; Obayashi *et al.*, 1998).

$$Fe^{III}\text{-}NO + NADH + NO + H^+ \rightarrow N_2O + H_2O + Fe^{III} + NAD^+ \qquad \text{(eq. 1.5)}$$

On the basis of spectroscopic data, the electronic structure of the $\{FeNO\}^8$ species is described as $[Fe^{II}\text{-}NO^-]$, and thus the bound-nitrosyl provides the nucleophile for N-N bond formation.

The NO reduction mechanisms for dinuclear metal metalloproteins are yet to be defined. Alternative pathways for the N-N bond formation in dinuclear metal centers include 1) electrophilic attack on metal bound NO^- by the other NO molecule as seen in P450nor, and 2) coupling of two metal-bound NO neutral radicals. The possible reaction mechanisms for HCOs, NORs, and FDPs are discussed below.

1.4 Putative reaction mechanisms for NO reductase enzymes

1.4.1 Heme-copper oxidases (HCOs) and NO reductases (NORs)

Three possible mechanisms are proposed for HCOs and NORs; *trans*-, *cis*-M_B, and *cis*-heme mechanisms (Figure 1.4). Experimental and theoretical studies have brought some support to all three mechanisms in NOR. In the *trans*-mechanism, the catalytic cycle is initiated by the binding of one NO molecule to each metal center to form a *trans*-dinitrosyl complex. The close proximity of the two metal-nitrosyl species facilitate the formation of N-N bond via an electrophilic attack to form a hyponitrite species ($N_2O_2^{2-}$) bridged between the two metal centers. Several experimental observations support this reaction mechanism. Shiro and coworkers have shown that fully reduced cNOR reacts with NO in a submilisecond time scale and observed appearance of EPR signals characteristics of $S = 1/2$ low-spin heme $\{FeNO\}^7$ and $S = 3/2$ non-heme $\{FeNO\}^7$ species (Kumita *et al.*, 2004). Furthermore, using CO as an analog for NO,

Moënne-Loccoz and coworker reported the characterization of an [heme-CO • OC-Fe_B] ternary complex at the active site of *B. azotoformans* qCu_ANOR (Lu *et al.*, 2004).

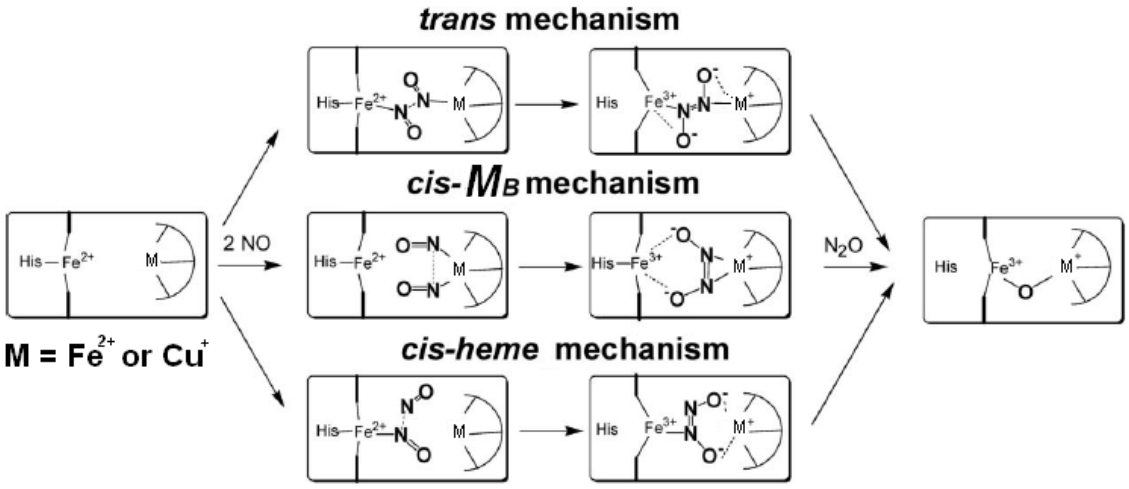

Figure 1.4 Putative NO reduction mechanisms in heme/non-heme iron or heme/copper dinuclear metal center. Adapted from (Moënne-Loccoz, 2007).

The *cis*-M_B mechanism is supported by the observation that NO can be reduced to N_2O by free Fe^{II} ion in the presence of reduction agents, such as ascorbic acid (Zumft and Frunzke, 1982). Additionally, formation of non-heme iron-dinitrosyl $\{Fe(NO)_2\}$complexes have been observed in some non-heme iron containing proteins (Gomes *et al.*, 2000; Cruz-Ramos *et al.*, 2002; D'Autreaux *et al.*, 2004; Strube *et al.*, 2007). In this model, the role of heme iron would be limited to electron transfer site for the non-heme iron active site.

In the *cis*-heme mechanism, the first NO binds to the heme iron(II) to form a heme-nitrosyl $\{FeNO\}^7$ complex and is partially reduced to a more nitroxyl anion character, which activates it toward an electrophilic attack by the second NO molecule (Blomberg *et al.*, 2006). The product of this reaction is a hyponitrite species bridged between the two metal centers analogous to that of the *trans*-mechanism. This reaction mechanism is reminiscent of that proposed for fungal P450nor, where an initial $\{FeNO\}^6$ complex is reduced to a $\{FeNO\}^8$ intermediate by the reducing power of NADH, which then react with the second NO to yield a hyponitrite species, followed by N_2O and H_2O production (Shiro *et al.*, 1995; Obayashi *et al.*, 1998).

The catalytic mechanism of NO reduction in HCOs is generally considered to be initiated by the binding of NO to the high-spin heme in the fully reduced enzyme, forming an $S = 1/2$ low-spin heme $\{FeNO\}^7$. Subsequent steps are expected to involve Cu_B^I, either as a coordination site for a second NO molecule (the *trans*-mechanism) or as an electron donor and electrostatic partner to a heme-hyponitrite complex (the *cis*-heme mechanism). The ability of Cu_B to bind NO in either a stable or transient fashion has been demonstrated in bovine cytochrome *c* oxidases (Zhao *et al.*, 1994; Pilet *et al.*, 2007), ba_3 from *Thermus thermophilus* (Pilet *et al.*, 2004), and bo_3 from *Escherichia coli* (Butler *et al.*, 1997). Further, Varotsis and coworkers have shown that exposure of saturated NO to fully oxidized ba_3 result in formation of a hyponitrite ion ($HONNO^-$) bridged heme/copper species, which is seemingly an intermediate species in the *trans*-mechanism (Varotsis *et al.*, 2007). Although the theoretical calculation by Varotsis and coworkers have proposed formation of a *trans*-dinitrosyl complex as an intermediate of the reaction (Ohta *et al.*, 2006), similar theoretical work by Blomberg and coworkers favor a *cis*-heme mechanism (Blomberg *et al.*, 2006).

Clearly, the mechanisms of NO reduction by HCOs and NORs are matters of debate. Defining these mechanisms will require strategies that combine multiple spectroscopic techniques. In chapter 3 and 4, we will present mechanistic study of NO reductase reactions in HCOs. More specifically, low temperature photolysis is employed to investigate chemical behaviors of NO in heme/copper centers of cytochrome ba_3 and bo_3. Using the same technique, we will describe the manner in which NO interacts with heme/non-heme diiron center of NOR models in Chapter 5.

1.4.2 Flavodiiron proteins (FDPs)

While only two electrons are required to complete the reduction of NO to N_2O, fully reduced FDPs have four electron equivalents (two from the diiron center and two from the FMN cofactor). Several mechanisms have been proposed for FDPs (Figure 1.5) (Silaghi-Dumitrescu *et al.*, 2005; Kurtz, 2007). Kinetic studies predict cooperative binding of two NO molecules at the enzyme active site (Silaghi-Dumitrescu *et al.*, 2005), but more data will be needed to exclude some of the mechanistic models described below.

The 'diferrous-dinitrosyl', 'hyponitrite', and 'iron-dinitrosyl' mechanisms (Figure 1.5-1, 2, and 3) are reminiscent of '*trans*', '*cis*-heme', and '*cis*-M_B' mechanisms proposed for NORs, respectively (Figure 1.4). A computational study by Siegbahn et al. supports the 'hyponitrite' mechanism for FDP, where a ferrous iron-nitrosyl reacts with a second NO, leading to a diferric-hyponitrite species (Figure 1.5-2) (Blomberg *et al.*, 2007). In these reaction mechanisms, the proximal FMN cofactor is not directly involved into the catalysis; its role is only limited to re-reduction of the diiron site back to diferrous after its oxidation to the diferric state by two NO molecules. In the 'super-reduced' mechanism (Figure 1.5-4), however, the FMN cofactor plays a more integral role in the catalytic turnover; a diferrous-dinitrosyl precursor is super-reduced to a diferrous-dinitroxyl intermediate species (i.e., $[\{FeN(H)O\}^8]_2$) by the reducing power of $FMNH_2$.

Reactivity of diiron centers with NO has been investigated in some of the non-heme carboxylate-bridged diiron proteins, such as MMOH, R2, hemerythrin (Hr), and NorA, a NO-binding diiron protein, but none of these proteins exhibits significant NOR activity (Nocek *et al.*, 1988; Haskin *et al.*, 1995; Coufal *et al.*, 1999; Strube *et al.*, 2007). In fact, these diiron centers have been shown to react with NO to form stable iron-nitrosyl complexes, i.e., $[\{FeNO\}^7]_2$ in MMOH and R2, $[Fe\text{-}\{Fe(NO)_2\}^{10}]$ in NorA, and $[Fe\text{-}\{FeNO\}^7]$ in Hr. The reasons for this striking difference in reactivity towards NO in apparently similar non-heme diiron proteins are yet to be elucidated. The catalytic NO-reductase efficiency of FDPs might be due to the presence of the proximal FMN cofactor which can provide reducing equivalents to a diferrous-dinitrosyl complex as in the 'super-reduced' mechanism. The reduction potential of the high-spin non-heme $\{FeNO\}^7/\{FeN(H)O\}^8$ couple have not been reported yet, however, in heme proteins (Lin *et al.*, 2000) and octahedral non-heme iron complexes (Serres *et al.*, 2004; Montenegro *et al.*, 2009) the reduction potential of low-spin $\{FeNO\}^7/\{FeN(H)O\}^8$ couples range from -1.4 to -0.6 V. The redox potential of free FMN is -0.2 V but it is always lowered by interaction with the protein matrix, with the lowest value reported at ~-0.5 V in flavodoxins (Barman and Tollin, 1972).

Evaluating the super-reduced mechanism using a flavin-free form of FDP is the subject of chapter 6. Specifically, we will present the first evidence that the diiron center

of a flavin-free FDP reacts with one NO molecule to form a diiron-mononitrosyl species which can react with a second NO molecule to produce N_2O. These results suggest that the NO reduction in FDPs might proceed via the hyponitrite mechanism (Figure 1.5-2).

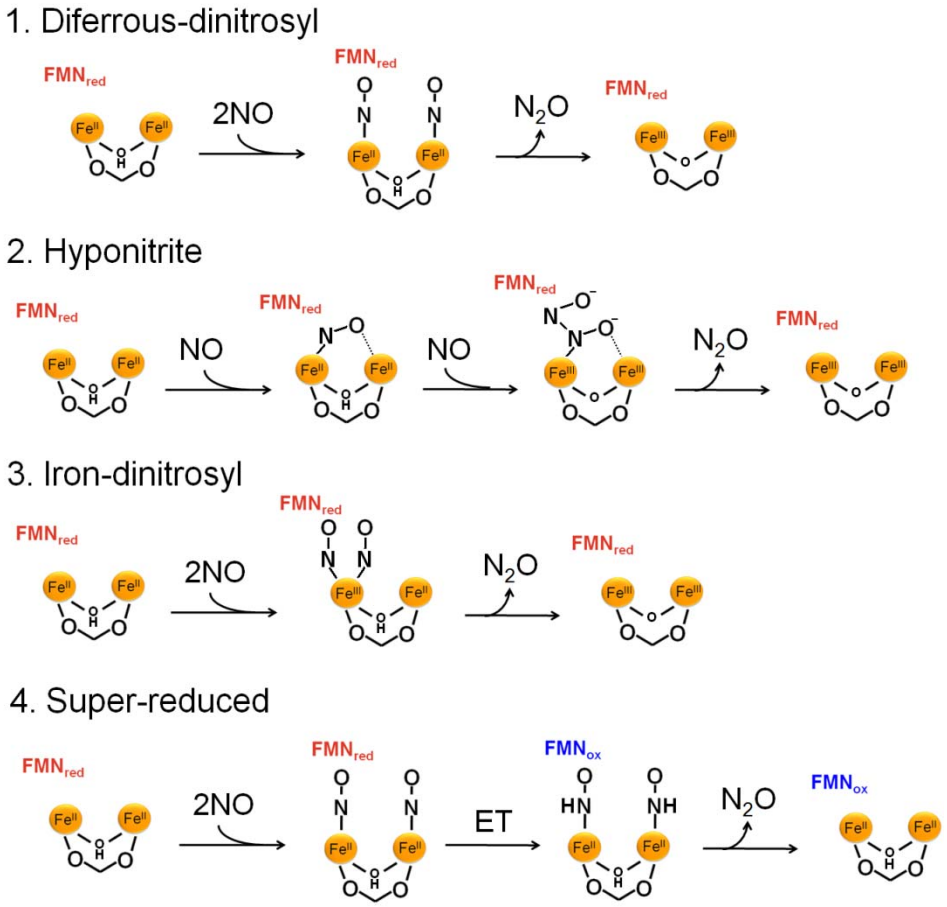

Figure 1.5 Proposed NO reduction mechanisms in flavodiiron proteins. Adapted from (Kurtz, 2007).

CHAPTER 2
SPECTROSCOPIC CHARACTERIZATION OF METAL-NITROSYL COMPLEXES

2.1 Molecular spectroscopy

A variety of spectroscopic methods have been used to define the molecular and electronic structures of metal-nitrosyl complexes. Unlike synthetic model compounds, which contain a limited number of atoms, metalloproteins consist of a large number of atoms and are typically available at limited concentrations in aqueous solutions. Here we will discuss spectroscopic approaches used to selectively study metal-nitrosyl species formed within the complexity of NO reductase enzymes.

2.1.1 UV-vis absorption and EPR spectroscopy

Hemoproteins

Heme and other iron-porphyrin complexes exhibit characteristic intense visible absorption near 400 nm known as Soret or γ band; weaker absorption bands below 500 nm are known as Q or α/β bands. These absorption features are primarily due to $\pi \rightarrow \pi^*$ electronic transition of the porphyrin macrocycle but the absorption maxima and intensity of these bands are sensitive to the heme iron oxidation state, spin state, coordination number as well as the type of ligand present at the 5th and 6th coordination sites and the heme pocket environment. Although UV-vis spectra of heme are rarely straightforward to interpret, changes due to ligand binding or other alterations of heme environment are easily reported by these spectra.

Unlike O_2 and CO, NO can coordinate to both Fe^{II} and Fe^{III} hemes to form $\{FeNO\}^7$ and $\{FeNO\}^6$ complexes. All $\{FeNO\}^6$ species reported for hemoproteins are 6-coordinate low-spin (6cLS) (Ding *et al.*, 1999), with Soret absorbance at ~420 nm and split α/β bands at ~530 and ~575 nm (Figure 2.1). The $\{FeNO\}^6$ species are EPR silent as a result of either antiferromagnetic coupling of $S = 1/2$ low-spin Fe^{III} heme with $S = 1/2$

$NO^{\bullet}$ or an $S = 0$ low-spin Fe^{II} heme coordinate by $S = 0$ NO^{+}, both of which give a total electron spin of $S = 0$.

The Fe^{II}-nitrosyl $\{FeNO\}^7$ species can exist as a 6-coordinate low-spin (6cLS) or 5-coordinate low-spin (5cLS) species. This difference in coordination number in $\{FeNO\}^7$ species is easily detected by UV-vis and EPR spectroscopy. While 6cLS heme $\{FeNO\}^7$ species display the Soret absorbance at ~420 nm, 5cLS species show blue-shifted Soret at ~400 nm (Figure 2.1) (Decatur *et al.*, 1996). Both 6- and 5-coordinate heme $\{FeNO\}^7$ are $S = 1/2$ system and thus exhibit EPR signals at $g \sim 2$. However, they show distinct hyperfine splitting due to interaction of the electronic spin with the ^{14}N nucleus (nuclear spin quantum number, $I = 1$) of the NO ligand and a *trans* N-ligand. 5cLS species exhibit a 3-line hyperfine structure with hyperfine coupling constant (A_{HF}) of ~17 G due to the NO ligand (Wayland and Olson, 1974) (Figure 2.1). In contrast, 6cLS species typically exhibit a 9-line hyperfine structure with hyperfine coupling constant (A_H) of ~22 G and superhyperfine coupling constant (A_{SHF}) of ~6 G due to the NO ligand and a *trans* N-ligand, such as histidine, respectively (Maxwell and Caughey, 1976) (Figure 2.1).

Preparation of a stable heme $\{Fe(H)NO\}^8$ species have been reported in Mb either by one electron reduction of $\{FeNO\}^7$ species or by addition of nitroxyl (HNO) to Fe^{II} heme (Sulc *et al.*, 2004). As $\{FeNO\}^6$ species, $\{FeNO\}^8$ are diamagnetic and show no EPR signal. The electronic absorption spectra of $\{FeNO\}^8$ species observed in myoglobin are nearly identical to those of 6cLS heme $\{FeNO\}^7$ or $\{FeNO\}^6$ (Figure 2.1). Therefore, characterization of these diamagnetic iron-nitrosyl species requires additional spectroscopies, such as vibrational spectroscopy, which will be discussed later in this chapter.

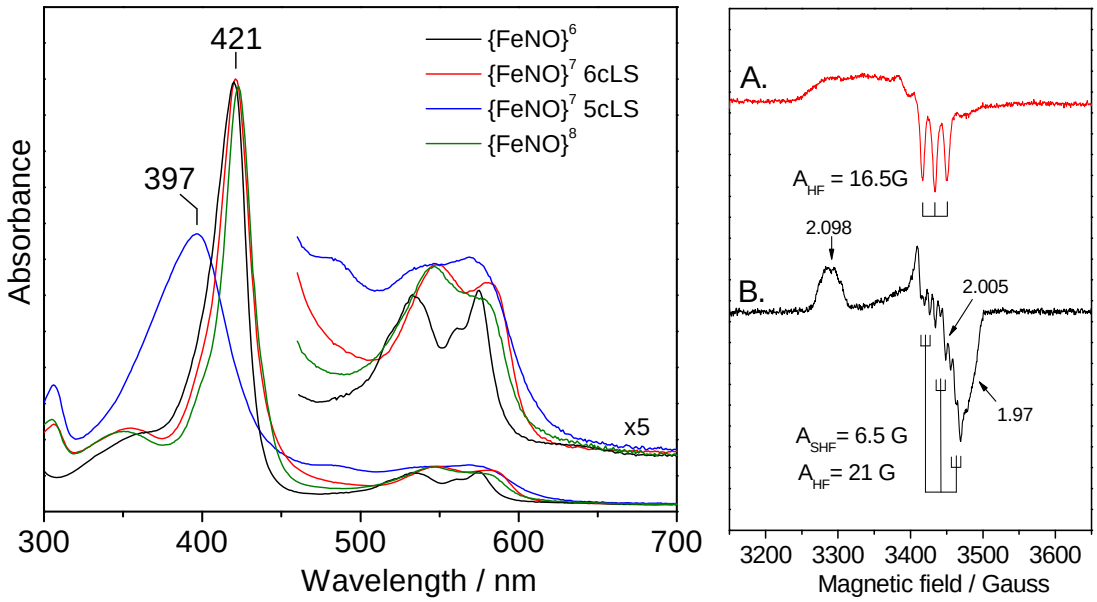

Figure 2.1 Electronic absorption spectra of myoglobin nitrosyl complexes at equivalent concentrations (left) and EPR spectra of 3-line (A) and 9-line (B) species observed in cytochrome ba_3(NO) (right).

Non-heme iron proteins

Electronic absorption spectra of non-heme iron and copper NO adducts are dominated by ligand to metal (LM) and metal to ligand (ML) charge transfer (CT) transitions. NO has been shown to react with ferrous state of many mononuclear non-heme iron enzymes to produce stable $S = 3/2$ high-spin non-heme $\{FeNO\}^7$ species, best described as a high-spin Fe^{II} ($S = 5/2$) antiferromagnetically coupled with NO^- ($S = 1$) (Arciero and Lipscomb, 1986; Nelson, 1987; Brown *et al.*, 1995). These species exhibit EPR signals at $g \sim 2$ and ~ 4. These $\{FeNO\}^7$ species exhibit characteristic electronic absorption at 400~500 nm due to nitrosyl to iron LMCT transitions. The molar extinction coefficient of these species is typically ~1000 $M^{-1}cm^{-1}$. Figure 2.2 shows electronic absorption and EPR spectra of the $\{FeNO\}^7$ species formed in Fe^{II}EDTA model complex.

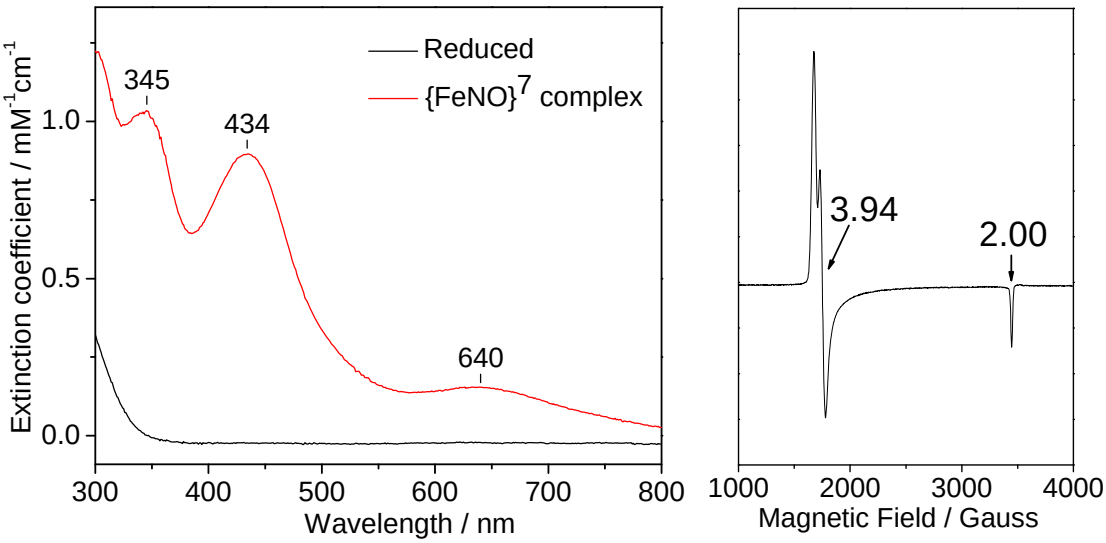

Figure 2.2 Electronic absorption spectra of Fe^{II}EDTA reduced and $\{FeNO\}^7$ complex (left) and EPR spectra of the $\{FeNO\}^7$ complex (right).

Both UV-vis absorption and EPR spectroscopies are based on absorption measurements and thus contain quantitative information on the absorbing species present in the sample. For UV-vis absorption spectroscopy, the absolute concentration of a species can be determined once a molar extinction coefficient (ε) is defined. For EPR spectroscopy, the concentration is determined in terms of spin-concentration using a series of well-characterized standards. For $S = 1/2$ and 3/2 $\{FeNO\}^7$ species, EPR signal quantifications are performed using a series of concentrations of Cu^{II}EDTA, an $S = 1/2$ system, and Fe^{II}EDTA(NO), a $S = 3/2$ complex. EPR measurements of these standards should be carried out under non-saturating condition and ideally using identical instrumental conditions. After double integration of the EPR derivative signals, the double integral values (A) are converted to normalized values (A_{norm}) according to equation 2.1 for more accurate quantification (Bou-Abdallah and Chasteen, 2008).

$$A_{norm} = \frac{A}{RG \times MA \times \sqrt{P} \times \frac{1}{T} \times g^{ave} \times CT} \qquad \text{(eq. 2.1)}$$

where RG is the receiver gain which is given by $10^{dB/20}$, MA is the modulation amplitude (in G), P is microwave power (in mW), T is temperature (in Kelvin), and CT is

conversion time (in ms). g^{ave} is average value of g-factors for all orientations and is given by equation 2.2.

$$g^{ave} = \frac{2}{3}\sqrt{\frac{g_x^2 + g_y^2 + g_z^2}{3}} + \frac{1}{3}\left[\frac{g_x + g_y + g_z}{3}\right] \qquad \text{(eq. 2.2)}$$

2.1.2 Low temperature FTIR photolysis

Although metal-nitrosyl complexes exhibit strong IR absorptions due to ν(N-O) stretching mode of M-N-O unit, IR spectra of protein aqueous solutions contain a number of bands due to H_2O bending (~1600 cm^{-1}), amide I (~1650 cm^{-1}), and amide II (~1550 cm^{-1}) of peptide vibrations, making it difficult to isolate the ν(N-O) mode. Alternatively, a photolysis-induced IR difference spectroscopy has been recognized as a powerful tool to selectively study metal-ligand interactions in metalloproteins. This method involves measurement of IR spectra before and after photolysis, and the difference of the two spectra contains only IR absorption features due to photodissociation of the ligand from the metal (e.g., ligand vibrations, and protein and cofactor bands associated with photodissociation events). At ambient temperature, the ligand IR absorption features rapidly disappear in difference spectra after photolysis due to ligand recombination. For example, recombination of NO and CO with myoglobin has been reported to be completed in picosecond to nanosecond time scales (Vos *et al.*, 2000). At cryogenic temperatures, however, the ligand recombination becomes sufficiently slow such that IR spectra of photodissociated species can be measured with a conventional FTIR instrument.

Figure 2.4 shows FTIR spectra of $Mb^{II}(CO)$ and $Mb^{II}(NO)$ before and after photolysis, and the 'dark' minus 'illuminated' difference spectra obtained at 30 K. In the difference spectrum of the $Mb^{II}(CO)$ complex, the photodissociation of CO from the heme and docking of the free CO to proteinaceous pocket are revealed by the positive ν(C-O)heme at 1945 cm^{-1} (i.e., from the heme-CO in the 'dark' spectrum) and the negative ν(C-O)free at 2131 cm^{-1} (i.e., from the free CO in the 'illuminated' spectrum) (Figure 2.4). The down-shifts of the ν(C-O) bands to 1901(-44) and 2083(-48) cm^{-1} with

^{13}CO are in perfect agreement with predicted value for isolated diatomic oscillators according to equation 2.3.

$$\upsilon = \upsilon' \sqrt{\left(\frac{M1+M2}{M1 \cdot M2}\right) / \left(\frac{M1'+M2'}{M1' \cdot M2'}\right)} \qquad \text{(eq. 2.3)}$$

where M_1 and M_2 are atomic masses. Besides the ν(C-O) bands, the difference spectra show a number of differential signals between 1100 and 1800 cm^{-1} which are not isotope sensitive and are not observed in control experiments with deoxy-Mb samples (Fe^{II}-heme without CO). Thus, these IR bands originate from perturbations of protein and heme vibrational modes associated with the CO dissociation event.

Similarly, the difference spectra of the Mb ^{II}(NO) reveal a positive ν(N-O)heme at 1613 cm^{-1} and a negative ν(N-O)free at 1855 cm^{-1}, which down-shift to 1539(-74) and 1772(-83) cm^{-1} with ^{15}N^{18}O isotopes, respectively. Again, these shifts are consistent with the calculated value for isolated diatomic vibrations. As shown in the difference spectra, use of isotope technique is particularly helpful for NO samples as ν(N-O)heme overlaps with the bands due to protein and heme vibrational modes.

Importantly, the 'dark' minus 'illuminated' difference spectra of Mb ^{II}(CO) and Mb ^{II}(NO) can be regenerated after annealing the FTIR samples above 40 K to allow geminate rebinding of the dissociated ligand to the heme iron (Figure 2.3). These photolytic processes are reversible and can be reproduced for multiple cycles.

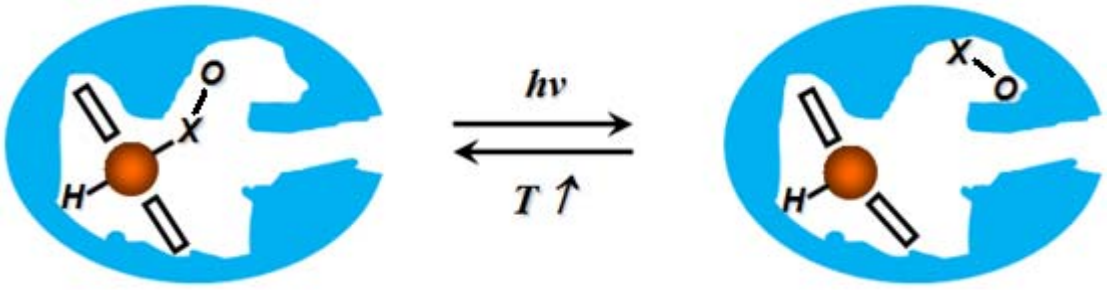

Figure 2.3 Schematic representation of diatomic ligand migration due to photolysis and geminate rebinding in myoglobin at cryogenic temperature. X is either C or N.

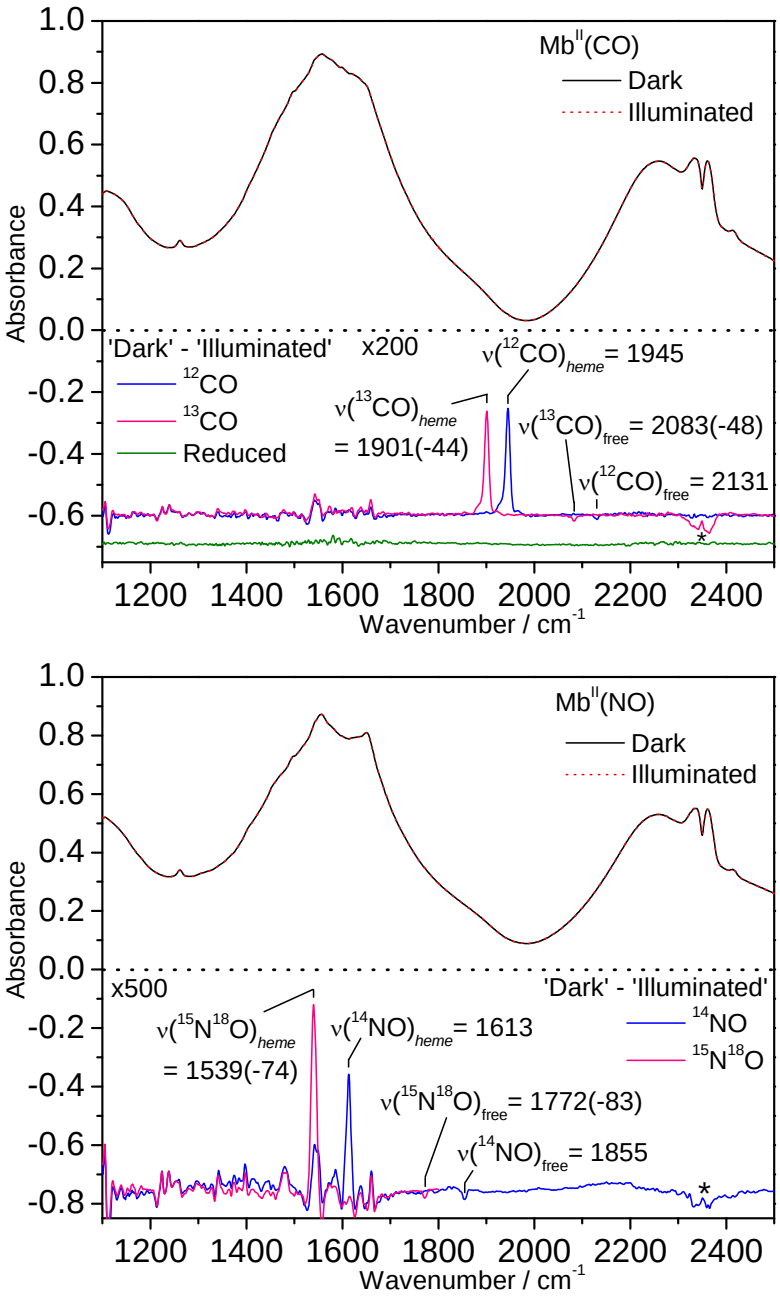

Figure 2.4 FTIR spectra of Mb ^{II}(CO) (top) and Mb ^{II}(NO) (bottom) before and after illumination and the 'dark' minus 'illuminated' difference spectra at 30 K. * indicates $\nu(CO_2)$ asymmetric stretching mode from variations in CO_2 content of sample compartment of FTIR instrument.

One could argue that processes observed at low temperature might not be relevant to functions of a protein in physiological conditions. However, evidence has accumulated over the years that cryogenic photolysis provide insights into physiological ligand binding mechanisms (Nienhaus *et al.*, 2002). Insight come from X-ray crystal structure analyses of photodissociated Mb ^{II}(CO) at cryogenic temperature, where photolysis at different temperature results in selective trapping of CO into different distal cavities also observable by occupancy with xenon in crystal exposed to high Xe pressure (Figure 2.3) (Chu *et al.*, 2000; Ostermann *et al.*, 2000). These studies indicate that, after entering the protein from the solvent matrix, the ligand samples multiple cavities, many times, before binding to the heme iron or exiting the protein matrix.

To validate the integrity of active site configurations and protein conformations during the course of cryogenic FTIR experiments, we also use other spectroscopic techniques such as resonance Raman, UV-vis absorption, and EPR spectrscopy. For hemoproteins, relatively high-quality UV-vis spectra can be obtained on FTIR films at cryogenic temperature. Figure 2.5 shows comparison of UV-vis spectra of Mb ^{II}(CO) obtained at room temperature and 30 K which correspond to the FTIR spectra shown above (Figure 2.4 top). In dark state, the low temperature UV-vis spectra reveal the Soret band at 426 nm and α/β bands at 546 and 582 nm, which are in good agreement with those observed at room temperature. Upon illumination, Soret absorption at 444 nm appears at the expense of the Soret bands at 426 nm, indicating the dissociation of CO from the heme (Figure 2.5), as reported by the FTIR photolysis data.

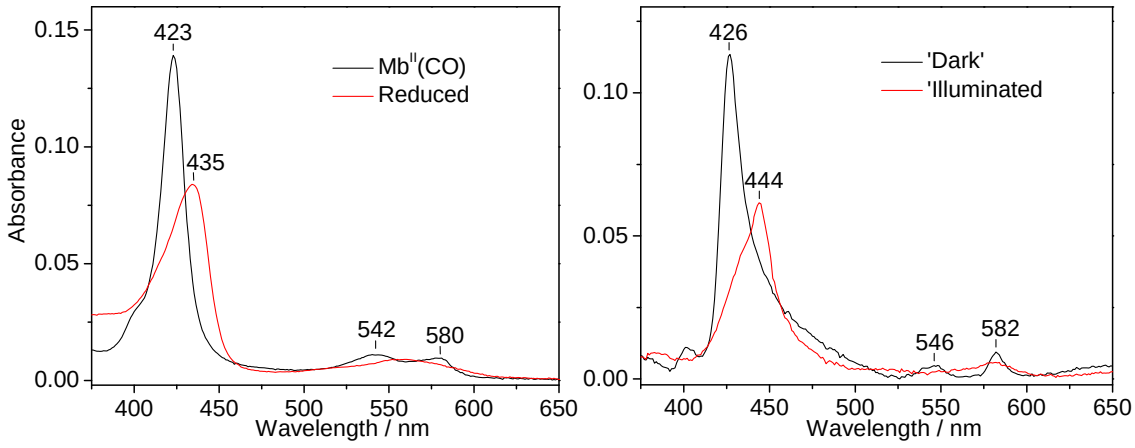

Figure 2.5 UV-vis spectra of Mb ^{II} reduced and CO adduct at room temperature (left) and of Mb ^{II}(CO) before and after illumination at 30 K.

Carrying mechanistic studies at cryogenic temperatures provide further advantages. The temperature dependence of ligand-rebinding kinetics directly reflects the thermal stability of dissociated states. In chapter 3 and 4, illumination of cytochrome *ba*$_3$(NO) and *bo*$_3$(NO) dissociates heme-nitrosyl complexes with equivalent efficiency, but rebinding of NO in *ba*$_3$ requires temperature annealing up to 90 K, which is 30-K higher than in *bo*$_3$(NO) (Hayashi *et al.*, 2007; Hayashi *et al.*, 2009). This difference in rebinding temperature indicates that the photolyzed *ba*$_3$(NO) is thermodynamically more stable than the photolyzed state in *bo*$_3$(NO). In fact, our vibrational data show that the dissociated NO is stabilized through binding to Cu_B^I in *ba*$_3$, but not in *bo*$_3$ (Hayashi *et al.*, 2007; Hayashi *et al.*, 2009). In chapter 4, different ligand-rebinding temperatures for CO and NO complexes in *bo*$_3$ and *ba*$_3$ allow us to isolate spectroscopic signatures from these two complexes (Hayashi *et al.*, 2009).

2.1.3 RR spectroscopy

Unlike infrared absorption spectroscopy, Raman spectroscopy is a scattering technique where the interaction of monochromatic light with a molecule reports on molecular vibrations. The energy difference between scattered and incident photons corresponds to vibrational transition energy of the molecule. In resonance Raman (RR) spectroscopy, the energy of the incident light is adjusted to match the energy of an electronic transition to enhance vibrational modes involving electrons associated with the excited state. This resonance effect becomes particularly useful to gather information from prosthetic groups that exhibit electronic absorptions in large biomolecules, such as proteins and enzymes (Carey, 1982).

Hemoproteins have been extensively studied using RR spectroscopy. Use of Soret excitation results in strong resonance enhancement of porphyrin skeletal vibrations that are sensitive to oxidation state, spin states, and coordination number of the heme iron, and heme pocket environment. RR spectroscopy has also been used for the study of other metalloproteins. For example, in non-heme iron proteins, the nitrosyl to metal LMCT transitions can be used to selectively resonance enhance the vibrational modes associated with iron-nitrosyl complexes (i.e., Fe-N-O stretching modes). Figure 2.5 shows the UV-

vis absorption spectra of reduced and the $\{FeNO\}^7$ nitrosyl complex of iron superoxide dismutase (FeSOD). The $\{FeNO\}^7$ species exhibits a visible absorption band at ~420 nm due to nitrosyl to iron LMCT transitions (Jackson *et al.*, 2003), and a 458-nm excitation allows resonance enhancement of vibrational modes associated with the $\{FeNO\}^7$ unit. Isotope-edited RR spectra of Fe(II)SOD(NO) reveal ν(Fe-NO), ν(N-O), and a combination mode (ν(Fe-NO) + δ(Fe-NO)) at 482, 1771, and 957cm^{-1}, respectively. Other non-isotope sensitive bands present in the RR spectra are due to peptide backbone and aromatic side chains (Carey, 1982), and are effectively subtracted out in difference spectra (Figure 2.6).

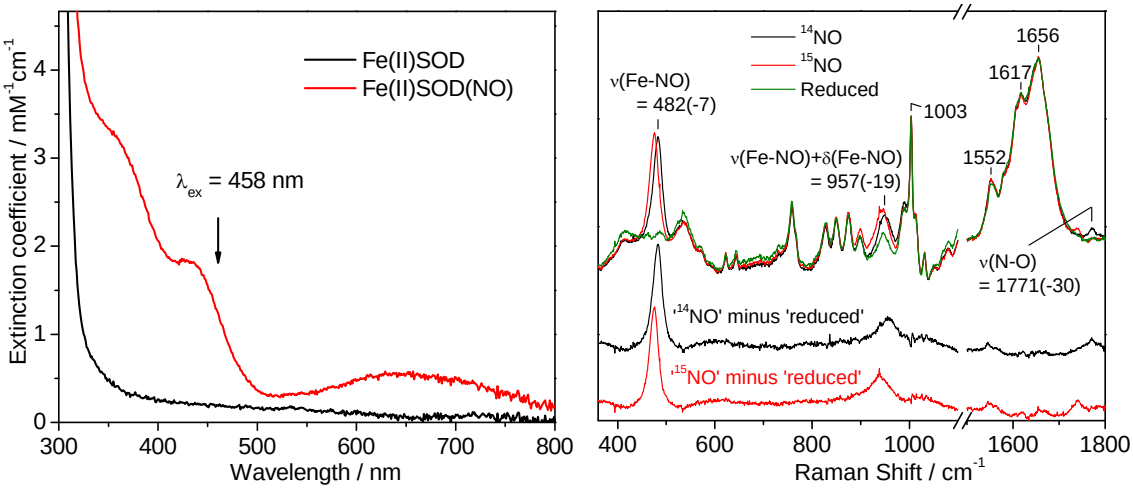

Figure 2.6 UV-vis spectra of Fe(II)SOD and Fe(II)SOD(NO) at room temperature (left) and RR spectra of reduced, NO and ^{15}NO adduct Fe(II)SOD , obtained with 458-nm excitation at room temperature (right).

2.2 Instrumentation and general methods

2.2.1 Anaerobic sample preparation

Samples are purged with argon bubbled through water to prevent desiccation and transferred to a glove box containing less than 1 ppm of O_2 (Omni-Lab System; Vacuum Atmospheres Co.). The reduction of protein solution is achieved by addition of microliter aliquots of concentrated sodium dithionite solution (~100 mM), followed by removal of the excess reduction agent with desalting spin column (Zebra, Pierce). To prepare NO adducts, the headspaces over reduced protein solutions are replaced with NO (NO

purchased from Airgas and ^{15}NO and $^{15}N^{18}O$ from Aldrich and treated with 1 M KOH solution) directly in UV-vis cuvettes, EPR tubes, or Raman capillaries (Figure 2.7). For FTIR measurements, the NO adducts are prepared in Eppendorf tubes before immediate transfer to CaF_2 cells. ^{12}CO (Airgas) and ^{13}CO (99% ^{13}C; ICON stable isotopes) adducts are obtained by the same procedure.

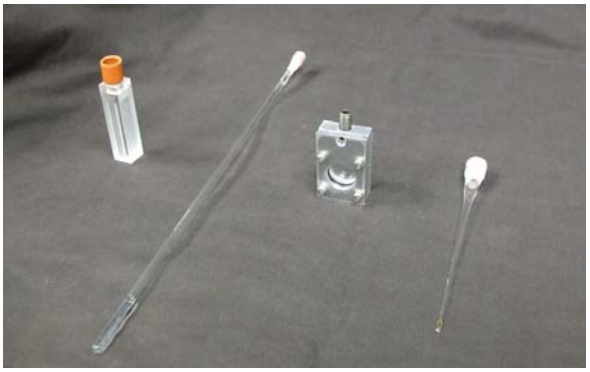

Figure 2.7 From left to right; anaerobic UV-vis cuvette, EPR tube, FTIR cell, and Raman capillary

Stoichiometric addition of NO to fully reduced protein is achieved by adding small aliquots of NO-saturated solutions after determining the stock concentration by titration against deoxymyoglobin. Alternatively, a diethylamine NONOate (Cayman Chemical, Ann Arbor, MI) is added into reduced protein solutions. The concentration of NONOate stock solution was determined using an ε_{250} extinction coefficient of 6500 $M^{-1}cm^{-1}$ in 0.01 M NaOHaq, and addition of aliquots to deoxymyoglobin at pH~5 was used to further confirm the concentration of NO produced. In both cases, these additions were made just prior to transfer into EPR tubes, Raman capillaries or FTIR cells.

2.2.2 UV-vis spectroscopy

Electronic absorption spectra are obtained using a Cary 50 Varian spectrophotometer using 1-nm resolution a scanning rate of 1200 nm/min. Protein solutions are monitored in UV-vis cuvettes, EPR tubes, Raman capillaries or FTIR cells, whose pathlength is 1 cm, ~3 mm, 1.2 mm, and 15 μm, respectively (Figure 2.7).

2.2.3 Low temperature FTIR and UV-vis spectroscopy

Approximately 15 µL of protein solutions are deposited as a droplet on a CaF_2 window (International Crystal Labs, Garfield, NJ) and a second CaF_2 window is gently dropped on the sample to form an optical cell with a pathlength controlled by a 15-µm Teflon spacer (International Crystal Labs, Garfield, NJ) (Figure 2.8). After confirming the presence of the NO adduct by UV-vis absorption spectroscopy, the FTIR cell is mounted to a sample rod which then flash-frozen in liquid N_2, prior to insertion into the sample compartment of closed-cycle cryogenic systems (Displex and Omniplex, Advanced Research System) (Figure 2.8). The sample is placed inside the sample compartment of the FTIR or the UV-vis instrument and kept in the dark during cooling below 30 K (Figure 2.9). The temperature of the sample is monitored and controlled with a Cryo-Con 32 and Lake Shore Model 331 units.

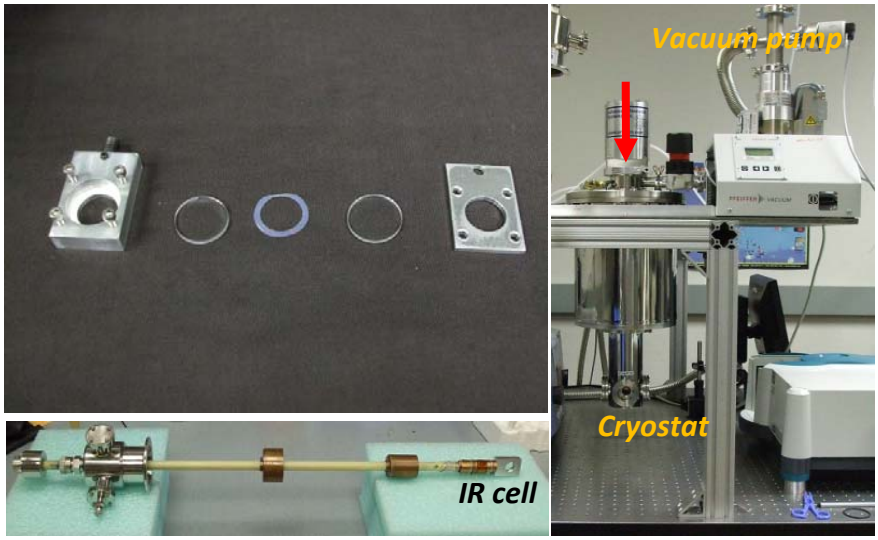

Figure 2.8 IR cell compositions (left top): a cell holder, bottom window, Teflon spacer, top window, and cover. A sample rod (left bottom) and Closed-cycle cryogenic system Omniplex (right). The red arrow indicates where the sample rod is inserted.

FTIR spectra are obtained on a Perkin-Elmer System 2000 and a Bruker Tensor 27, both equipped with a liquid-N_2-cooled MCT detector. Sets of 1000-scan accumulations are acquired at 4-cm^{-1} resolution. Photolysis of nitrosyl or carbonyl complexes are performed by continuous illumination of the sample directly in the FTIR

sample chamber using a 50-W tungsten lamp and 300-W arc lamp after filtering out heat and NIR emissions. The complete reversibility of the photolysis processes is confirmed by reproducing the same FTIR difference spectra after annealing the samples. The low temperature UV-vis spectra are obtained directly on FTIR cells mounted on a closed-cycle cryogenic system (Displex and Omniplex, Advanced Research system), using a Cary 50 Varian spectrophotometer.

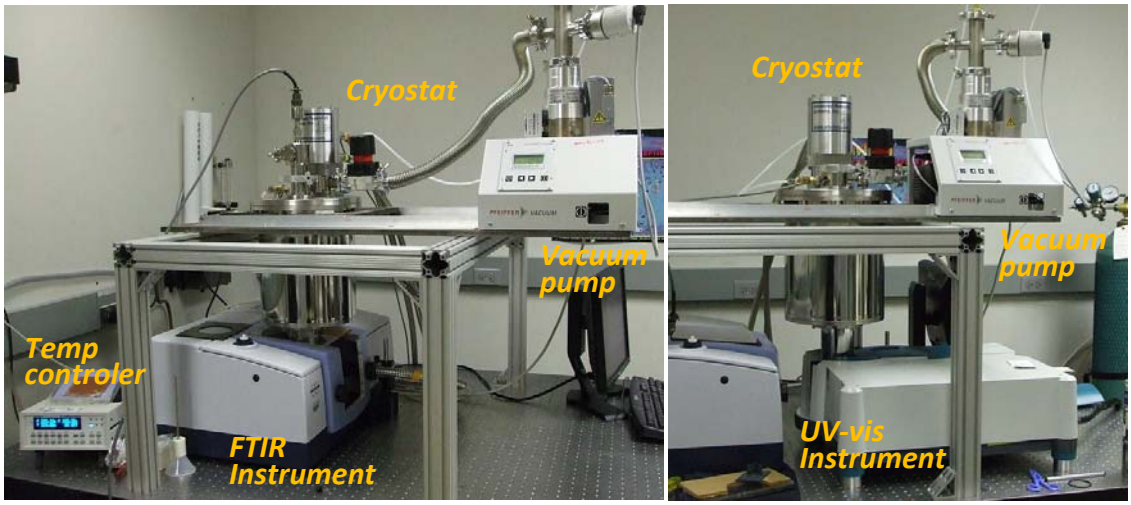

Figure 2.9 Instrumental setup for the low temperature IR (left) and UV-vis spectroscopy (right).

2.2.4 RR spectroscopy

Resonance Raman (RR) spectra are obtained using a custom McPherson 2061/207 spectrograph (set at 0.67 m with variable gratings) equipped with a liquid-N_2-cooled CCD detector (LN-1100PB, Princeton Instruments). The 413-, 568-, and 647-nm excitation lasers are derived from an Kr laser (Innova 302, Coherent), the 442-nm line from a He-Cd laser (4240NB Liconix), and the 458-, 488-, and 514-nm excitation lasers from an Ar laser (Innova 90, Coherent). Kaiser Optical supernotch filters or long-pass filters (RazorEdge, Semrock) are used to attenuate Rayleigh scattering (Figure 2.10).

Room temperature RR spectra are collected in a 90^o scattering geometry on samples mounted on a reciprocating translation stage (Figure 2.10). To assess the photosensitivity of the NO adduct, rapid acquisitions with minimal laser power and continuous sample translation are compared with longer data acquisitions on static

samples. The low temperature RR spectra are collected in a backscattering geometry on samples prepared in a multiwell sample holder attached to the same closed-cycle cryostat system used in the low temperature FTIR and UV-vis experiments (Figure 2.10). Frequencies are calibrated relative to indene and aspirin standards and are accurate to ±1 cm^{-1}. Polarization conditions are optimized using CCl_4 and indene. The integrity of the RR samples is confirmed by direct monitoring of their UV-vis absorption spectra in Raman capillaries before and after laser exposure. Typical enzyme concentrations for RR experiments are ~100 μM for heme-proteins and ~1 mM for non-heme iron proteins.

Figure 2.10 Raman setup (Top) and different types of sample-geometry: a 90° scattering geometry for room temperature experiments (bottom left) and backscattering geometry for low temperature experiments (bottom right). The laser beam paths are indicated by green lines.

2.2.5 EPR spectroscopy

Electron paramagnetic resonance (EPR) spectra are obtained with a Bruker E500 X-band EPR spectrometer equipped with a superX microwave bridge and a dual-mode cavity with a helium flow cryostat (ESR900, Oxford Instrument, Inc.). The experimental conditions, i.e., temperature, microwave power, and modulation amplitude, are varied to optimize the detection of all potential EPR active species. Quantitation of the EPR signals is performed under non-saturating conditions by double integration and comparison with series of concentrations of Cu^{II}EDTA and Fe^{II}EDTA(NO) standards. Photolysis of samples is achieved by direct illumination of samples in EPR cavity using the 300-W arc lamp.

CHAPTER 3

CHARACTERIZATION OF Cu-(NO) COMPLEX IN CYTPCHROME *ba*$_3$

3.1 Cytochrome *ba*$_3$ from *Thermus thermophilus*

Cytochrome *ba*$_3$ is a cytochrome *c* oxidase that is expressed under limited O_2 supply in the extremely thermophilic bacterium *Thermus thermophilus* (Keightley *et al.*, 1995). On the basis of sequence similarity and conserved amino acid residues for the proton channels, HCOs are divided into three subgroups: A, B, and C (Pereira *et al.*, 2008). Most of HCOs, including mitochondrial cytochrome *c* oxidase and bacterial *aa*$_3$- and *bo*$_3$-type oxidases, are classified as A-type and possess at least two proton channels. Cytochrome *ba*$_3$ and *cbb*$_3$ are diverged from other members of the HCO superfamily and classified as B and C type, respectively; they exhibit only very few sequence identities with other members of this superfamily (~20% sequence identity) and possess fewer recognized proton channels. Despite this divergence among HCOs, X-ray crystal structures show that these enzymes share the same structural fold of the catalytic subunit (subunit I) and the side chain residues that anchor the low-spin heme and the catalytic high-spin heme/copper center. From these structural considerations, the chemistry that takes place at the active site of HCOs seems likely to be the same.

---

*Material in this chapter has been published in this or similar form in *Journal of American Chemical Society*, and is used here with permission of the American Chemical Society.

Hayashi T, Lin I.J., Chen Y., Fee J.A., and Moënne-Loccoz P. (2007) Fourier Transform Infrared Characterization of a Cu_B-Nitrosyl Complex in Cytochrome *ba*$_3$ from *Thermus thermophilus*: Relevance to NO Reductase Activity in Heme-Copper Terminal Oxidases. ***J. Am. Chem. Soc.***, 129, 14952-14958.

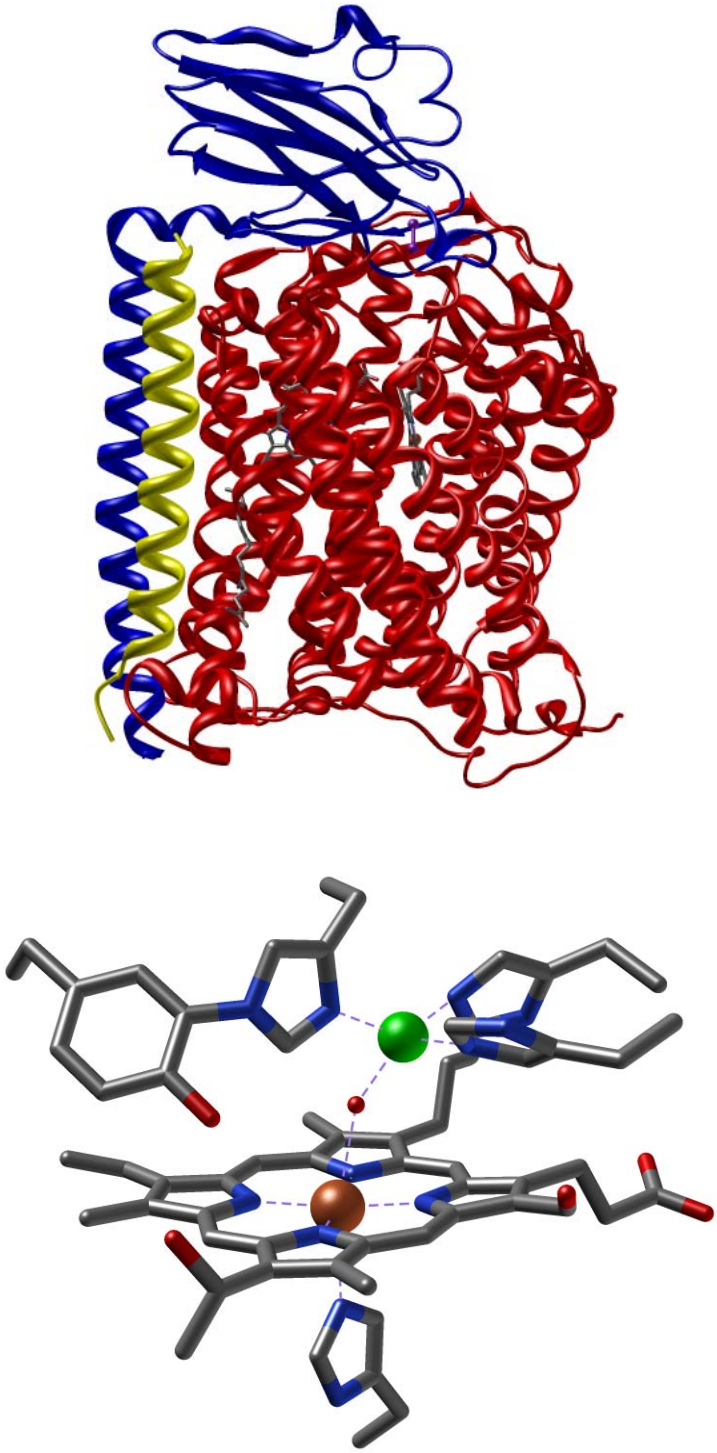

Figure 3.1 Overall structure (top) and zoom-in on the heme/copper center (bottom) of Cytochrome ba_3 from *Thermus thermophilus* (PDB code: 1XME). Peripheral chain is omitted in order to better visualize the heme/copper center

Unlike *aa₃*-type oxidases, *ba₃* has been shown to catalyze two electron reduction of NO to N_2O (Giuffre *et al.*, 1999). Because the NO-reductase activity of *ba₃* is less than 1% that of denitrifying NO reductases, it is unlikely to be its primary function (Butler *et al.*, 2002). However, *ba₃* can be viewed as a 'slow' homologue of NORs and may reveal features responsible for NO reductase catalytic ability. Furthermore, characterization of the reaction intermediates, if any, can expand our knowledge of the chemical behavior of the divergent a_3-Cu_B centers and dinuclear sites in general.

3.2 Proposed NO reduction mechanisms for *ba₃*

As mentioned in Chapter 1.4, the catalytic mechanism of NO reduction in terminal oxidases is generally considered to be initiated by the binding of NO to heme a_3 in the fully-reduced enzyme. Subsequent steps are expected to involve Cu_B^I, either as a coordination site for a second NO molecule or as an electron donor and electrostatic partner to a heme a_3-hyponitrite complex (Pinakoulaki *et al.*, 2005; Blomberg *et al.*, 2006; Ohta *et al.*, 2006). The initial heme a_3-nitrosyl complex is a low-spin Fe(II)-NO, i.e., an $S = 1/2$ $\{FeNO\}^7$ species in Enemark and Feltham notation (Enemark and Feltham, 1974). Using resonance Raman (RR) spectroscopy, Varotsis and coworkers have shown that the *ba₃*(NO) complex is a six-coordinate species with ν(Fe-NO) and ν(N-O) at 539 and 1620 cm^{-1}, respectively (Pinakoulaki *et al.*, 2005). In addition, Vos and coworkers have monitored the rebinding kinetics of the photolyzed NO, at room temperature in the picosecond to microsecond time scale. While geminate NO recombination to the heme of myoglobin is completed in the picosecond timescale, rebinding of NO to heme a_3 is observed on the nanosecond timescale in *ba₃*(NO) (Pilet *et al.*, 2004). Since binding of NO from solution occurs in microseconds, these results strongly support the idea that the photolyzed NO binds transiently to Cu_B before rebinding to heme a_3 in the nanosecond regime. Varotsis and coworkers have attempted to gain information on this photoinduced state at room temperature using time-resolved step-scan FTIR, but the microsecond-time resolution of this technique precludes the characterization of a Cu_B-nitrosyl complex (Pinakoulaki *et al.*, 2005).

In this chapter, we carry out low-temperature FTIR photolysis experiments to study the *ba₃*(NO) complex. Our hypothesis is that, at low temperature, NO dissociates

from the heme-a_3 and binds to a secondary site upon photolysis at low temperature, and this site would likely be the second NO binding site during the NO reduction turnover in ba_3. The low-temperature UV-vis, EPR, and RR spectroscopies confirm the efficiency of the photolysis and NO-isotopic labeling permits the isolation of ν(NO) modes from the light-induced FTIR difference spectra. After NO dissociation from the heme a_3, we detected a new species associated with an IR band at 1589 cm^{-1} at 30 K, which is assigned to a Cu_B-nitrosyl complex. However, this N-O stretching frequency is unusually low compared to the few Cu-NO species reported so far (Ruggiero *et al.*, 1993; Zhao *et al.*, 1994). Because our low-temperature UV-vis and RR data rule out a bridging configuration between Cu_B and heme a_3, this exceptionally low ν(NO) identifies the Cu_B-nitrosyl complex as either an O-bound (η^1-O) or a side-on (η^2-NO) complex. The relevance of this Cu_B-nitrosyl complex is discussed in the context of the NO reductase activity in the heme/copper center of cytochrome ba_3.

3.3 Materials and methods

Protein preparations

The expression and purification of ba_3 was performed as previously described (Chen *et al.*, 2005). Protein solutions were prepared in 20 mM Tris-HCl pH 7.5 with 0.05 % dodecyl β-D-matoside and concentrated in a glovebox containing less than 1-ppm O_2 using a microcon filtering device (30 kD cutoff, Biomax, Millipore), if necessary. The sample was fully reduced by addition of dithionite at a final concentration of 10 mM in an Eppendorf tube with a septum top. NO gases (NO and $^{15}N^{18}O$ purchased from Aldrich, ^{15}NO purchased from ICON) were initially treated with 1 M KOH solution to remove higher nitrogen oxide impurities. NO gas addition to the sample headspace was achieved in the glove box using gastight Hamilton syringes to reach a partial pressure of 0.1 atm of NO. After one minute of incubation at room temperature, the septum was removed and protein solution was transferred to an IR cell, RR capillary, EPR tube, or UV-vis cuvette. Experiments with 1.0 equivalent NO addition were performed as described in Chapter 2.2.

Molecular spectroscopy

UV-vis, EPR, FTIR and RR spectroscopy were carried out as described in Chapter 2.2. The typical enzyme concentrations for UV-vis, EPR, FTIR and RR spectroscopy are 3, 30, 350, and 430 μM, respectively.

For EPR spectroscopy, 250 μL of *ba*$_3$(NO) complex prepared in an EPR tube was flash-frozen in liquid N_2 after confirming the presence of the NO adduct by UV-vis absorption spectroscopy. Quantitation of the EPR signals was performed under non-saturating conditions by double integration and comparison with 0.1 mM and 0.01 mM Cu^{II}EDTA standards.

The FTIR cell was mounted to a closed-cycle cryogenic system and kept in the dark while the temperature dropped to 30 K (cooling rate ~ 4 K/min). The FTIR spectra were obtained on a Perkin-Elmer system 2000 equipped with a liquid-N_2 cooled MCT detector and purged with compressed air dried and depleted of CO_2. Sets of 1000-scan accumulations were acquired at a 4-cm^{-1} resolution. These data averaging conditions required 15-min, and because of instrumental drift, further accumulation time did not result in an improvement of the FTIR difference spectra. Photolysis of the *ba*$_3$(NO) complex was achieved with continuous illumination of the samples directly in the FTIR sample chamber with a 50 W tungsten lamp after filtering out heat and NIR emission. The same illumination procedure was used to follow the dissociation-rebinding process by UV-vis spectroscopy with the Cary-50 spectrophotometer.

RR sample of reduced *ba*$_3$ and *ba*$_3$(NO) complexes were prepared in a glovebox and loaded on a multi-well sample holder mounted to the same closed cycle cryostat system used in the FTIR experiments. The RR spectra were obtained using a backscattering geometry. Kaiser Optical supernotch filters were used to attenuate Rayleigh scattering generated by the 413- and 442-nm excitation. Frequencies were calibrated relative to aspirin, indene and CCl_4 standards and are accurate to ±1 cm^{-1}.

3.4 Formation of *a*$_3$-NO complex in *Tt ba*$_3$

In our preliminary experiments, extended exposure of fully-reduced *Tt ba*$_3$ to excess NO_g was shown to produce UV-vis spectra identical to that of fully-oxidized *Tt ba*$_3$, consistent with the NO reductase activity reported previously. However, rapid

exposure of the fully-reduced *Tt* ba_3 to a headspace containing 0.1 atm NO_g results in the formation of a ba_3(NO) complex as evidenced by changes in its UV-vis spectrum (Figure 3.2A). Specifically, the Fe^{II} heme a_3 Soret band at 443 nm blue-shifts to merge with the Soret absorption of the Fe^{II} low-spin heme *b* at 426 nm. Moreover, the Fe^{II} heme a_3 absorption at 612 nm blue-shifts to 600 nm upon NO binding. Identical UV-vis absorption features were observed at 30 K (Figure 3.2B). The absence of a 443-nm shoulder in the Soret region and the presence of a 597-nm band confirm the presence of the heme a_3-NO complex at 30 K (Figure 3.2B) (Reddy *et al.*, 1996). After a few minutes of illumination with white light, the 443-nm shoulder characteristic of the high-spin Fe(II) heme a_3 species is clearly observed at the expense of the 597-nm absorption band from the a_3-NO complex (Figure 3.2B red trace).

The low-temperature UV-vis data reveal efficient NO photolysis from heme a_3 to form a stable photolyzed state at 30 K. Based on the intensity of the 443-nm shoulder in the UV-vis spectrum of 'illuminated' ba_3(NO) and that of 'illuminated' ba_3(CO), we estimate that in the former samples, at least 2/3 of the total heme a_3 content is converted to high-spin after illumination.

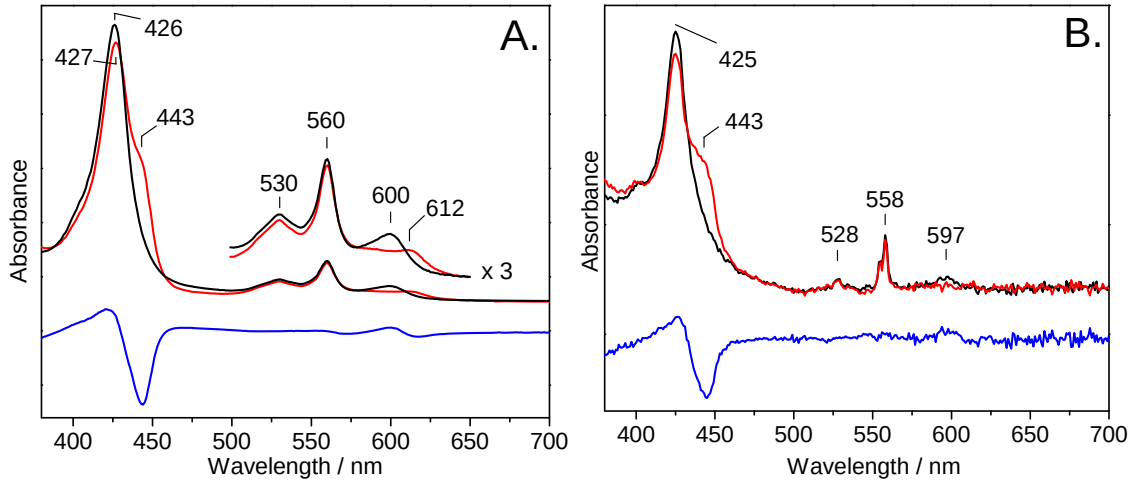

Figure 3.2 UV-vis absorption spectra of fully reduced cytochrome ba_3 (red) and the ba_3(NO) complex (black), and 'the ba_3(NO)' minus 'fully reduced ba_3' difference spectrum (blue) obtained at room temperature (A); and of the ba_3(NO) complex before (black) and after illumination (red), and 'dark minus illuminated' difference spectrum (blue) obtained at 30 K (B).

Prior to photolysis, the EPR spectrum of ba_3(NO) complex shows a superposition of two signals centered near $g \sim 2$ (Figure 3.3A black trace). One signal is readily photolabile and exhibits g values (2.098, 2.008, 1.97) and a 9-line ^{14}N-hyperfine structure at g_z (A_{NO} = 21.5 G, A_{His} = 6.5 G), characteristic of 6-coordinate heme-nitrosyl with a proximal histidine ligand (Yonetani *et al.*, 1972). Another signal with distinctive 3-line ^{14}N-hyperfine structure (A_{NO} = 16.5 G) (Figure 3.3A red trace) is reminiscent of the 5-coordinate heme-nitrosyl myoglobin-NO formed at low-pH and in hemoglobin-NO in the presence of allosteric effectors, and in myoglobin proximal histidine variants (Rein *et al.*, 1972; Wayland and Olson, 1974; Szabo and Perutz, 1976; Hille *et al.*, 1979; Ruggiero *et al.*, 1993). The two different EPR signal are easily isolated from one another as the 3-line EPR signal is not affected by illumination at 30 K.

Equivalent 3-line EPR signal have been observed in bovine and *P. denitrificans* aa_3(NO) and have been assigned alternatively to a 5-coordinate a_3-NO subpopulation or to a 6-coordinate a_3-NO with distinct orientations of the imidazole and nitrosyl axial ligands, which limits the interaction between the p-orbital of the imidazole nitrogen and the π-orbital of NO moiety (Pilet *et al.*, 2007) (vide infra). Significant variations in the relative intensity of the 9-lines versus 3-lines EPR signals were observed among samples, with the 3-line EPR species representing as low as 20% in some enzyme preparation but reaching up to 50% in others (Figure 3.3B). On the other hand, using different reducing conditions (10 mM dithionite, and 10 mM ascorbate with 0.1 mM *N,N,N',N'*-tetramethyl-*p*-phenylenediamine (TMPD)), or different NO concentrations (1 or 5 equiv) had no impact on the relative concentrations of the two heme a_3-NO populations (data not shown). Increasing the protein concentration to 300 μM as used in the FTIR experiments had also no effect on the intensity ratio between the two EPR signals (data not shown). While the two heme a_3-NO species are easily distinguished by EPR spectroscopy, the low temperature UV-vis spectra show no evidence for the variable population of the 3-line EPR signal. Similarly, RR experiments fail to detect two distinct heme-nitrosyl complexes (vide infra).

Both EPR and UV-vis experiments show that rebinding of the photolyzed NO to the heme a_3 is inhibited at temperatures below 80 K. This temperature is lower than the protein-solvent glass transition temperature (~180 K) at which the escape of photolyzed

ligand can occur. Thus, the data suggest that rebinding of NO to the heme a_3 does not require release of the photolyzed ligand from the active site pocket as proposed for the gate rebinding mechanism of CO in HCOs. Yet, the rebinding temperature in ba_3(NO) is significantly higher than that measured with the ferrous-nitrosyl complex of myoglobin where rebinding of the photodissociated NO occurs at 40 K (Miller *et al.*, 1997; Schlichting and Chu, 2000) which suggests that the photolyzed NO is trapped by stabilizing interactions, presumably with Cu_B^+. Earlier low-temperature UV-vis and EPR photolysis experiments carried out with bovine HCO have reported similar rebinding temperatures (Yoshida *et al.*, 1980; Boelens *et al.*, 1982). As with these early studies, formation of the photolyzed state of ba_3(NO) does not result in the appearance of new features in the EPR or UV-vis spectra.

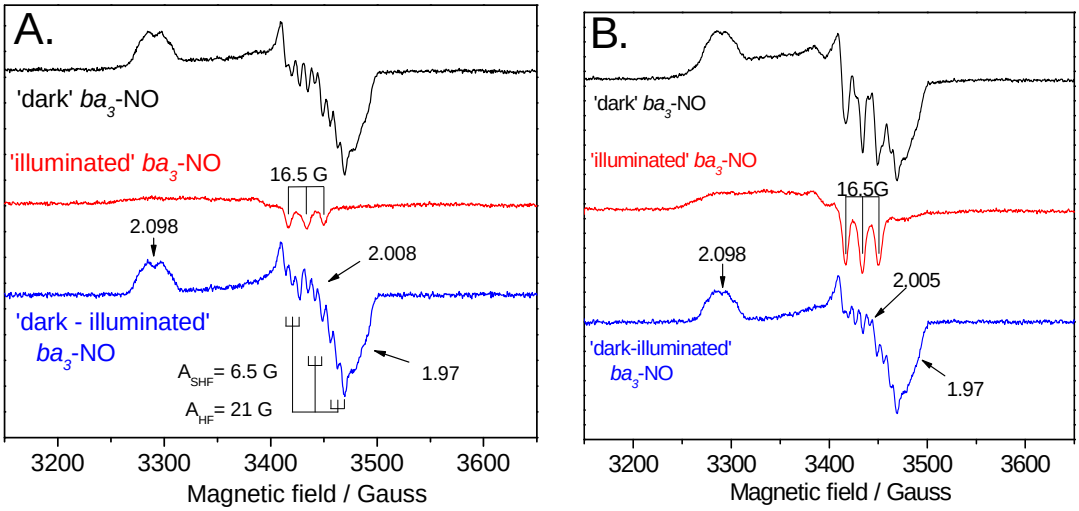

Figure 3.3 EPR spectra of the ba_3(NO) complex prepared with two independent enzyme preparations (A and B) at 30 K. Before and (black) and after (red) illumination, and the 'dark' minus 'illuminated' difference spectrum (blue).

3.5 Trapping of the photolyzed NO on Cu_B^I at 30 K

Figure 3.4A shows 'dark' minus 'illuminated' FTIR difference spectra of fully-reduced ba_3(NO) at 30 K; an FTIR difference spectrum collected on the ba_3(CO) complex is also shown for comparison. In the latter complex, the difference spectrum reveals a positive and negative bands at 1985 and 2052 cm^{-1}, which are assigned to ν(C-

O) of a_3-CO and Cu_B-CO complexes, respectively. These observations are consistent with dissociation of CO from heme a_3 and ligation of the CO to Cu_B. The difference spectrum also shows weaker differential signals near and below 1700-cm^{-1} that are insensitive to CO-isotopic labeling and are assigned to perturbations of amide and porphyrin vibrational modes from heme a_3 (Gregoriou *et al.*, 1995).

In the 'dark' minus 'illuminated' FTIR difference spectra of ba_3(NO) obtained at 30 K, the positive 1622 cm^{-1} and negative 1589 cm^{-1} features are assigned to ν(N-O) modes based on their -29 and -27 cm^{-1} downshifts with ^{15}NO (Figure 3.4A). By analogy with ba_3(CO) complex, a few minutes of white light at 30 K is sufficient to generate these FTIR difference spectra and subsequent illuminations do not produce any further changes. The positive band at 1622 cm^{-1} is attributed to the heme a_3-NO complex based on its photolabile character and this ν(N-O)a_3 frequency is within a few cm^{-1} of that reported by Varotsis and coworkers (Pinakoulaki *et al.*, 2005). The photo-induced ν(N-O) appears as a negative band at 1589 cm^{-1} and is best extracted from raw data by making differences of difference spectra such that modes insensitive to NO-isotopic labeling cancel out (Figure 3.4B). This approach is particularly useful with the $^{15}N^{18}O$ sample where the superposition of differential signals around 1530 cm^{-1} leads to the lack of a negative ν(^{15}N-^{18}O) (Figure 3.4B lower red trace). The subtraction of the $^{15}N^{18}O$ data from those obtained with $^{14}N^{16}O$ clearly reveals two sets of isotope-sensitive bands. The ['dark' minus 'illuminated' ba_3($^{14}N^{16}O$)] minus ['dark' minus 'illuminated' ba_3($^{15}N^{18}O$)] (Figure 3.4B, lower green trace) exhibits a positive and negative bands at 1622 and 1547 cm^{-1} which correspond to the ν(^{14}N-^{16}O)a_3 and ν(^{15}N-^{18}O)a_3, respectively. In this same trace, the photo-induced ν(^{14}N-^{16}O) is observed as a negative band at 1589 cm^{-1} and a positive ν(^{15}N-^{18}O) at 1535 cm^{-1}.

The observed frequency and isotopic dependence of the 1589 cm^{-1} signal is consistent with an N-O stretching mode of a metal-nitrosyl, and by analogy with the photolysis on the CO complex, we assign this photo-induced signal to an ν(N-O) of a Cu_B-nitrosyl complex. In agreement with the UV-vis and EPR data, the 'dark' FTIR spectrum can be regenerated after annealing the FTIR sample at 90 K, and a new set of 'dark' and 'illuminated' spectra can be collected subsequently. Comparison of successive FTIR difference spectra obtained after annealing above 90 K shows identical features as

the previous cycle, confirming the reversibility of the photolysis to produce identical FTIR difference spectra from one cycle to the next (Figure 3.5). These observations demonstrate that the low-intensity white light used in these experiments only induces fully-reversible processes involving only the photolysis of the exogenous ligand bound to heme a_3.

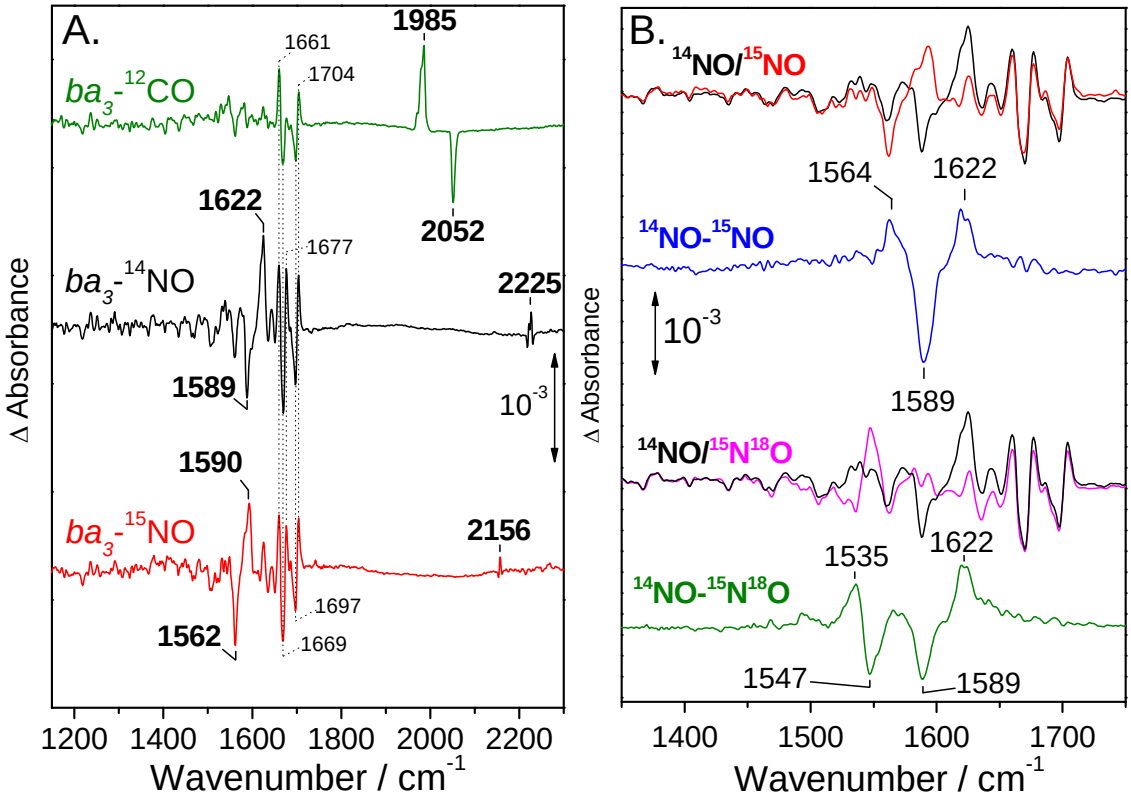

Figure 3.4 FTIR 'dark' minus 'illuminated' difference spectra of the ba_3(CO) (green) and ba_3(NO) (NO; black, ^{15}NO; red) complex at 30 K (A). Difference of 'dark' minus 'illuminated' FTIR difference spectra obtained at 30 K (B). Top traces: ba_3(NO) (black), ba_3(^{15}NO) (red), and the ba_3(NO) minus ba_3(^{15}NO) difference spectra (blue). Bottom traces: ba_3(NO) (black), ba_3(^{15}N^{18}O) (red), and the ba_3(NO) minus ba_3(^{15}N^{18}O) difference spectra (green).

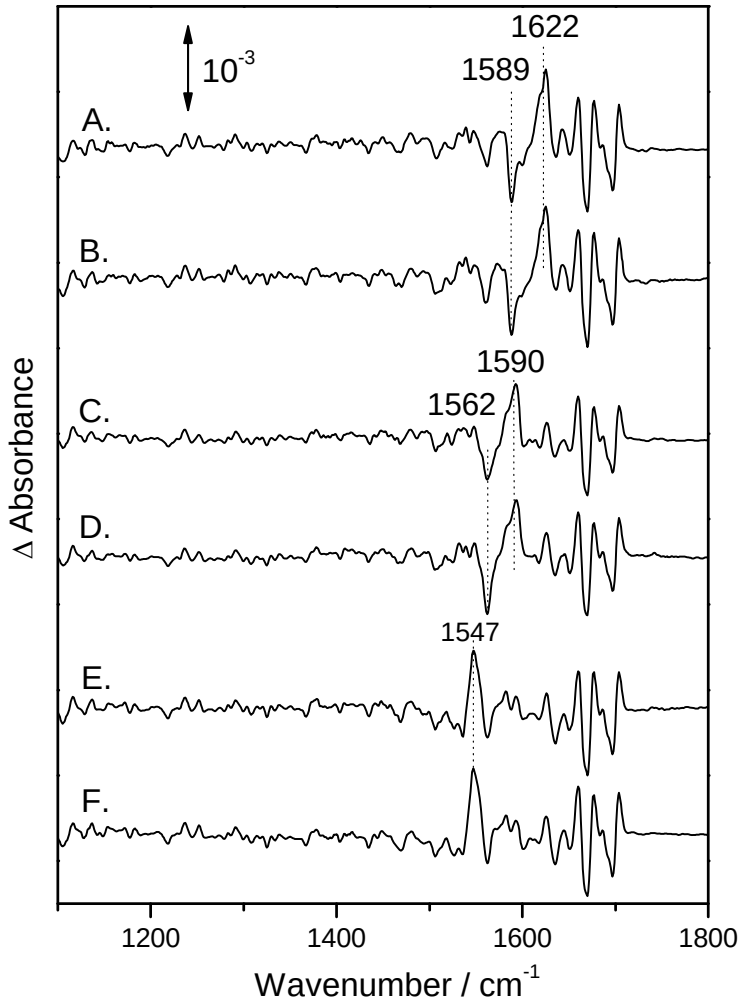

Figure 3.5 Comparison of successive ('dark' minus 'illuminated') FTIR difference spectra obtained after annealing above 90 K for ba_3- NO (A. and B.), ba_3(^{15}NO) (C. and D.), and ba_3(^{15}N^{18}O) (E. and F.).

Low-temperature RR experiments were carried out to compare the porphyrin vibrational modes of the ferrous heme a_3 in the fully-reduced enzyme with those in the photolyzed ba_3(NO) complex. A 442-nm excitation provides selective enhancement of the 5-coordinate high-spin ferrous heme a_3 vibrations, and the fully-reduced ba_3 exhibits two low-frequency modes at 193 and 209 cm^{-1} that have been assigned to heme a_3 iron(II)-histidine stretches on the basis of their downshift with ^{57}Fe (Oertling *et al.*, 1994; Gerscher *et al.*, 1999). While these two bands are of comparable intensity at 10 °C (Oertling *et al.*, 1994), at 30 K they are replaced by a single ν(Fea_3-His) band at 214 cm^{-1}

(Figure 3.6, top black trace). When the same experimental conditions are used with $ba_3(^{14}N^{16}O)$ and $ba_3(^{15}N^{18}O)$ samples at 30 K (Figure 3.6, bottom black and grey traces), the 442-nm laser line provides an effective means of fully dissociating the heme a_3-nitrosyl complex, and an intense RR band at 215 cm^{-1} is assigned to the ν(Fea_3-His) in the photolyzed ba_3(NO) complex. The 1-cm^{-1} up-shift of the ν(Fea_3-His) in the photodissociated state relative to the resting state of the fully-reduced enzyme is reminiscent of the 6- to 8-cm^{-1} up-shift observed with the CO complex of bovine HCO in nanosecond to sub-millisecond timescales (Findsen *et al.*, 1987). These data suggest that subsequent to NO dissociation, the heme a_3 is trapped in a non-equilibrium conformation. The detection of this ν(Fea_3-His) mode confirms that, following the photolysis of NO from heme a_3, Fea_3^{II} is in a 5-coordinate high-spin state equivalent to that of the fully-reduced resting enzyme and thus, is not involved in a bridging coordination of the photolyzed NO with Cu_B^I.

Figure 3.6 shows RR spectra of the ba_3(NO) samples obtained at 180 K, where rapid rebinding of the photolyzed NO to the heme a_3 occurs and prevents accumulation of the photolyzed state (bottom blue and green traces). Because ν(Fe-His) modes are resonance enhanced only in 5-coordinate high-spin Fe^{II} heme species, no ν(Fea_3-His) is detected in the ba_3(NO) samples at 180 K with 442-nm excitation. Under these condition, only weak pre-resonance Raman bands for both heme a_3-NO and the low-spin heme *b* are observed. In contrast, the fully-reduced enzyme continues to display ν(Fe-His) modes similar to those observed at 30 K (Figure 3.6). RR experiments with 413-nm excitation at 180 K also confirm the presence of heme a_3-NO complexes (Figure 3.7). Specifically, the heme a_3-NO complex displays porphyrin skeletal modes ν_4, ν_3, ν_2, and ν_{10} at 1370, 1496, 1595, and 1632 cm^{-1}, respectively, and an NO-isotope sensitive band at 544 cm^{-1} that shifts by -17 cm^{-1} with $^{15}N^{18}O$. This band at 544 (-17) cm^{-1} is typically assigned to ν(Fe-NO) (Stong, 1980; Tsubaki and Yu, 1982; Coyle *et al.*, 2003). However, using nuclear resonance vibrational spectroscopy (NRVS) combined with normal coordination analyses, Lehnert et al. favor a reassignment of Fe-N-O vibrations in the 520-580 cm^{-1} region to modes dominated by Fe-N-O bending character and only minor contributions from Fe-NO stretching displacement (Lehnert *et al.*, 2010). As with the low-temperature UV-vis data, and in contrast with the EPR data, the low-temperature RR spectra provide

no evidence for the presence of a significant 5-coordinate heme-nitrosyl population. Indeed, 5-coordinate heme $\{FeNO\}^7$ species display porphyrin modes that are upshifted ~5 cm^{-1} from their 6-coordinate counterparts. Their ν(Fe-NO) and ν(N-O) modes are also affected by the absence of a sixth *trans* ligand which facilitates the back-donation of electron density from Fe d-orbital to nitrosyl π^*-orbital, and are typically observed at ~ -20 cm^{-1} and ~ +50 cm^{-1}, respectively, from their 6-coordinate counterparts.

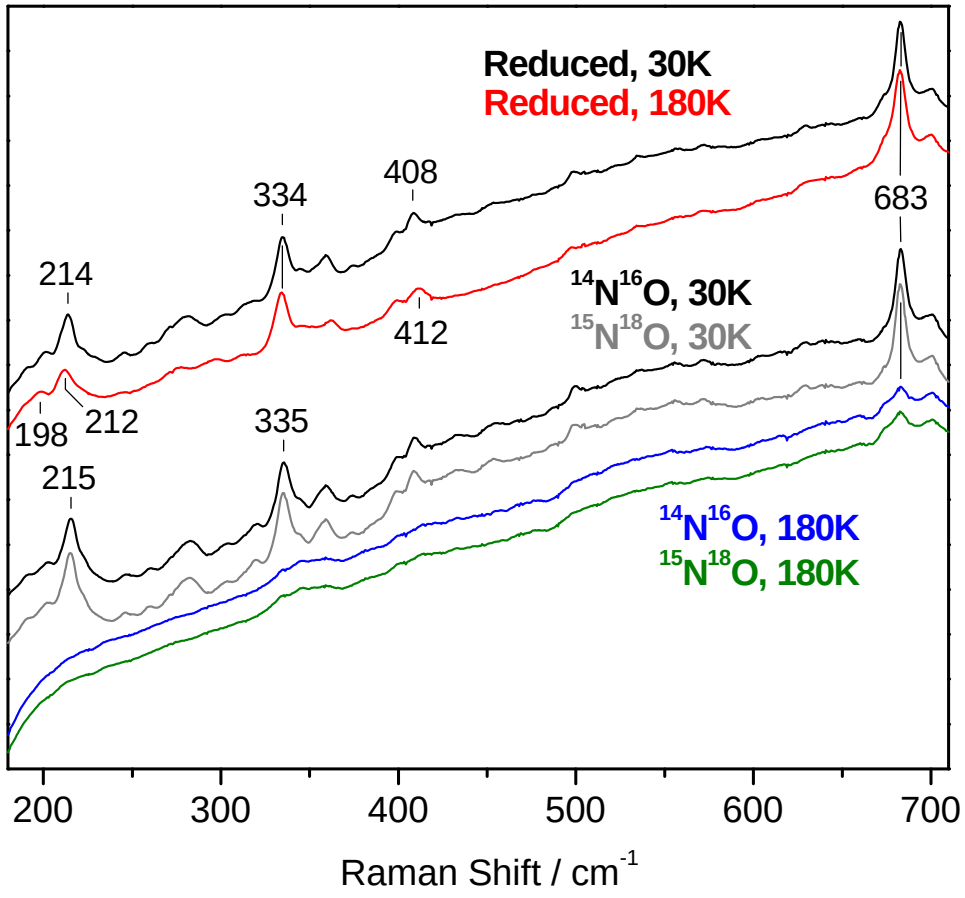

Figure 3.6 RR spectra obtained with 442-nm excitation at cryogenic temperatures. Top traces: reduced ba_3 at 30 (black) and 180 K (red). Bottom traces: ba_3(NO) and ba_3($^{15}N^{18}O$) at 30 (black and grey) and 180 K (blue and green).

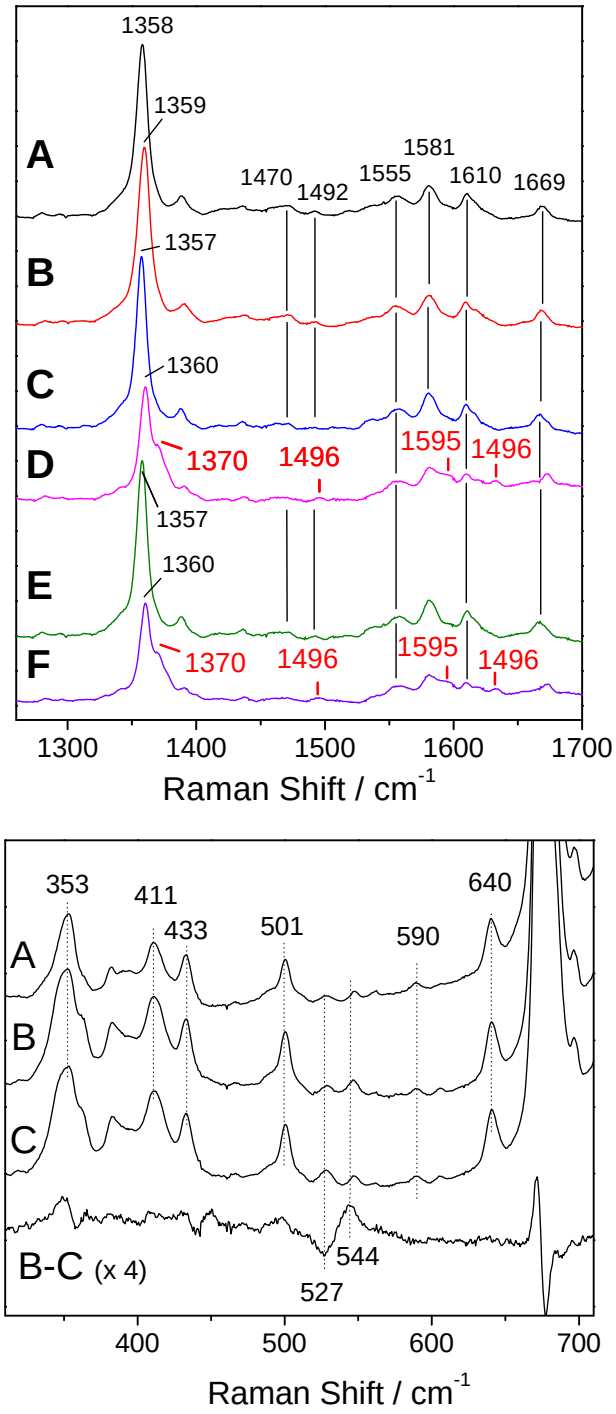

Figure 3.7 High-frequency rR spectra, obtained with 413-nm excitation (Top). Fully-reduced ba_3 at 30 (A) and 180 K (B); $ba_3(^{14}N^{16}O)$ at 30 (C) and 180 K (D); $ba_3(^{15}N^{18}O)$ at 30 (E) and 180 K (F). The porphyrin modes assigned to the heme a_3-nitrosyl adducts are labeled in red. Low-frequency rR spectra, obtained with 413-nm excitation (bottom). Fully-reduced ba_3 (A), $ba_3(^{14}N^{16}O)$ (B), $ba_3(^{15}N^{18}O)$ (C) at 180 K

3.6 Discussion

Fully reduced *ba*$_3$ exhibit high affinities for NO, and formation of heme *a*$_3$-nitrosyl complexes is demonstrated by UV-vis, EPR, and vibrational spectroscopies (Blokzijl-Homan and van Gelder, 1971; Stevens *et al.*, 1979; Brudvig *et al.*, 1980; Mascarenhas *et al.*, 1983; Blackmore *et al.*, 1991; Zhao *et al.*, 1994; Vos *et al.*, 2001; Pinakoulaki *et al.*, 2005). In bovine C*c*O, at high NO concentration, evidence for the binding of a second NO molecule to Cu_B^I is based on the disappearance of the *a*$_3$-NO EPR signal and the detection of two ν(NO)s in the FTIR spectra: one at 1610 cm^{-1} assigned to *a*$_3$-NO, and one at 1700 cm^{-1} assigned to Cu_B^I-NO (Brudvig *et al.*, 1980; Zhao *et al.*, 1994; Pilet *et al.*, 2007). Only a few Cu-nitrosyl complexes have been fully characterized so far, but N_3-Cu-NO model compounds synthesized by Tolman and coworkers have ν(N-O) between 1712 and 1753 cm^{-1}, in good agreement with the data on bovine C*c*O(NO) (Ruggiero *et al.*, 1993; Schneider *et al.*, 1998). Presumably, the lack of NO reductase activity in bovine HCO allows for the accumulation of a stable [$\{FeNO\}^7/\{CuNO\}^{11}$] complex. In contrast, binding of a second NO molecule in *ba*$_3$(NO) is proposed to result in the formation of the N-N bond and the eventual release of N_2O (Pinakoulaki *et al.*, 2005). Whether Cu_B^I in *ba*$_3$ binds NO, even transiently, remains unclear since the attack of *a*$_3$-NO by a second NO molecule may occur without its coordination to Cu_B^I (Blomberg *et al.*, 2006). Flash photolysis experiments on the *ba*$_3$(NO) complex carried out at room temperature reveal efficient geminate rebinding of NO to the heme *a*$_3$ with a time constant of 15 ns (Pilet *et al.*, 2004). This rapid rebinding rate precludes characterization of the photolyzed state of *ba*$_3$ using step-scan FTIR spectroscopy since the time resolution of this technique is limited to the μs range (Pinakoulaki *et al.*, 2005).

Using cryogenic temperatures, we were able to trap the photolysis product of *ba*$_3$(NO) and identify a novel ν(NO) at 1589 cm^{-1}. The efficient formation of this photolyzed state by illumination of the *ba*$_3$(NO) complex with a diffuse 50-W white light limits the realm of this photoprocess to the dissociation of the exogenous ligand from heme *a*$_3$, as previously observed with *ba*$_3$(CO). Low-temperature UV-vis and RR spectra suggest that the heme *a*$_3$ does not interact with the photolyzed NO group in any significant manner, and thus, by analogy with the photolysis process in *ba*$_3$(CO), the

novel ν(NO) at 1589 cm^{-1} is assigned to a Cu_B-nitrosyl complex. However, this ν(NO) frequency is exceptionally low and contrasts with terminally-bound M-NO complexes, which typically display ν(NO)s above 1650 cm^{-1} (Nakamoto, 1997). A bridging coordination of the photolyzed NO group between heme a_3 and Cu_B may explain the observed ν(NO) since multinuclear inorganic complexes with bridging nitrosyl groups adopt μ-1,1 N-bound bridging geometries with ν(NO)s near 1500 cm^{-1} (Nakamoto, 1997). This interpretation however, is not supported by the UV-vis and RR features of the heme a_3 in the photolyzed ba_3(NO) complex which are practically indistinguishable from those of the histidine-bound 5-coordinate heme a_3^{II}. Thus, we favor an assignment of the 1589-cm^{-1} ν(NO) to an NO bound to Cu_B^I either in an O-bound or side-on geometry. Precedent for such NO coordination to transition metals is beginning to accumulate (Coppens *et al.*, 2002; Novozhilova *et al.*, 2006). Light-induced isomerization of (Jasinski *et al.*)^6, $\{RuNO\}^6$, $\{FeNO\}^6$ and $\{FeNO\}^7$ complexes to O-bound and/or side-on conformers are associated with large downshifts in ν(NO) (Fomitchev and Coppens, 1996; Fomitchev *et al.*, 1999; Cheng *et al.*, 2000). In the case of porphyrin $\{FeNO\}^7$ models, N-bound isomers, with ν(NO)s near 1670 cm^{-1}, experience downshifts of ~140 cm^{-1} upon light-induced isomerization (Cheng *et al.*, 2000). O-bound isomers of $\{CuNO\}^{11}$ species have yet to be reported, but this is hardly surprising in view of the scarcity of characterized $\{CuNO\}^{11}$ species as a whole. While the investigation of Cu-nitrosyl complexes in metalloproteins is equally scarce, the type-II copper of nitrite reductase has been shown, crystallographically, to coordinate NO with a side-on geometry (Tocheva *et al.*, 2004; Antonyuk *et al.*, 2005). More recently and subsequently to publication of our work, formation of a side-on Cu_B-NO complex has been reported on bovine HCO under white-light illumination at 50 K (Ohta *et al.*, 2010) (Figure 3.9). Thus, it is tempting to propose an equivalent side-on geometry for the Cu_B-nitrosyl complex in *Tt* ba_3.

The low ν(NO) in the photolysis product of ba_3(NO) suggests a $\{CuNO\}^{11}$ species that should be viewed as a Cu_B^{II}-NO^- rather than a Cu_B^I-NO species. The latter formulation implies a cuprous d^{10} electronic configuration with an $S = 1/2$ NO ligand and is expected to produce an overall $S = 1/2$ species with an EPR signal centered around g ~ 2. In contrast, a Cu_B^{II}-NO^- formulation suggests an $S = 1/2$ cupric center coupled to an S

= 1 NO^- ligand to produce an $S = 3/2$ or $S = 1/2$ species depending on whether ferromagnetic or antiferromagnetic coupling occurs. The latter description of the $\{CuNO\}^{11}$ species is equivalent to that of a non-heme $\{FeNO\}^7$ species, which is described as an $S = 3/2$ species with an $S = 5/2$ high-spin ferric center antiferromagnetically coupled to an $S = 1$ NO^- ligand (Brown *et al.*, 1995). Based on this analogy, an EPR signal at $g \sim 4$ or $g \sim 2$ would be expected for the Cu_B-nitrosyl complex in ba_3; however, despite our efforts, we were not able to detect an EPR signal associated with the photolyzed state of the enzyme. The lack of an EPR signal may originate from a rapid intramolecular electron transfer between Cu^I and $NO^\bullet$ that results in signal broadening beyond detection. Magnetic coupling of the $\{CuNO\}^{11}$ species with the $S = 2$ high-spin ferrous heme a_3 may also render the heme/Cu dinuclear center EPR silent. Finally, environmental effects could also play an important role in the EPR silent character of some $\{CuNO\}^{11}$ species since Tolman and coworkers have noted that the addition of π-electron systems into the surrounding of Cu-NO model complexes can result in the disappearance of EPR activity (Schneider *et al.*, 1998).

Our EPR data obtained prior to photolysis also deserve further discussion. The 9-line and 3-line g ~ 2 signals observed in our experiments with ba_3(NO) are similar to those reported earlier for heme a_3-NO complexes in other terminal oxidases (Pearce *et al.*, 2003; Pilet *et al.*, 2004), but the presence of these two populations in ba_3(NO) is in apparent conflict with earlier reports by Pilet and coworkers (Pilet *et al.*, 2004; Pilet *et al.*, 2007). Indeed, while Pilet et al. observed both the 9-line and 3-line EPR features in *P. denitrificans* aa_3(NO), they observed no 3-line signal in their EPR spectra of ba_3(NO) (Pilet *et al.*, 2004). In *P. denitrificans* aa_3(NO), the appearance of the 3-line $g \sim 2$ signal was dependent on the number of NO equiv added and was accompanied by a second signal at $g \sim 4$ assigned to an $S = 3/2$ Cu_B-NO complex (Pilet *et al.*, 2004). These same authors have proposed that binding of a second NO molecule at the heme/Cu site results in a reorientation of heme a_3 proximal histidine plane perpendicular to, rather than parallel to, the plane of the Fe-N-O unit. However, the structural event that leads to the heme a_3-NO 3-line EPR signal in *Tt* ba_3 must be different since our measurements show that the 3-line $g \sim 2$ signal is observed without the accompanying $g \sim 4$ signal and without a clear dependence on the NO concentration. Additionally, the presence of two

NO molecules in the active site of *ba*$_3$ is expected to represent a highly reactive intermediate within the NO reductase turnover.

Several structural characteristics may determine the proficiency of a given terminal oxidase with regard to NO reductase activity, and proposing distinct isomer forms of Cu_B-nitrosyl complexes in terminal oxidases has mechanistic significance. For example, the distance between the two metal ions at the active site is likely to be important for NO reductase activity. In *P. denitrificans* cNOR, the iron-iron distance is ≤3.5 Å and could favor the formation of an N-N bond between two metal-nitrosyl complexes (Moënne-Loccoz *et al.*, 2000; Moënne-Loccoz, 2007). Crystal structures of terminal oxidases have revealed a range of Fe*a*$_3$-Cu_B distances. In oxidized *Tt ba*$_3$, the heme-copper distance is 4.4 Å (Soulimane *et al.*, 2000; Hunsicker-Wang *et al.*, 2005), while in bovine C*c*O, it varies between 4.9 and 5.3 Å depending on the state of the enzymes (Yoshikawa *et al.*, 1998). Similarly, in *P. denitrifcans aa*$_3$ the Fe*a*$_3$-Cu_B distance varies between 4.5 and 5.2 Å depending on the presence of an auxiliary subunit complementing the subunit I/subunit II core complex (Iwata *et al.*, 1995; Ostermeier *et al.*, 1997). Also noteworthy is the observation that heme-copper terminal oxidases form both 5- and 6-coordinate heme $\{FeNO\}^7$ species (Pinakoulaki *et al.*, 2002; Pearce *et al.*, 2003; Pilet *et al.*, 2004; Pinakoulaki *et al.*, 2005). Undoubtedly, the coordination numbers must impact the fate of the NO reaction at the dinuclear active site. Our current data suggest that the manner in which Cu_B^I interacts with NO, i.e., through an N-bound, side-on, or O-bound complex, may also determine whether or not NO reductase activity will be observed. Specifically, while a heme/non-heme $[\{FeNO\}^7]_2$ complex in cNOR is believed to be catalytically competent (Kumita *et al.*, 2004), the formation of an N-bound Cu_B-NO complex in bovine *aa*$_3$ may lead to an inhibitory $[\{FeNO\}^7\{CuNO\}^{11}]$ dead-end complex (Figure 3.8C). Instead, the NO reductase activity in *Tt ba*$_3$ may be based on the formation of a $\{CuON\}^{11}$ species or the concerted formation of Cu_B-O and N-N bond between a free NO molecule and the heme *a*$_3$-nitrosyl complex to form a bridging hyponitrite between Cu_B and Fe*a*$_3$ (Figure 3.8B).

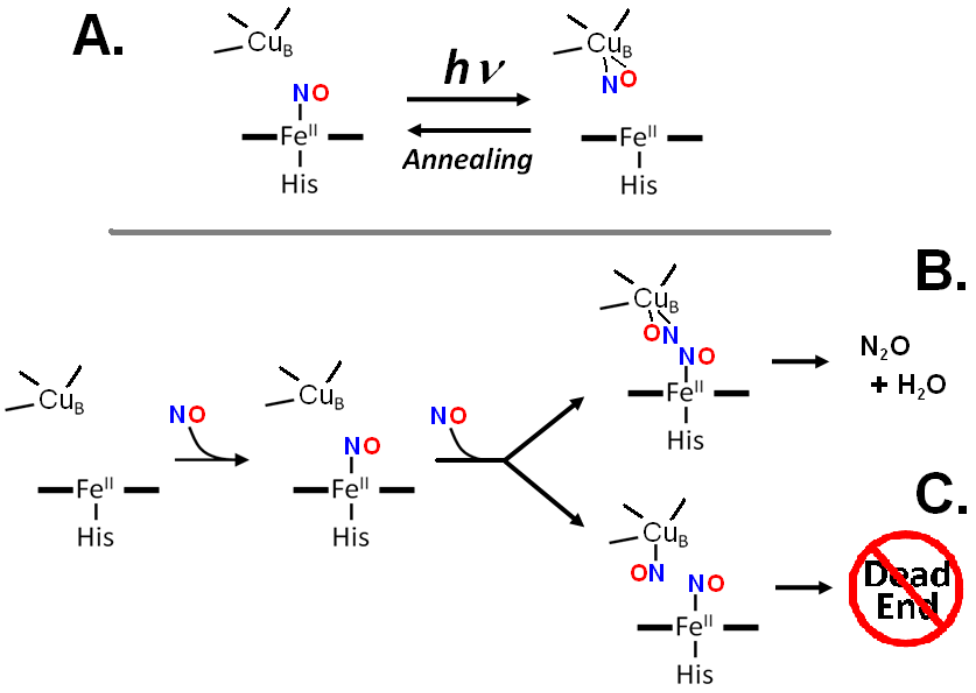

Figure 3.8 The photolysis process observed in *ba*$_3$(NO) (A) and putative mechanisms for NO reductase reaction in terminal oxidases (B). Also shown is expected formation of a [{FeNO}^{7}{CuNO}^{11}] dead-end complex in non-NO reductase active bovine *aa*$_3$ (C).

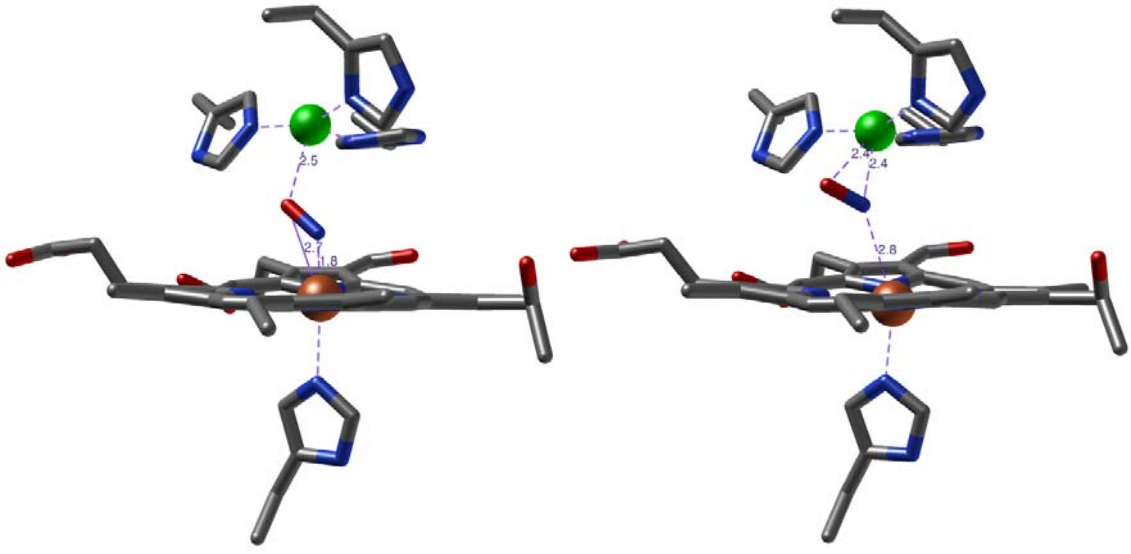

Figure 3.9 Crystal structures of the NO-bound *aa*$_3$ at 100 K (left) and at 50 K under light illumination (right) of bovine heart *aa*$_3$ (PDB code: 3AG3 and 3ABK). The peripheral side chain and cross-linked tyrosine are omitted in order to better visualize the heme/copper center.

CHAPTER 4

CHARACTERIZATION OF [o_3-NO • OC-Cu_B] COMPLEX IN CYTOCHROME bo_3

4.1 Cytochrome bo_3 from *Escherichia coli*

In the previous chapter, we reported a cryogenic FTIR photolysis study of the NO complex of cytochrome ba_3 from *Thermus thermophilus*. The results show the formation of a transient Cu_B-nitrosyl species with an unusual N-O stretching frequency suggestive of an O-bound (η^1-O) or side-on (η^2-NO) configuration. The characterization of this complex suggested that the N-N bond formation in ba_3 does not proceed from a [a_3-NO • ON-Cu_B] trans ba_3-$(NO)_2$ complex as proposed by Ohta and coworkers (Ohta *et al.*, 2006). Instead, we speculated that the photo-induced Cu_B-nitrosyl species describes the mode of binding of the second NO molecule during the NO reduction turnover.

To determine whether the hypothesis drawn with ba_3 apply to other terminal oxidases with NO reductase activity, we now direct our effort to the bo_3 ubiquinol oxidase from *Escherichia coli* (Figure 4.1) (Abramson *et al.*, 2000; Butler *et al.*, 2002). Only a few investigations have been focused on the interaction of NO with bo_3 from *E. coli*. Sarti and coworkers measured a low but significant NO reductase activity in bo_3 under reducing condition (Butler *et al.*, 2002). Thomson and coworkers have reported EPR data that led them to propose that two NO molecules bind to Cu_B^{II} in the oxidized form of bo_3 (Butler *et al.*, 1997). To our knowledge, cytochrome bo_3 is the only quinol oxidase reported to exhibit NO reductase activity, and thus, it provide a relevant model for the quinol NOR (qNOR) from *N. gonorrhoeae* and *Neisseria meningitidis* (Anjum *et al.*, 2002).

---

*Material in this chapter has been published in this or similar form in *Biochemistry*, and is used here with permission of the American Chemical Society.

Hayashi T., Lin M.T., Ganesan K., Chen Y., Fee J.A., Gennis R.B., and Moënne-Loccoz P. (2009) Accommodation of Two Diatomic Molecules in Cytochrome bo_3: Insights into NO Reductase Activity in Terminal Oxidases. ***Biochemistry***, 48, 883-890.

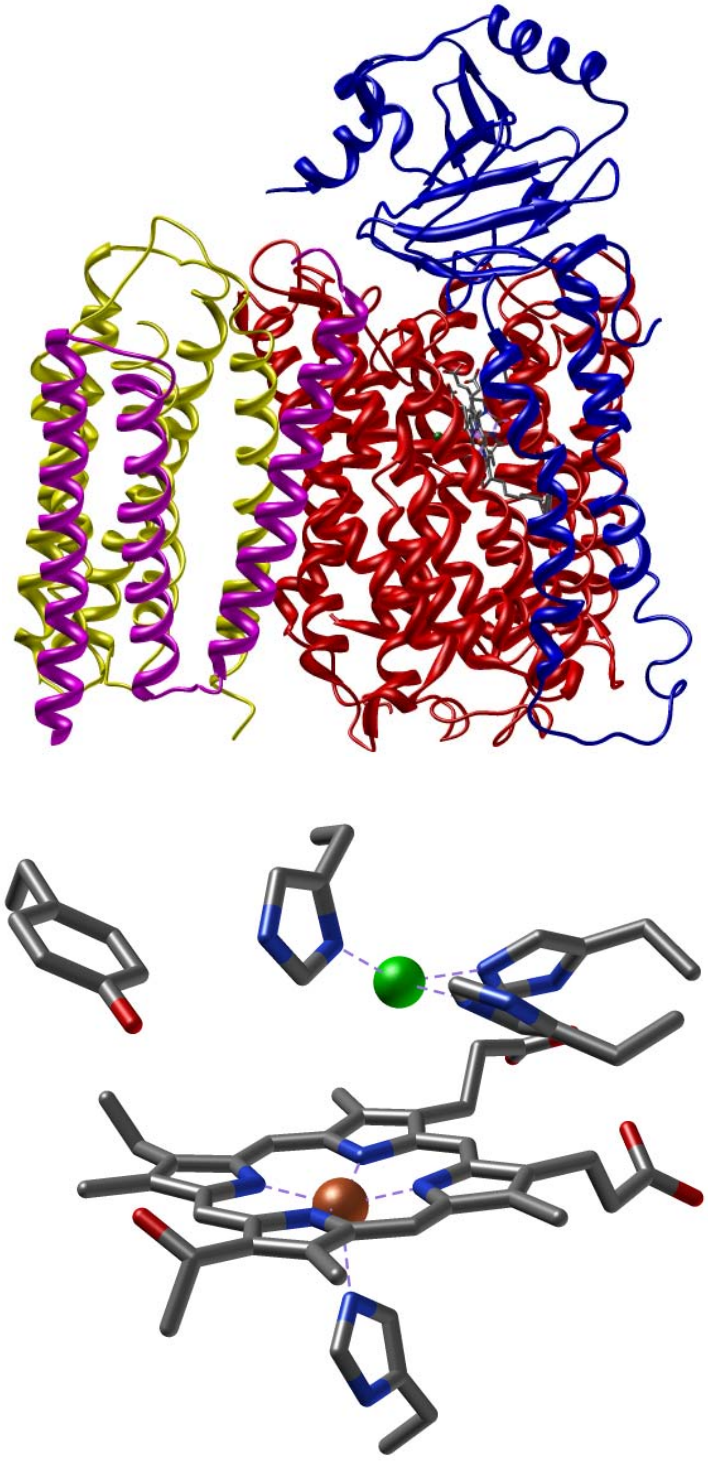

Figure 4.1 Overall structure (top) and zoom-in on the heme/copper center (bottom) of Cytochrome bo_3 from *Escherichia coli* (PDB code: 1FFT). The presence of cross-link between His284 and Tyr288 could not be determined at the resolution of 3.5Å. The peripheral side chain is omitted in order to better visualize the heme/copper center.

Here we report cryogenic FTIR photolysis experiments on fully reduced *bo₃*(NO) and the mixed gas *bo₃*(CO)(NO) complexes. Amperometric measurement of NO concentrations and monitoring of production of N_2O by FTIR spectroscopy demonstrate that *ba₃* and *bo₃* catalyze the same reaction at similar rates. However, the Cu_B-nitrosyl species observed in *ba₃*(NO) does not form in *bo₃*(NO), and instead, the photolyzed NO docks a protein pocket that lead to efficient NO geminate recombination as in ferrous myoglobin(NO) (Miller *et al.*, 1997). FTIR experiments carried out on *bo₃* and *ba₃* exposed to NO/CO mixed gas show simultaneous binding of two diatomic molecules, in the dinuclear site of *bo₃* to form a [o_3-NO • OC-Cu_B] complex which is not observed in *ba₃*. The relevance of this [o_3-NO • OC-Cu_B] state to the NO reductase activity in cytochrome *bo₃* is discussed in the context of other terminal oxidases and of denitrifying NORs.

4.2 Materials and methods

Protein Preparations

The expression and purification of *ba₃* and *bo₃* were performed as previously described (Rumbley *et al.*, 1997; Chen *et al.*, 2005). *ba₃* and *bo₃* were prepared in 20 mM Tris-HCl pH 7.5 with 0.05% dodecyl β-D-maltoside and 50 mM potassium phosphate pH 8.0 with 0.1% dodecyl β-D-maltoside, 10 mM EDTA, and 5% glycerol, respectively.

bo₃(NO) complex was prepared by the method used for *ba₃*(NO). The *bo₃* was fully reduced by addition of dithionite at a final concentration of 10 mM, followed by exposure to 0.1 atm of NO. After one minute of incubation at room temperature, the protein solution was transferred to an IR cell, RR capillary, EPR tube, or UV-vis cuvette. Experiments with 1.0 equivalent NO addition were performed as described in Chapter 2.2. CO/NO mixed gas experiments were carried out with ~500 μM reduced protein solution with 10 mM ascorbate, 0.1 mM TMPD, and 25% glycerol addition. The sample headspace was thoroughly exchanged with CO gas (^{12}CO purchased from Airgas or ^{13}CO purchased from ICON), and after 15 min of incubation at room temperature, 1.0 or 3.0

equiv NO addition was achieved using NONOate. 15 µL of the protein solution was immediately transferred to a FTIR cell with a 15-µm Teflon spacer.

NO reductase activity measurements

NO stock solutions were prepared by bubbling of NO previously treated with 1 M KOH through double distilled water in an anaerobically sealed vessel for ~15 min at 25°C. The concentration of NO in the solution was determined to be 1.5 mM by titration against ferrous Mb. NO reduction measurement was carried out with a Clark-type NO electrode (Figure 4.2) equipped with a 2 ml gas tight sample chamber at 25°C in a glove box containing less than 1ppm O_2 (Omnilab System, Vacuum Atmospheres Company). The electrode polarization was adjusted to +860 mV, at which NO is oxidized to nitrite ($NO + H_2O \rightarrow NO_2^- + 2H^+ + e^-$) (Girsch and de Vries, 1997). The current was stabilized with a buffer solution containing 10 mM ascorbate and 0.1 mM TMPD in the sample chamber, followed by three successive addition of saturated NO solution to reach final NO concentrations of 40 to 60 µM. After stabilization of the NO solution, the reduced enzyme was added and the current monitored until it returned to zero.

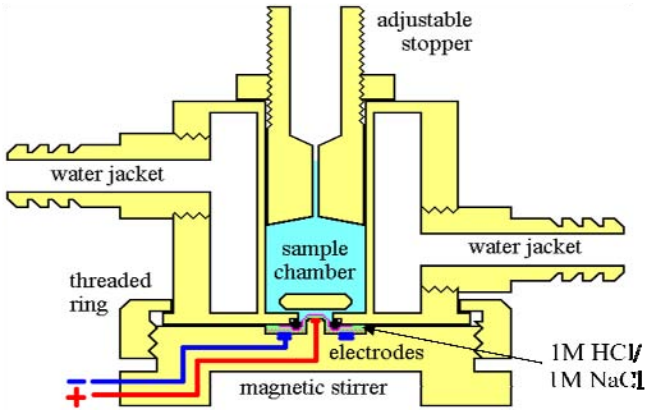

Figure 4.2 Schematic representation of Clark-type NO electrode.

N_2O production measurements

The production of N_2O by the two terminal oxidases was monitoring the ν(NNO) stretch at 2230 cm^{-1} in the FTIR spectra (Zhao *et al.*, 1995). Protein solutions were made anaerobic by prolonged purging with argon on a Schlenk line and brought to a final

enzyme concentration of 50 μM with 10 mM ascorbate and 0.1 mM TMPD in the glove box. Quickly after the addition of NONOate to the protein solution, a 33-μL droplet of sample was deposited on a CaF_2 window and a second CaF_2 window was dropped on the sample. The optical pathlength was controlled by 100-μm Teflon spacer. The FTIR cell was placed in the sample compartment of the FTIR instrument. FTIR spectra were obtained on a Perkin-Elmer system 2000 and sets of 100 scans accumulations were acquired every 2 min at a 4-cm^{-1} resolution until no further growth of the N_2O IR band was observed. These data were compared to a calibration curve obtained from controlled solutions with varying N_2O concentrations.

Molecular spectroscopy

UV-vis, EPR, FTIR and RR spectroscopy were carried out as described in Chapter 2.2. The typical enzyme concentrations for UV-vis, EPR, FTIR and RR spectroscopy are 3, 30, 350, and 120 μM, respectively.

For EPR spectroscopy, 250 μL of *bo*$_3$(NO) complex prepared in an EPR tube was flash-frozen in liquid N_2 after confirming the presence of the NO adduct by UV-vis absorption spectroscopy. Quantitation of the EPR signals was performed under non-saturating conditions by double integration and comparison with 0.1 mM and 0.01 mM Cu^{II}EDTA standards.

The FTIR cell was mounted to a closed-cycle cryogenic system and kept in the dark while the temperature dropped to 30 K (cooling rate ~ 4 K/min). The FTIR spectra were obtained on a Perkin-Elmer system 2000 equipped with a liquid-N_2 cooled MCT detector and purged with compressed air dried and depleted of CO_2. Sets of 1000-scan accumulations were acquired at a 4-cm^{-1} resolution. These data averaging conditions required 15-min, and because of instrumental drift, further accumulation time did not result in an improvement of the FTIR difference spectra. Photolysis of the *bo*$_3$(NO) complex was achieved with continuous illumination of the samples directly in the FTIR sample chamber with a 50 W tungsten lamp after filtering out heat and NIR emission. The same illumination procedure was used to follow the dissociation-rebinding process by UV-vis spectroscopy with the Cary-50 spectrophotometer.

RR sample of reduced *bo₃* and *bo₃*(NO) complexes were prepared in anaerobic Raman capillaries. The RR spectra were collected in a 90° scattering geometry on samples mounted on a reciprocating translation stage at room temperature. Kaiser Optical supernotch filters were used to attenuate Rayleigh scattering generated by the 413-nm excitation. Frequencies were calibrated relative to indene and CCl_4 standards and are accurate to ±1 cm^{-1}. The integrity of the RR samples is confirmed by direct monitoring of their UV-vis absorption spectra in Raman capillaries before and after laser exposure.

4.3 NO reductase activity measurements

Both *ba₃* and *bo₃* have been reported to possess NO reductase activity (Giuffre *et al.*, 1999; Butler *et al.*, 2002), but their steady-state turnover rates have not been compared in side-by-side experiments. Thus, we carried out parallel NO reductase activity measurements on *ba₃* and *bo₃* by monitoring NO consumption amperometrically in reducing conditions (10 mM ascorbate and 0.1 mM TMPD) (Figure 4.3 top). Upon addition of myoglobin, *aa₃*, *ba₃*, and *bo₃*, a rapid initial decay of current is assigned to stoichiometric binding of NO to ferrous high-spin hemes. While no further decay is observed with myoglobin and *aa₃*, *ba₃* and *bo₃* display NO consumption with initial rates of 3.8 mol NO/mol *ba₃*-min and 3.5 mol NO/mol *bo₃*-min at [NO] = 40 μM (Figure 4.3 top). These values match previous report by Giuffre et al. (3.0 ± 0.7 mol NO/mol *ba₃*-min at [NO] = 55 μM) (Giuffre *et al.*, 1999) and complement Butler et al. (0.3 mol NO/mol *ba₃*-min at [NO] = 5 μM) (Butler *et al.*, 2002). It is worth noting that, in the presence of excess reducing agent, both enzymes remain as mononitrosyl-complexes after the turnover measurements (data not shown). This observation indicated that, in both enzymes, the binding affinity for the second NO is much lower than that of the first NO.

The production of N_2O was monitored by FTIR measurement of the antisymmetric N-N-O stretch mode ν_3 of N_2O at 2231 cm^{-1}. Using calibration curves with N_2O saturated solutions, the 2231-cm^{-1} absorption values in *ba₃* and *bo₃* confirm that all the NO consumed is converted to N_2O. (Figure 4.3 bottom).

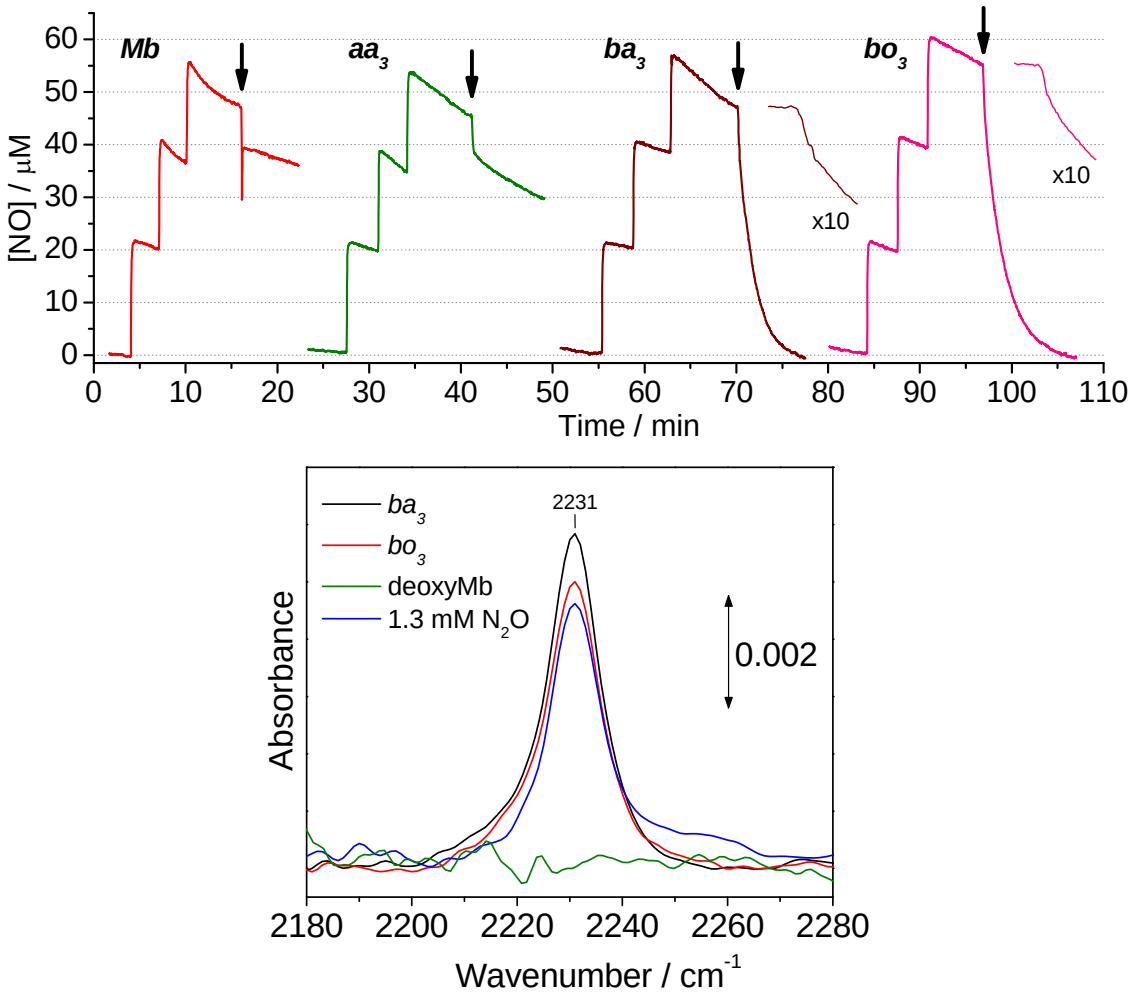

Figure 4.3 NO binding and reductase activity of deoxy myoglobin (Mb), *aa*$_3$, *ba*$_3$, and *bo*$_3$ at 25°C (Top). Black arrows show time points where each enzyme were added to react a final concentration of 7 μM. For *ba*$_3$ and *bo*$_3$, the early part of the trace is also shown expanded 10-times to reveal the initial NO-binding steps. FTIR spectra of *ba*$_3$ and *bo*$_3$ after 15-min incubation with 2.0 mM NO generated from NONOate, 10 mM ascorbate, and 0.1 mM TMPD (Bottom).

4.4 Formation of 6-coordinate *o*$_3$-NO in *Ec bo*$_3$

Similar to *Tt ba*$_3$, extended exposure of fully-reduced *Ec bo*$_3$ to excess NO_g produces an UV-vis spectrum identical to that of fully-oxidized *Ec bo*$_3$, consistent with the NO reductase activity observed above. Exposure of fully-reduced *bo*$_3$ to a headspace containing 0.1 atm NO results in the formation of *bo*$_3$(NO). The Fe^{II} heme-*o*$_3$ Soret

absorption at 427 nm is blue-shifted to generate a new Soret band at 417 nm, and there are only minor changes in the visible range of the room-temperature absorption spectra (Figure 4.4A). The Soret absorption, assigned to the heme-o_3-NO complex, is also observed at 30 K, but disappears following illumination (Figure 4.4B). As reported previously (Cheesman *et al.*, 1993), the EPR spectrum of the bo_3(NO) complex is characteristic of a 6-coordinate low-spin heme iron(II)-nitrosyl species with spectral parameters equivalent to those observed in ba_3(NO) (Figure 4.5). In addition, this EPR spectrum includes an easily saturated, isotropic g = 2.005 with a 10 G linewidth which was previously assigned to a semi-quinone radical (Yap *et al.*, 2006; Yap *et al.*, 2007). Unlike the EPR features associated with the heme o_3-NO, this signal is insensitive to short illumination at cryogenic temperatures (Figure 4.5). The only new EPR signal observed after illumination is that of free NO at g = 1.97, which is best observed at high microwave power and below 10 K (data not shown). Thus, the low-temperature UV-vis and EPR data reveal efficient NO photolysis from heme o_3 to form a stable photolyzed state at 30 K.

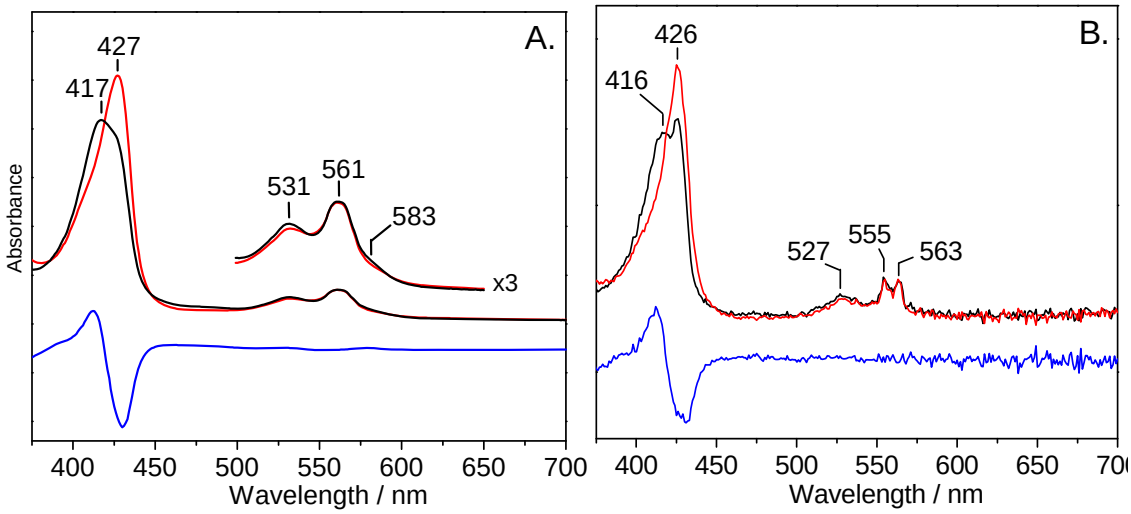

Figure 4.4 UV-vis absorption spectra of fully reduced cytochrome bo_3 (red) and the bo_3(NO) complex (black), and 'ba_3(NO)' minus 'fully reduced bo_3' difference spectrum (blue) obtained at room temperature (A); and of the bo_3(NO) complex before (black) and after illumination (red), and 'dark' minus 'illuminated' difference spectrum (blue) obtained at 30 K (B).

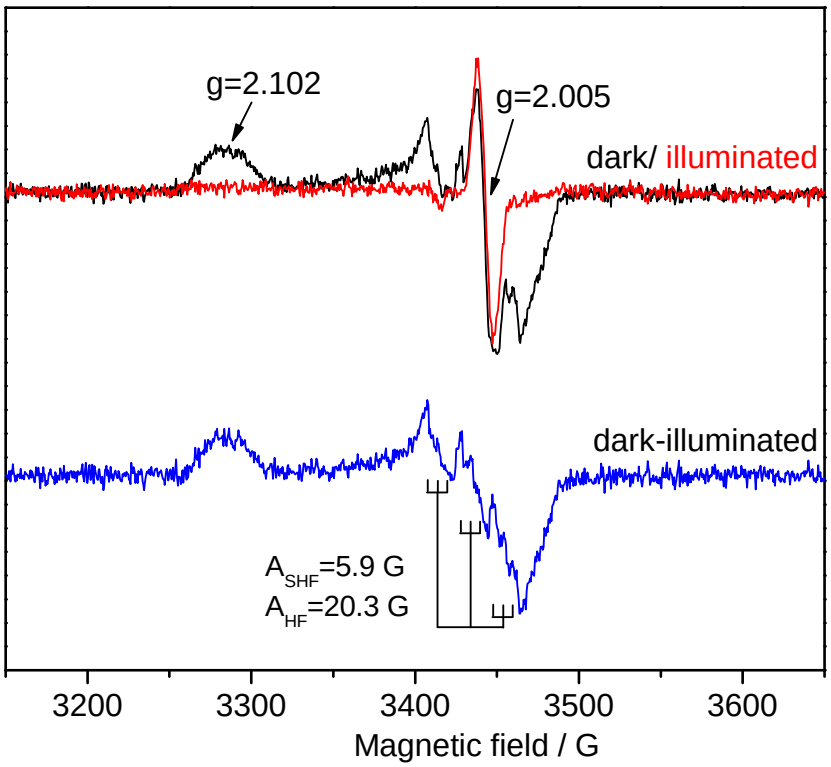

Figure 4.5 EPR spectra of *bo*$_3$(NO) at 30 K. Spectrum taken in dark (black), after illumination (red), and the 'dark' minus 'illuminated' difference spectrum (blue). Conditions: protein concentration, 30 μM; temperature, 30 K; microwave power, 0.04 mW; modulation amplitude, 2G; microwave frequency, 9.66 GHz.

RR spectra of the *bo*$_3$(NO) complex, obtained with a 413-nm excitation at room temperature, display enhancement of vibrational modes from the heme *o*$_3$-NO complex (Figure 4.6). The porphyrin skeletal modes ν_4, ν_3, ν_2, and ν_{10} at 1361, 1504, 1587, and 1638 cm^{-1}, respectively, are characteristic of a 6-coordinate low-spin heme-nitrosyl species. Vibrational modes involving the Fe-N-O unit are identified by their $^{15}N^{18}O$-downshifts (Figure 4.6). The ν(N-O)*o*$_3$ mode is observed at 1615 cm^{-1} and exhibits a 67-cm^{-1} downshift with $^{15}N^{18}O$ that is within 5-cm^{-1} of the calculated shift for a diatomic N-O oscillator. Two bands, at 534 (-17) and 440 (-13) cm^{-1}, are assigned to δ(Fe-NO) and ν(Fe-NO) modes, respectively, according to theoretical work from Lehnert et al.(Lehnert *et al.*, 2010). The unusually intense ν(Fe-NO) band, which is not observed in *ba*$_3$(NO)

(Pinakoulaki *et al.*, 2005), and the low δ(Fe-NO) frequency suggest that the Fe-N-O angle is smaller than the 140° equilibrium value. The low ν(N-O)o_3 frequency is also consistent with a small Fe-N-O angle which favors the $Fe^{III}NO^{-}$ resonance structure and N-O double-bond character.

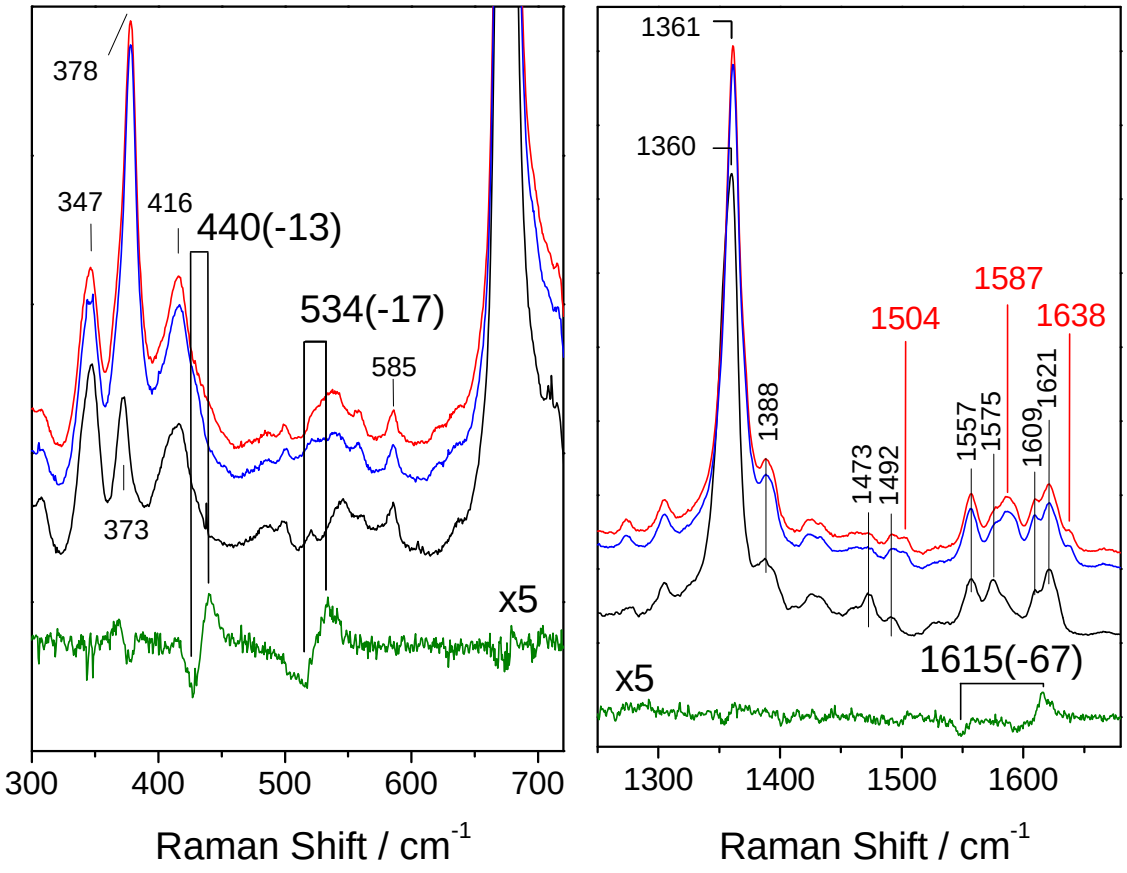

Figure 4.6 Low- and high-frequency RR spectra of $bo_3(^{14}N^{16}O)$ (red), $bo_3(^{15}N^{18}O)$ (blue), reduced bo_3 (black), and the '$bo_3(^{14}N^{16}O)$' minus '$bo_3(^{15}N^{18}O)$' difference spectrum (green) obtained with a 413-nm excitation at room temperature.

.

4.5 Concomitant binding of NO and CO in *bo₃*

bo₃(NO) complex

As done previously with *ba₃*(NO) (chapter 3), we use cryogenic photolysis experiments to isolate ν(N-O) vibrations in 'dark' minus 'illuminated' FTIR difference spectra. In *ba₃*(NO), these experiments revealed the disappearance of a ν(N-O)*a₃* at 1622 cm^{-1}, consistent with the dissociation of NO from the heme, and a negative ν(N-O)Cu_B at 1589 cm^{-1} corresponding to the formation of a Cu_B-nitrosyl complex. In the case of *bo₃*(NO), the FTIR 'dark' minus 'illuminated' difference spectrum shows a sharp positive band at 1610 cm^{-1} that is readily assigned to the ν(N-O)*o₃* by its 30-cm^{-1} downshift with ^{15}NO, but there are no negative signals below 1800 cm^{-1} that might be suggestive of a Cu_B-nitrosyl species (Figure 4.7). Instead, a negative band at 1863 cm^{-1} that shifts -34 cm^{-1} with ^{15}NO is characteristic of a ν(N-O) from an NO molecule docked in a proteinaceous pocket, as observed with the nitrosyl complex of myoglobin (Miller *et al.*, 1997). Changing buffer and salt conditions had no effect on the FTIR difference spectra of *bo₃*(NO) (Figure 4.8). Thus, these experiments suggest that, despite the structural similarities of the heme-copper sites in these two terminal oxidases (Abramson *et al.*, 2000; Soulimane *et al.*, 2000) and despite efficient capture of photolyzed CO by Cu_B^I in both terminal oxidases, NO transfer from the heme to Cu_B does not occur in *bo₃*.

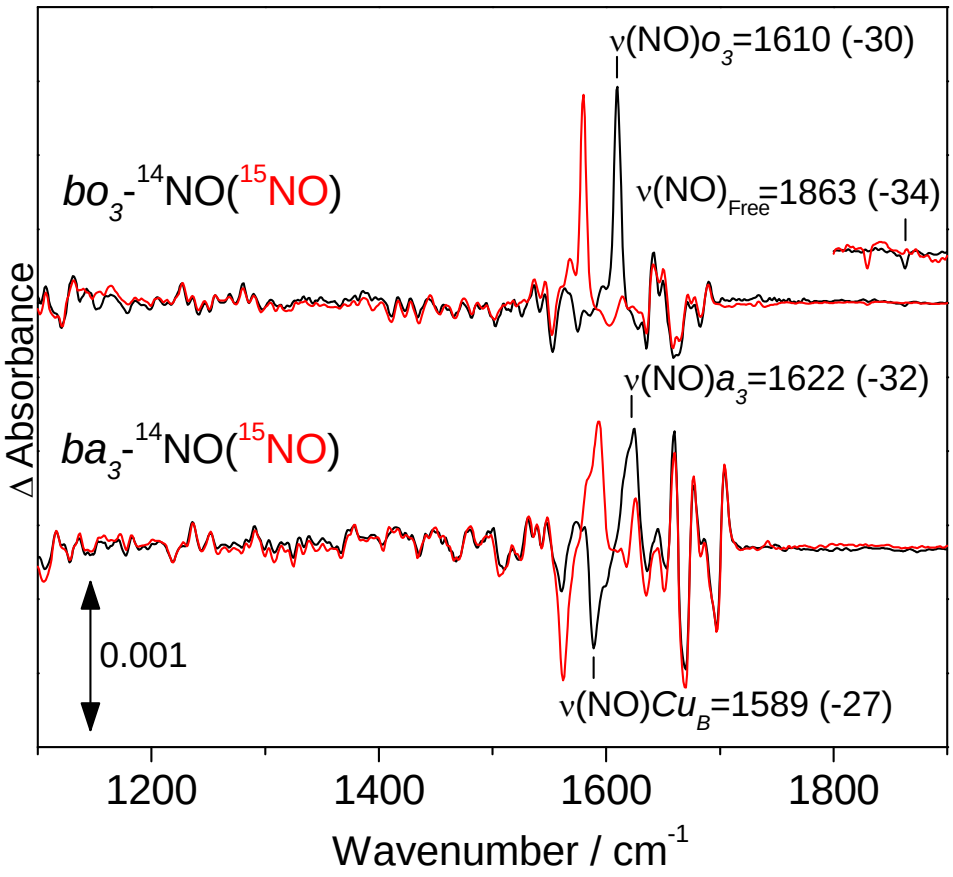

Figure 4.7 FTIR 'dark' minus 'illuminated' difference spectra of *bo*$_3$(NO) (top traces) and *ba*$_3$(NO) (bottom traces) at 30 K. The spectra were obtained with protein concentration near 350 μM and were normalized based on the room temperature UV-vis spectra obtained directly from the FTIR cell.

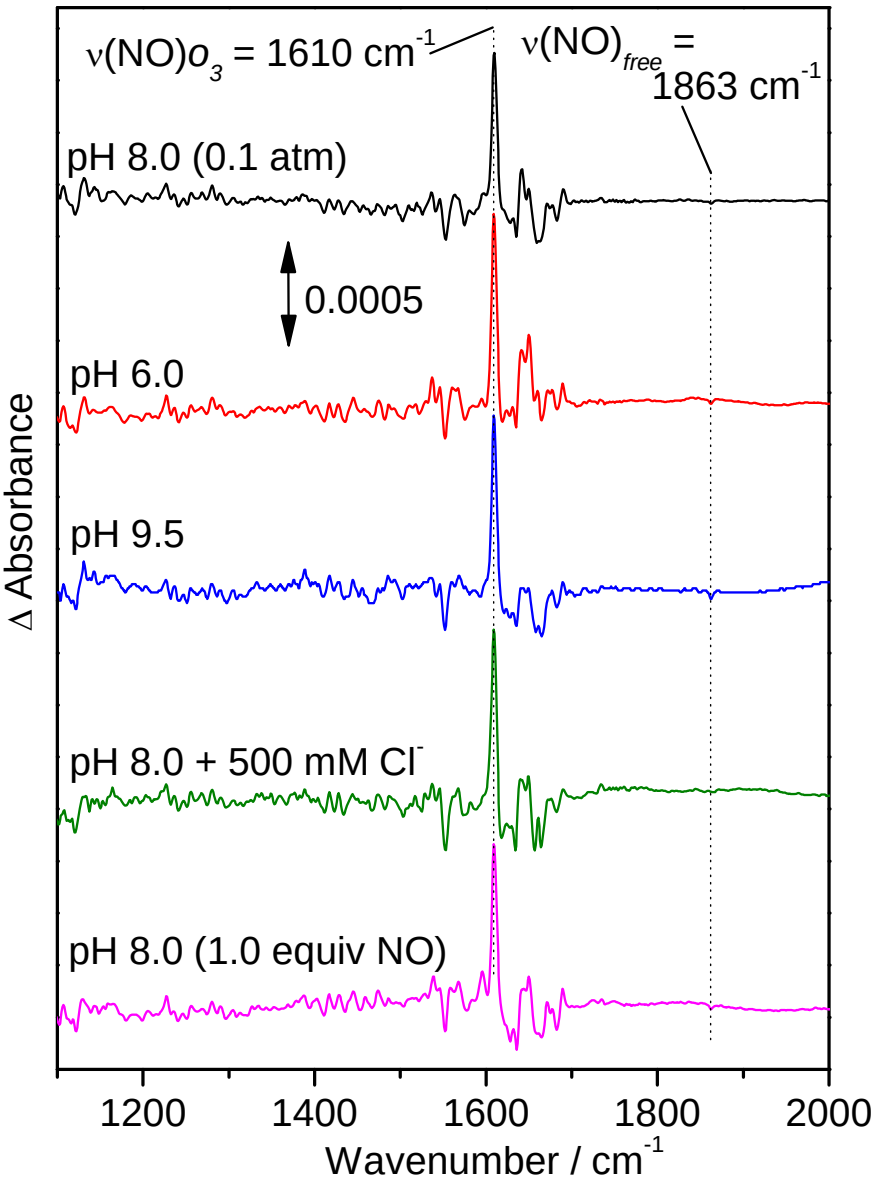

Figure 4.8 FTIR 'dark' minus 'illuminated' difference spectra of *bo*$_3$(NO) complex formed after exposure to 0.1 atm NO addition at pH 8.0 (black), pH 6.0 (red), pH 9.5 (blue), at pH 8.0 with 500 mM NaCl (green), and at pH 8.0 with 1.0 equiv NO addition (magenta) at 30 K. The spectra were obtained with protein concentration near 350 μM and were normalized based on the room temperature UV-vis spectra obtained directly from the FTIR cell.

bo_3(NO)(CO) complex

To gain further insight into the catalytically-relevant step where two NO molecules interact with the heme-copper, we carried out experiments with consecutive exposure of reduced *ba_3* and *bo_3* proteins to CO and NO gases, and succeeded in forming a [*o_3*-NO • OC-Cu_B] complex in *bo_3*. In *ba_3*, exposure of *ba_3*(CO), in the presence of excess CO, to 3 equiv of NO minutes before freezing (see experimental section) resulted in the formation of *ba_3*(NO) and *ba_3*(CO) complexes that were easily distinguishable in the FTIR spectra (Figure 4.9). While rebinding of the photolyzed CO required annealing the sample above 220 K, the rebinding of NO was complete after annealing at 100 K. This difference in rebinding temperature allows the separation of FTIR features associated with *ba_3*(NO) and *ba_3*(CO). When the same experiment was carried out with *bo_3*, features in the FTIR difference spectra associated with *bo_3*(NO) and *bo_3*(CO) complexes were also observed (Figure 4.10 A and B); however, the NO dissociation process induces a differential signal in the ν(C-O)Cu_B region that shifts –47 cm^{-1} with ^{13}CO (Figure 4.9). We assign this signal, centered at 2057 cm^{-1}, to a perturbation of the Cu_B-carbonyl as NO is dissociated from heme *o_3* (Figure 4.10 C). The ν(NO)*o_3* in these mixed-gas experiments is observed at 1610 cm^{-1} and is indistinguishable from the ν(NO)*o_3* observed when the complex is formed with pure NO. The relative intensities of the ν(N-O)*o_3* and ν(C-O)*o_3* bands suggest that the active site in the *bo_3*(CO) state represents only 10% of the sample, while the remaining 90% contains the heme *o_3*-NO complex. Furthermore, on the basis of the ν(C-O)Cu_B band observed in the 'dark' spectrum (Figure 4.11), we estimate that out of the 90% of nitrosylated active site, at least 10% binds CO to form the [*o_3*-NO • OC-Cu_B] complex. Thus, although the active site of *bo_3* cannot bind two CO molecules at the same time, binding of NO to heme *a_3* allows the subsequent binding of CO to Cu_B. The ν(C-O)Cu_B band in the [*o_3*-NO • OC-Cu_B] complex is symmetric and centered at 2057 cm^{-1}, which contrasts the multiple conformers observed in the light-induced [*o_3* • OC-Cu_B] state (Figure 4.11). Changing the order of gas exposure by forming the heme-nitrosyl complexes before the addition of excess CO had no effect on the FTIR data obtained with *bo_3* and *ba_3* (data not shown).

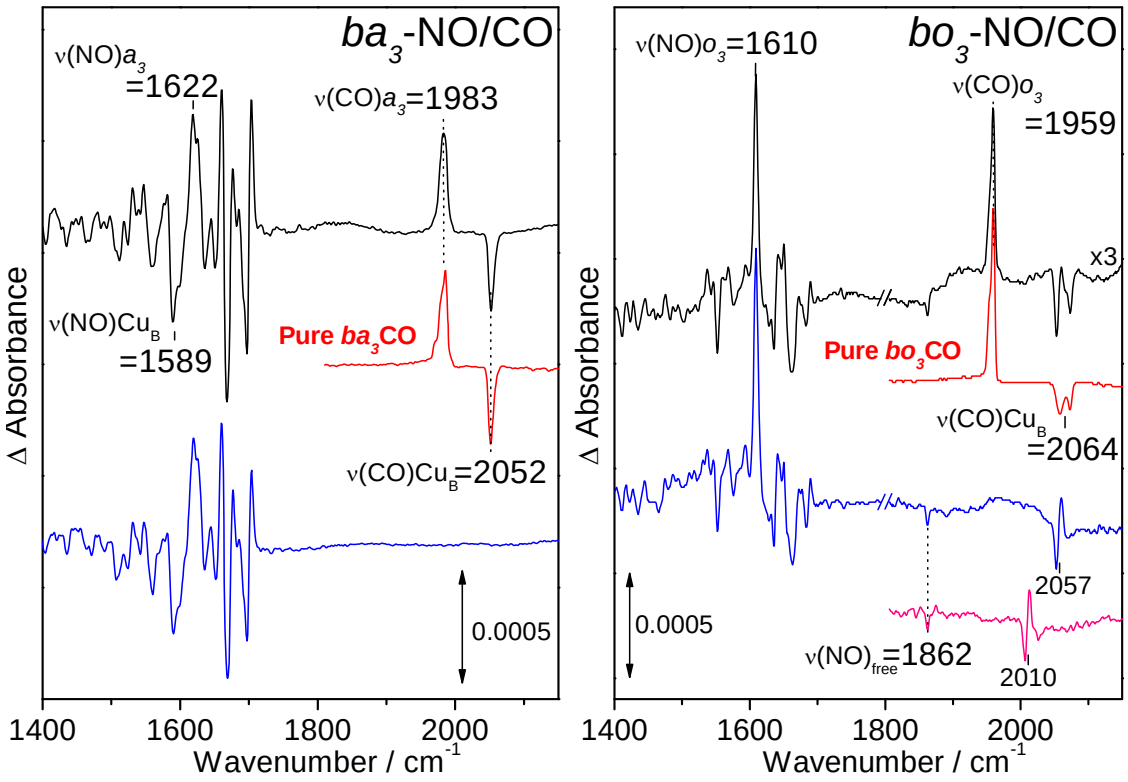

Figure 4.9 FTIR 'dark' minus 'illuminated' difference spectra of *ba*$_3$(CO)(NO) (left) and *bo*$_3$(CO)(NO) (right), before (black) and after annealing at 120 K (blue). Also shown for comparison, are the 'dark' minus 'illuminated' difference spectra for the pure-CO complexes (red traces) and the *bo*$_3$(^{13}CO)(NO) difference spectra after illumination and annealing at 120 K (pink). The spectra were obtained with protein concentration near 350 μM and were normalized based on the room temperature UV-vis spectra obtained directly from the FTIR cell.

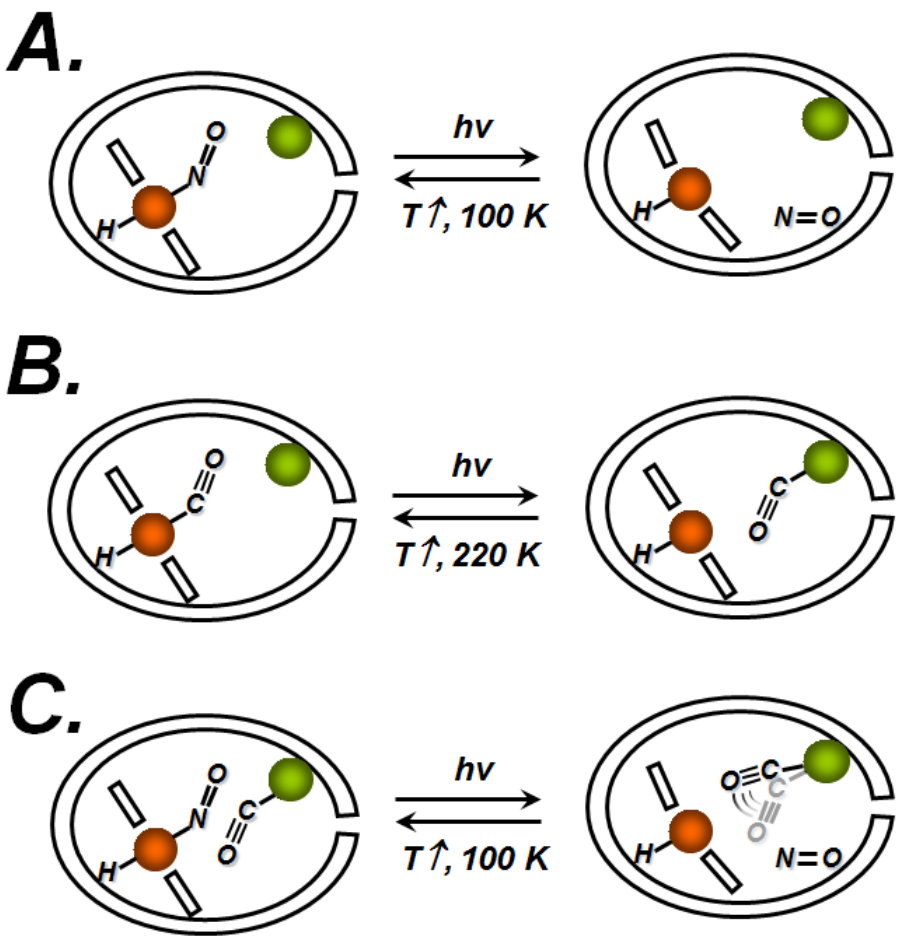

Figure 4.10 Three species *bo*$_3$(NO) (A), *bo*$_3$(CO) (B), and *bo*$_3$(CO)(NO) (C) observed in the *bo*$_3$(CO)(NO) preparation and their photo-induced states based on the low temperature photolysis data.

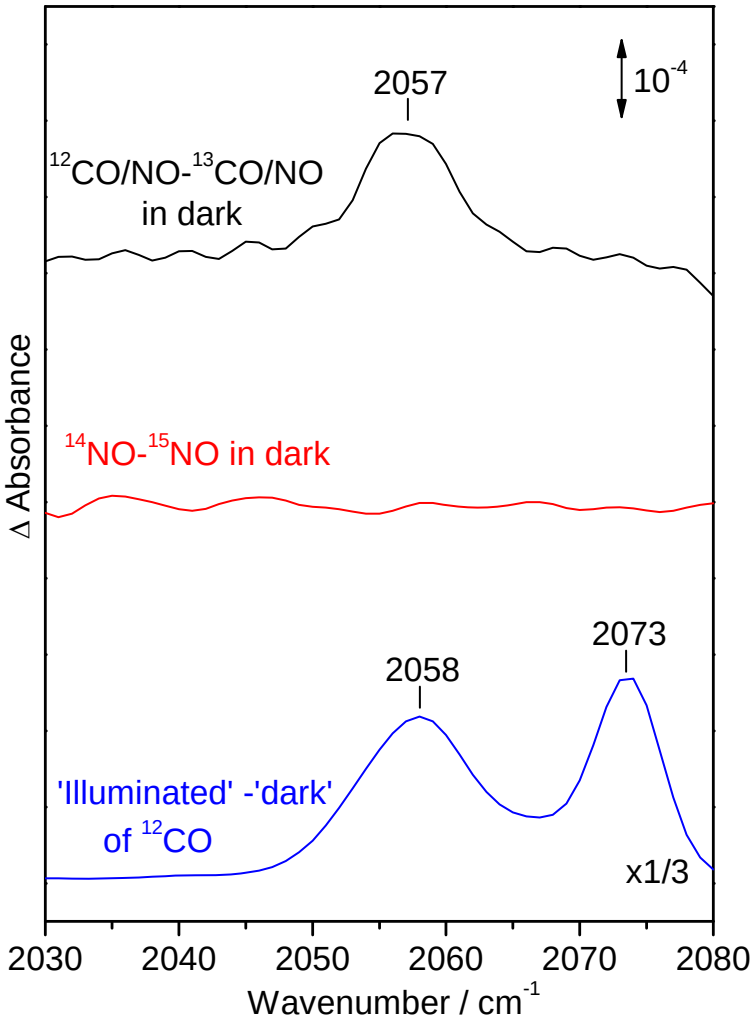

Figure 4.11 Comparison of FTIR difference spectra in the range of the $\nu(^{12}C\text{-}O)Cu_B$ modes in *bo*$_3$. From top to bottom: *bo*$_3$(CO)(NO) minus *bo*$_3$(^{13}CO)(NO) difference spectrum from the 'dark' spectra (black), *bo*$_3$(NO) minus *bo*$_3$(^{15}NO) difference spectrum from the 'dark' spectra (red), and 'illuminated' minus 'dark' *bo*$_3$-^{12}CO (blue). The spectra were obtained with protein concentration near 350 μM and were normalized based on the room temperature UV-vis spectra obtained directly from the FTIR cell.

4.6 Discussion

Several terminal oxidases, including *T. thermophilus* ba_3 and *E. coli* bo_3, have been shown to catalyze the two electron reduction of NO to N_2O (Giuffre *et al.*, 1999; Butler *et al.*, 2002). In the present work, we show that the bo_3 ubiquinol oxidase from *E. coli* reduces NO at a rate equivalent to that of ba_3 (~3 mol NO / [E] mol-min at [NO] = 40 μM). In analogy to ba_3, fully-reduced bo_3 rapidly binds NO to form a stable 6-coordinate low-spin heme-o_3 nitrosyl complex. This nitrosyl complex exhibits Fe-N-O bending modes suggestive of a bent Fe-N-O geometry (Coyle *et al.*, 2003; Lehnert *et al.*, 2010). Illumination of bo_3(NO) at 30 K dissociates the heme-nitrosyl complex with equivalent efficiency as in ba_3(NO), but complete rebinding of NO to the heme o_3 occurs after annealing the sample to 60 K which is significantly lower than the 90-K annealing temperature measured in ba_3(NO). Thus, the photolyzed bo_3(NO) state is thermodynamically less favored than the corresponding nitrosyl complex in ba_3. Comparison of low-temperature FTIR photolysis data for bo_3(NO) and ba_3(NO) support this conclusion. Indeed, light-induced FTIR difference spectra show that stabilization of the photolyzed NO through interactions with Cu_B^I does not occur in bo_3(NO) as it does in ba_3(NO). Rather, the photolyzed FTIR spectrum of bo_3(NO) reveals a ν(N-O) band at 1863 cm^{-1} which corresponds to an NO molecule docked in a proteinaceous pocket (Miller *et al.*, 1997).

What prevents the formation of a light-induced Cu_B-nitrosyl in bo_3? Because the photolysis process with the bo_3(CO) complex leads to the efficient capture of the photolyzed CO by Cu_B, a lack of an open coordination site on Cu_B can be ruled out. Extensive RR and FTIR studies of the heme-copper carbonyl complexes have revealed different configurations, which have been named α, β, and γ forms that correspond to increasing levels of steric restrictions at the active site pocket (Alben *et al.*, 1981; Einarsdottir *et al.*, 1989; Wang *et al.*, 1995; Puustinen *et al.*, 1997). According to these studies, the ba_3(CO) complex represents a highly-restricted site (γ form) (Einarsdottir *et al.*, 1989), while the bo_3(CO) complex offers more open configurations of the dinuclear site (Puustinen *et al.*, 1997). The iron-copper distances reported for the crystal structures of terminal oxidases support this view, with metal-metal distance ranging for 5.3 Å in bo_3 and 4.4 Å in ba_3 (Iwata *et al.*, 1995; Tsukihara *et al.*, 1996; Yoshikawa *et al.*, 1998;

Abramson *et al.*, 2000; Soulimane *et al.*, 2000; Hunsicker-Wang *et al.*, 2005). However, metal-metal distance comparison from crystal structures should be used with caution specially since some the structure of *bo*$_3$ was only solved at 3.5 Å resolution, and because the redox state of the active sites during the X-ray diffraction data acquisition is not always clearly defined.

Based on our FTIR results, we hypothesize that in *bo*$_3$(NO), a larger metal-metal distance prevents the efficient capture of the photolyzed NO by Cu_B. This hypothesis also explains the formation of a *bo*$_3$-(NO)(CO) complex which is not observed in *ba*$_3$. This [*o*$_3$-NO • OC-Cu_B] state is evidenced by a differential signal centered at 2057 cm^{-1} from a Cu_B-carbonyl complex perturbed by the photolysis of NO from heme-*o*$_3$. It is striking that one CO and one NO can co-exist at the dinuclear site of *bo*$_3$, while two CO molecules cannot. This observation suggests that the distance between heme *o*$_3$ and Cu_B is just large enough to accommodate one CO at the Cu_B with one NO at the heme *o*$_3$ in a bent geometry but not large enough to accommodate two linear diatomics. The limited accumulation of [*o*$_3$-NO • OC-Cu_B]) to 20% of the active sites may reflect the presence of multiple conformations of the heme-copper site (in *bo*$_3$). The ν(N-O)*o*$_3$ frequency in the [*o*$_3$-NO • OC-Cu_B] state is equivalent to that observed in the [*o*$_3$-NO • Cu_B] state. However, the [Fe-NO • OC-Cu_B] state exhibits only one ν(C-O)Cu_B at 2057 cm^{-1}, which contrasts with the multiple ν(C-O)Cu_B bands observed at 2056 and 2073 cm^{-1} observed after photolysis of *bo*$_3$(CO) at low temperature (Figure 4.10) (Hill *et al.*, 1992). EXAFS measurements suggest that high ν(C-O)Cu_B frequencies could correspond to active site populations where one of the three coordinating histidines to Cu_B is weakly bound (Calhoun *et al.*, 1993). Regardless of the structural significance of the different ν(C-O)Cu_B frequencies, the mixed-gas experiments suggest that the conformer that correspond to the high ν(C-O)Cu_B does not bind CO in presence of the heme *o*$_3$-NO complex.

Reports of concomitant binding of two diatomic molecules at heme-copper dinuclear sites are scarce. In fully-reduced bovine and prokaryotic *aa*$_3$, the loss of the EPR signal from *a*$_3$-NO at high NO concentration has been assigned to the binding of a second NO molecule to Cu_B (Brudvig *et al.*, 1980; Pilet *et al.*, 2007). Using FTIR spectroscopy, Caughey and coworkers observed two ν(NO)s in bovine *aa*$_3$: one at 1610

cm^{-1} assigned to a_3-NO, and one at 1700 cm^{-1} assigned to Cu_B-NO (Zhao *et al.*, 1994). Presumably, the lack of NO reductase activity in aa_3 terminal oxidases permits the accumulation of a stable [$\{FeNO\}^7/\{CuNO\}^{11}$] complex, but the presence of two NO molecules in the active site of ba_3 and bo_3 is expected to represent a highly reactive intermediate within the NO reductase turnover. Although the characterization of a [o_3-NO • OC-Cu_B] complex in bo_3 suggests that this active site can also accommodate a [$\{FeNO\}^7/\{CuNO\}^{11}$] trans-complex, this state may also correspond to a dead-end adduct as in the aa_3 systems.

Low-temperature photolysis experiments are a sensitive probe of dinuclear heme-copper active site. The results presented here show that fully-reduced ba_3 and bo_3 bind a first NO molecule to the high-spin heme-iron(II) in similar fashion, but the heme iron-copper distance differs significantly in the two proteins. Thus, in ba_3, the close vicinity of the heme a_3 and the Cu_B allows for the transfer of the photolyzed NO from the heme to Cu_B in a side-on geometry as shown in Chapter 3, whereas in bo_3, the larger metal-metal distance does not restrict the coordination of a second diatomic molecule at the Cu_B site. Our experiments do not determine whether the Cu_B^I site in bo_3(NO) binds a second NO molecule to form a trans [$\{FeNO\}^7/\{CuNO\}^{11}$] complex. Nevertheless, the comparison of ba_3 and bo_3 shows that the mechanism of NO reduction can accommodate the difference in heme-copper distances in these two active sites. This conclusion argues against the coordination of the second NO molecule to Cu_B^I as an essential step in the reaction mechanism. Instead, the role of the Cu_B site may be limited to promote the formation of a heme iron-hyponitrite species through electrostatic interactions (Blomberg *et al.*, 2006; Moënne-Loccoz, 2007).

CHAPTER 5
CHARACTERIZATION OF HEME AND NON-HEME Fe-NO COMPLEXES IN Fe_BMb

5.1 Structural and functional model of NORs

In chapter 3 and 4, we reported low-temperature FTIR photolysis experiments on cytochrome *ba₃*(NO) and *bo₃*(NO) complexes, and showed that, although *ba₃* and *bo₃* exhibit similar NO reductase activities (e.g. ~3 mol NO/[enzyme] • min), a side-on Cu_B-NO complex was observed only in *ba₃*. Furthermore, only *bo₃*(NO) can concomitantly bind CO to form a [*o₃*-NO • OC-Cu_B] ternary complex. We assigned these differences to differences in iron-copper distance in the two proteins and proposed that coordination of the second NO to Cu_B is not a productive step in the NO-reduction mechanisms of these enzymes (Hayashi *et al.*, 2007; Hayashi *et al.*, 2009). However, because the active site metal composition in NORs is different than in HCOs, this conclusion does not directly apply to NORs.

Recently, Yeung et al. reported a protein model that mimics the active site of NORs by introducing three histidine and one glutamate residues, as ligand sets to engineer a non-heme iron Fe_B center in the distal pocket of sperm whale myoglobin (Yeung *et al.*, 2009). The crystal structure of the triple mutant (L29H, F43H, and V68E), named Fe_BMb, shows that the non-heme iron in the Fe_B site is coordinated by the three histidine, one glutamate, and one water molecule in an octahedral coordination geometry (Figure 5.1). The iron-iron distance of Fe_BMb is 4.8 Å and is similar to the iron-copper distances reported for terminal oxidases (~5 Å). Although these NOR modes exhibit low NO reductase activities, study of the interaction of NO with this NOR active site model would expand our knowledge of NO chemistry that occurs in heme/non-heme dinuclear iron center of NORs.

Here, we report the UV-vis, RR, and FTIR characterization of the Fe-NO complexes formed in Fe_BMb. Addition of 1 equiv NO to reduced Fe^{II}-Fe_BMb results in the formation of a stable 6cLS heme-nitrosyl $\{FeNO\}^7$ complex with an exceptionally low ν(NO) stretching frequencies. This complex reacts further with NO to form a new

species, previously assigned to oxidized protein (Yeung *et al.*, 2009). However, our spectroscopic data suggests that the product of this reaction is not the oxidized protein and N_2O but instead a stable [heme-NO • ON-Fe] diferrous-dinitrosyl complex. These $\{FeNO\}^7$ complexes are discussed within the context of proposed NO reduction mechanisms in the heme/non-heme center of NORs.

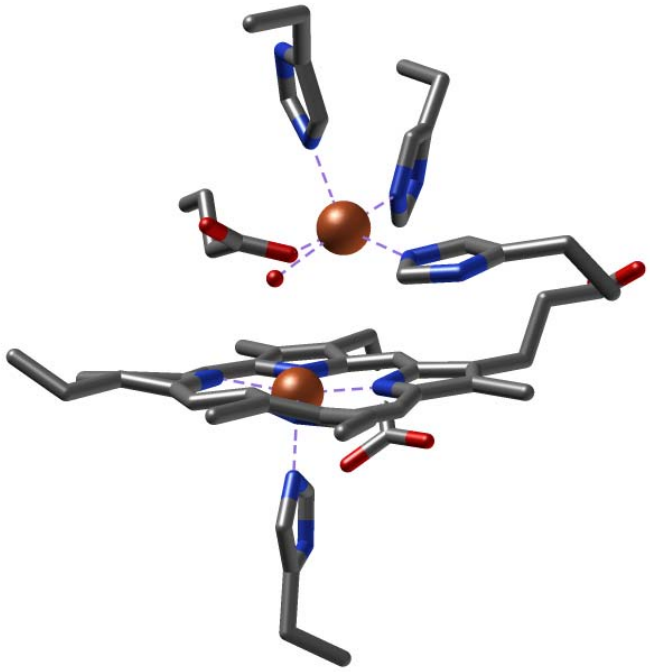

Figure 5.1 The heme/non-heme diiron center of Fe_BMb. (PDB ID code: 3M39)

5.2 Materials and methods

Protein preparations and Metal titrations

The expression and purification of Fe_BMb (swMb L29H/F43H/V68E) was performed as previously described (Yeung *et al.*, 2009). All the protein concentrations were calculated based on an ε_{406} extinction coefficient of 175 $mM^{-1}cm^{-1}$ in the oxidized state. Approximately 1 mM Fe_BMb solutions were brought into a glove box containing less than 1ppm of O_2 (Omnilab System, Vacuum Atomsphares Company) and

concentrated by a microcon filtering device (10 kDa cutoff, Amicon ultra, Millipore) if necessary. The protein solution was reduced by addition of ~5 mM dithionite followed by removal of excess reduction agents with desalting spin columns (Zebra, Pierce). Fe^{II} and Zn^{II} titrations were performed in 50 mM Bis-Tris pH 7.0 using $Fe^{II}Cl_2$ and $Zn^{II}SO_4$, respectively. Fresh Fe^{II} and Zn^{II} solutions were prepared each time by dissolving $Fe^{II}Cl_2$ and $Zn^{II}SO_4$ in 0.01 M HCl. Typically, 3 µl of metal solution containing 1.3~2 equiv of metals was added to 80~100 µl of ~1 mM protein solutions at 60 µl/h with gentle stirring. After metal addition, the protein solution was incubated at room temperature for 20 min with gentle stirring. The metal binding to the protein was confirmed by UV-vis spectroscopy. 1 equiv and excess NO adducts of Fe^{II}- and Zn^{II}-Fe_BMb were prepared as described in Chapter 2.2.

Molecular spectroscopy

UV-vis, RR, and FTIR measurements were performed as described in Chapter 2.2. The typical enzyme concentrations for RR, EPR and FTIR were 80~100 µM, 100 µM and 0.5~1.2 mM, respectively.

For EPR spectroscopy, 250 µL of *bo*$_3$(NO) complex prepared in an EPR tube was flash-frozen in liquid N_2 after confirming the presence of the NO adducts by UV-vis absorption spectroscopy. Quantitation of the EPR signals was performed under non-saturating conditions by double integration and comparison with Cu^{II}EDTA standards.

The FTIR cell was mounted to a sample rod prior to flash-freezing in liquid N_2 and insertion into the sample compartment of a pre-cool closed-cycle cryogenic system (Omniplex). The sample was kept in the dark while the temperature dropped to 10 K. The FTIR spectra were obtained on a Bruker Tensor 27 equipped with a liquid-N_2 cooled MCT detector and purged with compressed air dried and depleted of CO_2. Sets of 1000-scan accumulations were acquired at a 4-cm^{-1} resolution. These data averaging conditions required 7-min. Photolysis of the NO adducts was achieved with continuous illumination of the samples directly in the FTIR sample chamber with a 300 W arc lamp after filtering out heat and NIR emission. The same illumination procedure was used to follow the dissociation-rebinding process by UV-vis spectroscopy with the Cary-50 spectrophotometer.

RR samples were prepared in anaerobic Raman capillaries. The RR spectra were collected in a 90^{o} scattering geometry on samples mounted on a reciprocating translation stage at room temperature. Kaiser Optical supernotch filters were used to attenuate Rayleigh scattering generated by the 413-nm excitation. Frequencies were calibrated relative to indene and CCl_4 standards and are accurate to ±1 cm^{-1}. The integrity of the RR samples is confirmed by direct monitoring of their UV-vis absorption spectra in Raman capillaries before and after laser exposure.

5.3 Formation of heme-NO complex in Fe_BMb

Upon addition of Fe^{II} or Zn^{II}, the UV-vis spectra of deoxy Fe_BMb exhibits small changes; the Soret band at 434 nm blue-shifts to 433 nm and the α/β band at 556 nm splits into two bands at 556 and 577 nm, suggesting metal binding to the apoprotein (Figure 5.2) (Yeung *et al.*, 2009). Addition of up to 1 equiv of NO to reduced Fe^{II}-Fe_BMb results in a blue-shift of the Soret to 420 nm and appearance of α/β bands at 546 and 582 nm in the UV-vis spectrum (Figure 5.3 A). These absorption features are characteristics of 6cLS heme-NO complexes and very similar to those of the NO complex formed in apo-Fe_BMb (Figure 5.3A). The near complete conversion of Fe_BMb upon stoichiometric addition of NO suggests that the ferrous heme has a higher NO affinity than the non-heme Fe_B center.

The reaction of Zn^{II}- Fe_BMb with 1 equiv of NO generates a mixture of species as indicated by the presence of pronounced shoulders on both high- and low-wavelength sides of the heme Soret band (Figure 5.3 B). The Soret band at 421 nm is characteristics of 6cLS heme-NO, and the shoulders on high- and low-wavelength sides suggest incomplete reaction of the proteins with NO and the presence of 5cLS heme-NO species, respectively (Coletta *et al.*, 1990; Decatur *et al.*, 1996). A deconvolution analysis of the Soret absorption envelope yields estimates for the 1 equiv NO adducts composition of 40% 6cLS heme-NO, 30% 5cLS heme-NO, and 30% reduced (data not shown). So far, addition characterization of Zn^{II}-Fe_BMb(NO) is hampered by this mixture of species.

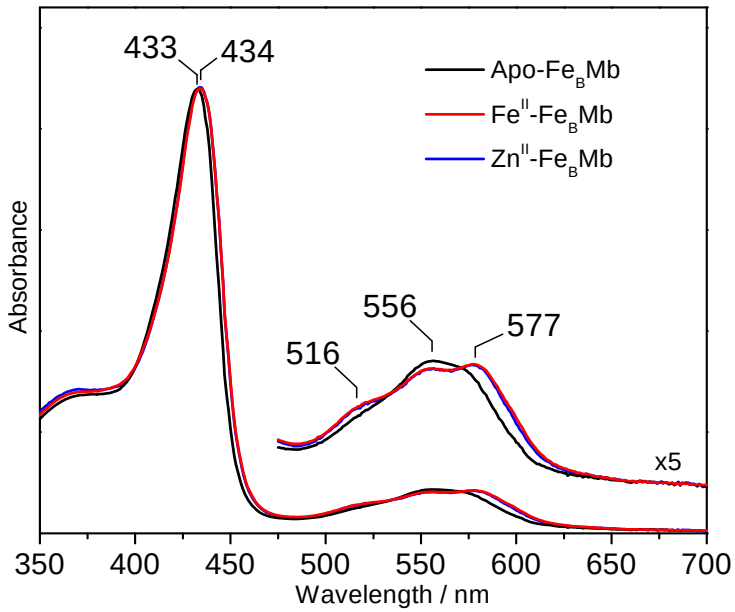

Figure 5.2 UV-vis absorption spectra of deoxy apo-, Fe^{II}-, and Zn^{II}-Fe_BMb.

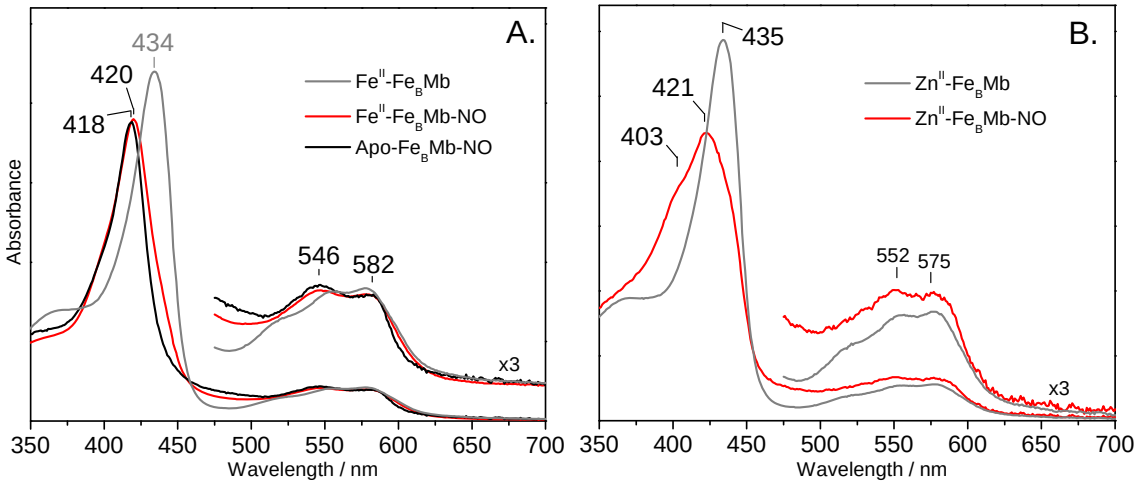

Figure 5.3 UV-vis absorption spectra of deoxy and 1 equiv NO adduct Fe^{II}-Fe_BMb and NO adduct apo-Fe_BMb, obtained at room temperature (A). The presence of a small shoulder on high-wavelength side of the Soret suggests incomplete reaction of the protein with NO. Indeed, subtraction of the high-wavelength component from the UV-vis spectrum of Fe^{II}-Fe_BMb using the spectrum of Fe^{II}-Fe_BMb produces a spectrum identical to that of apo-Fe_BMb(NO). UV-vis absorption spectra of deoxy and 1 equiv NO adduct Zn^{II}-Fe_BMb obtained at room temperature (B).

At 10 K, the UV-vis spectra of apo-$Fe_BMb(NO)$ and Fe^{II}-$Fe_BMb(NO)$ exhibit Soret bands at 423 and 426 nm, respectively, and are consistent with 6cLS heme-NO complexes (Figure 5.4). After a few minutes of illumination with 300-W arc lamp, however, new species associated with Soret band at ~440 nm appear at the expense of the Soret bands at ~425 nm, with 'dark' minus 'illuminated' difference spectra suggestive of efficient photo-dissociation of the nitrosyl complex in apo- and Fe^{II}-Fe_BMb.

As previously reported, the EPR spectrum of apo-$Fe_BMb(NO)$ is characteristic of an $S = 1/2$ 6cLS heme-NO species with g value centered around 2 (2.094, 2.012, 1.970) and a clear 9-line ^{14}N-hyperfine structure (A_{NO} = 21.5 G, A_{His} = 6 G) (Figure 5.5) (Lin *et al.*, 2010). Conversely, the EPR spectrum of Fe^{II}-$Fe_BMb(NO)$ complex shows a weak signal centered at $g \sim 2$ with 3-line ^{14}N-hyperfine structure (A_{NO} = 16.5 G), typically assigned to 5cLS heme iron^{II}-NO species. EPR signal quantification using $Cu^{II}EDTA$ standards suggests that this $g \sim 2$ signal represents only 6% of entire heme/non-heme diiron site. Thus, majority of the heme-nitrosyl species in Fe^{II}-$Fe_BMb(NO)$ are EPR silent at liquid nitrogen temperature (Figure 5.5).

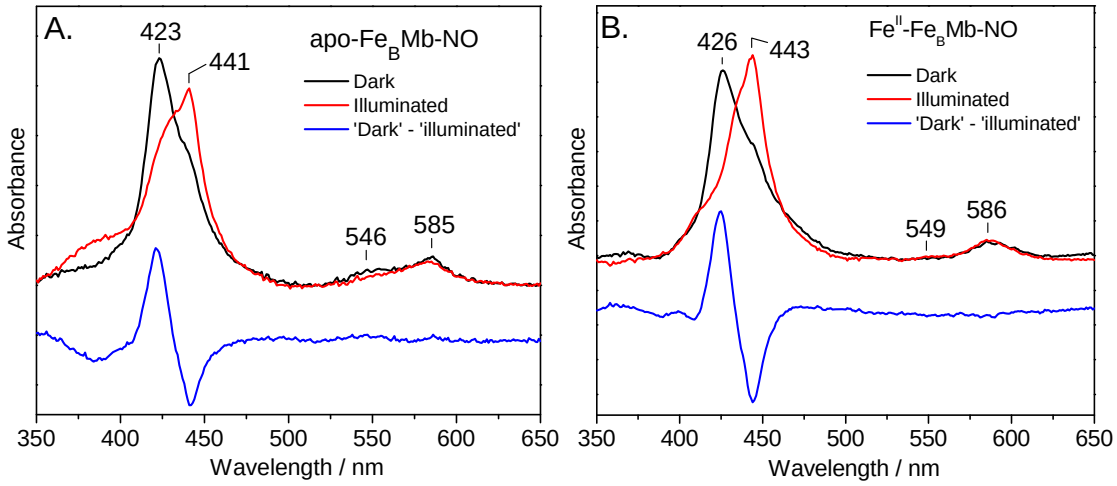

Figure 5.4 UV-vis spectra of apo-$Fe_BMb(NO)$ (A) and Fe^{II}-$Fe_BMb(NO)$ (B) obtained at 10K before (black) and after illumination (red). Also shown are 'dark' minus 'illuminated' difference spectra (blue).

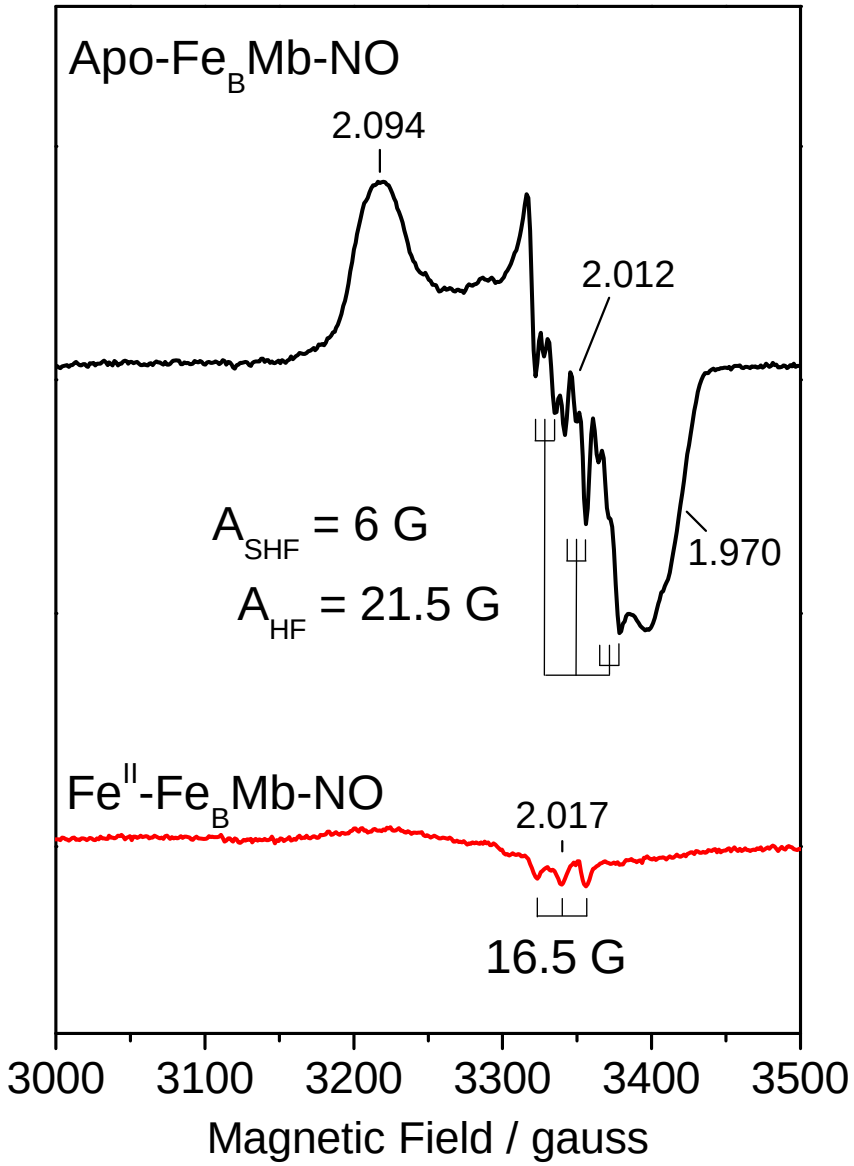

Figure 5.5 EPR spectra of Apo- and Fe^{II}-Fe_BMb(NO), obtained at 110 K. Condition: protein concentration, 100 μM; microwave frequency, 9.43 GHz; microwave power, 4 mW; modulation frequency, 100 kHz; modulation amplitude, 2.0 G.

The apo-Fe_BMb(NO) complex resulting from the reaction of reduced apo-Fe_BMb with excess NO are sufficiently stable to allow extended acquisition time for optimal RR spectral characterization. The high-frequency RR spectra of apo-Fe_BMb(NO) obtained with 413-nm excitation, show porphyrin skeletal modes ν_4, ν_3, ν_2, and ν_{10} at 1375, 1503, 1583, and 1638 cm^{-1}, consistent with 6cLS heme-NO complexes (Figure 5.6) (Tsubaki and Yu, 1982; Benko and Yu, 1983). The 'NO' minus '^{15}NO' RR difference spectrum reveals an isotope sensitive band at 1606 cm^{-1} which downshifts to 1582 (-24) cm^{-1}, readily assigned to ν(NO) of the heme-NO complex. The low-frequency RR spectra exhibit isotope sensitive mode at 560 cm^{-1} which downshifts to 538 (-22) cm^{-1}, assigned to δ(Fe-NO) of the heme-nitrosyl complexes and similar to that of wild-type sperm whale myoglobin (Tsubaki and Yu, 1982).

The mononitrosyl Fe^{II}-Fe_BMb(NO) complex forms only when using ≤1 equiv of NO. As expected from the UV-vis data, incomplete reaction of the protein with NO was also observed in RR samples (data not shown). In addition, the Fe^{II}-Fe_BMb(NO) complex exhibits a highly photolabile character at room temperature. Even with minimal laser power (~0.05 mW) and continuous sample translation, the accumulation of the NO dissociated state (i.e., reduced-like species) was observed in RR capillaries. The high-frequency RR spectra of Fe^{II}-Fe_BMb(NO), obtained with 413-nm excitation, show two prominent oxidation-state marker bands ν_4 at 1353 and 1375 cm^{-1} (Figure 5.6). The species with ν_4 at 1353 cm^{-1} increases at higher laser power and was also observed for reduced Fe^{II}-Fe_BMb, consistent with NO dissociated state of Fe^{II}-Fe_BMb(NO) complex; a RR difference spectrum was computed to isolate the component of the nitrosyl complex from the raw data (Figure 5.6). The RR difference spectrum of Fe^{II}-Fe_BMb(NO) exhibits porphyrin skeletal modes ν_4, ν_3, ν_2, and ν_{10} at 1374, 1503, 1583, and 1638 cm^{-1}, characteristic of 6cLS heme-nitrosyl species (Figure 5.6). Although ν(NO) could not be extracted from the RR spectra, its low-frequency spectra reveal an isotope sensitive mode at 577 cm^{-1}, assigned to δ(Fe-NO) of the heme-nitrosyl complex (Figure 5.6). This δ(Fe-NO) mode is up-shifted ~17 cm^{-1} compared to the corresponding vibration in apo-Fe_BMb(NO).

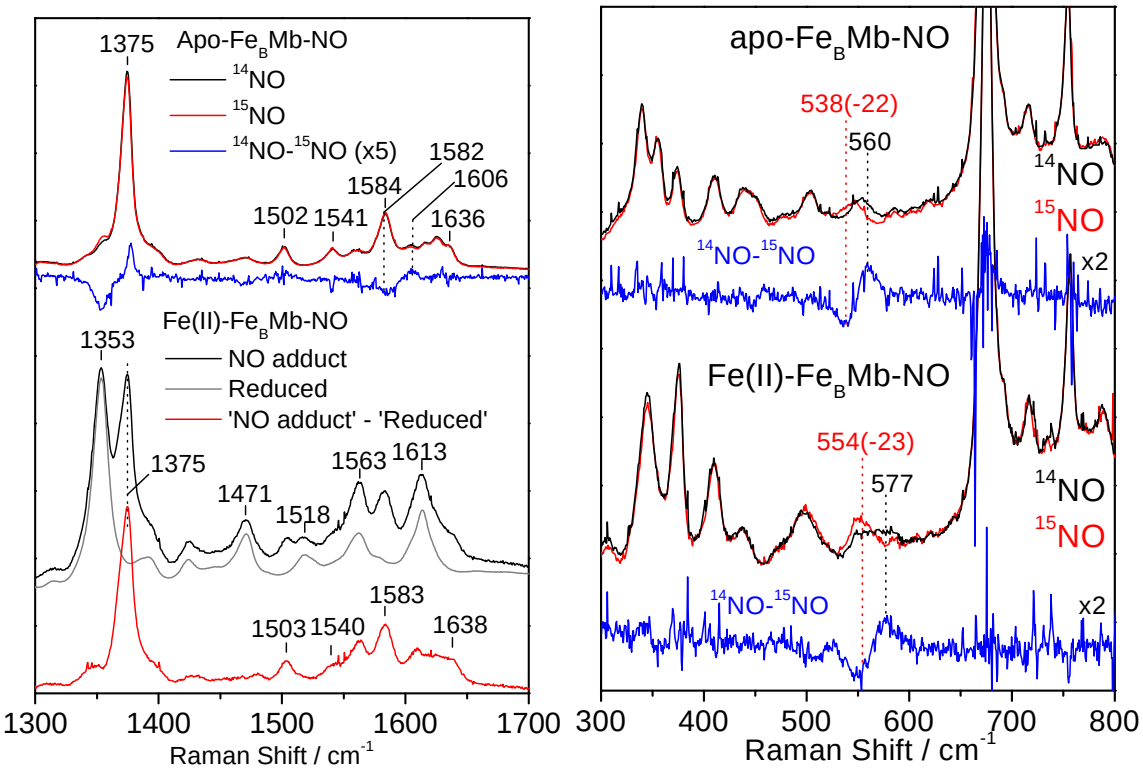

Figure 5.6 High-frequency RR spectra of Fe^{II}-Fe_BMb(NO), Fe^{II}-Fe_BMb, and apo-Fe_BMb(NO), and RR 'NO adduct' minus 'reduced' difference spectrum of Fe^{II}-Fe_BMb(NO), obtained with 413-nm excitation at room temperature (left). Low-frequency RR spectra of Fe^{II}- and apo-Fe_BMb(NO), obtained with 413-nm excitation at room temperature (right). Also shown are 'NO' minus '^{15}NO' difference spectra.

In the 10 K 'dark' minus 'illuminated' FTIR difference spectra of apo-Fe_BMb(NO), a positive band at 1601 cm^{-1} which downshifts to 1570 with ^{15}NO is assigned to ν(NO) of the heme-NO complex. The frequency is a close match to that observed in the RR spectra. The difference spectra also reveal a negative band at 1856 cm^{-1} which downshifts to 1823 cm^{-1} with ^{15}NO, readily assigned to ν(NO) of free NO docked in a proteinaceous pocket as observed with the nitrosyl complexes of myoglobin and some HCOs (Miller *et al.*, 1997; Hayashi *et al.*, 2009). Although Fe^{II} binding at the Fe_B site does not significantly affect the electronic absorption spectrum of the Fe_BMb(NO) complex (Figure 5.3 A), it leads to a large downshift of the ν(NO)heme mode. Specifically, the 10 K 'dark' minus 'illuminated' FTIR difference spectrum of Fe^{II}-Fe_BMb(NO) complex shows a positive band at 1549 cm^{-1}, which shifts to 1525 and 1480 cm^{-1} with ^{15}NO and $^{15}N^{18}O$, respectively (Figure 5.7). Reproducible detection of a negative band which could be assigned to free NO docked in a proteinaceous pocket was not achieved and may reflect the presence of multiple docking sites in Fe^{II}-Fe_BMb compared to apo-Fe_BMb.

The ν(NO) vibrations are accompanied by weaker signals between 1200 to 1700 cm^{-1} that cancel out in the isotope-edited difference spectra and are thus assigned to perturbations of amide and porphyrin vibrational modes. In addition, the difference spectra of apo-Fe_BMb(NO) complex show a differential signal centered at 1742 cm^{-1}, readily assigned to ν(C=O) of a carboxylic acid, which disappears upon Fe^{II} binding, suggesting that the carboxylic acid is deprotonated and presumably coordinated to the Fe_B metal center (Baenziger *et al.*, 1993; Yeung *et al.*, 2009; Lin *et al.*, 2010), while in apo-Fe_BMb(NO) the side chain of Glu68 must be protonated and impacted by the photolysis process. It is worth pointing out that the annealing temperature for the photolysis process in apo-Fe_BMb(NO) is 60 K but 120 K in Fe^{II}-Fe_BMb(NO), suggesting a greater thermodynamic barrier for NO-rebinding in the latter complex.

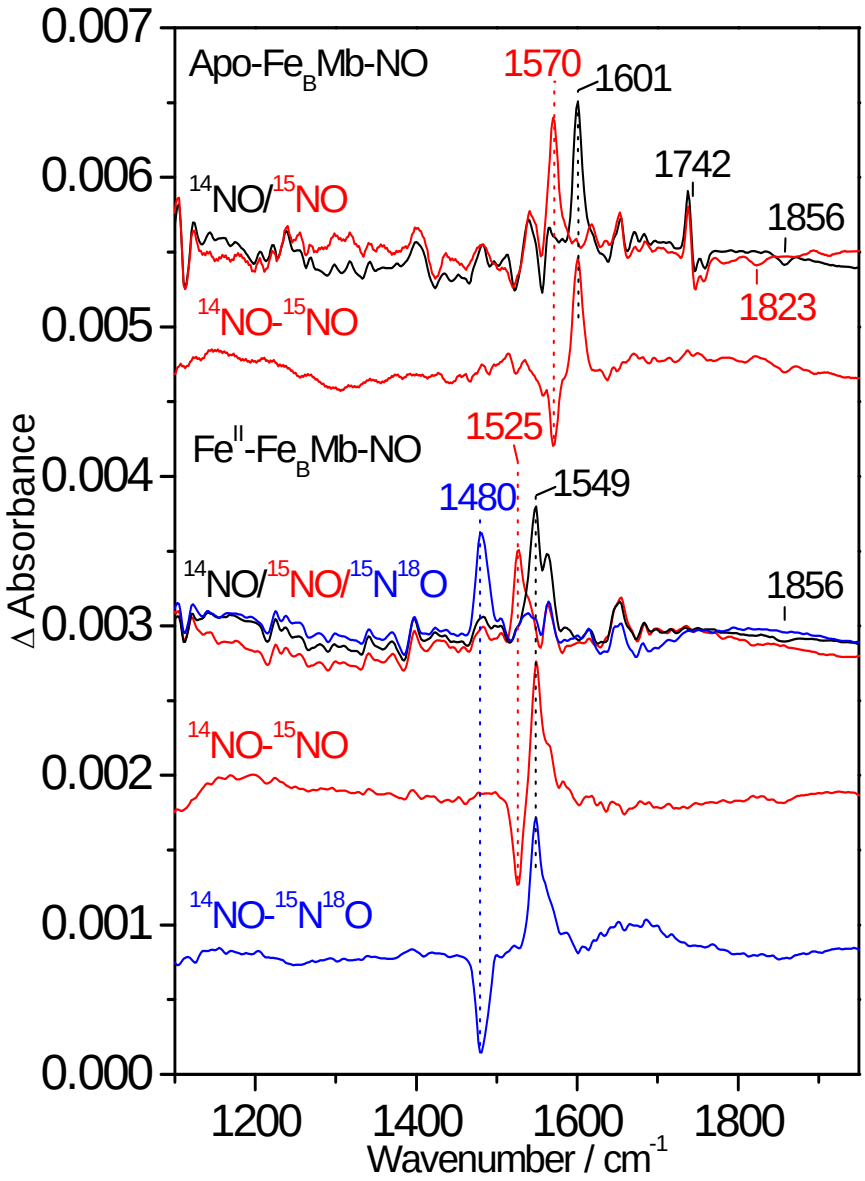

Figure 5.7 FTIR 'dark' minus 'illuminated' difference spectra of apo-Fe$_B$Mb(NO) (top) and Fe^{II}-Fe$_B$Mb(NO) (bottom) with NO (black), ^{15}NO (red), and ^{15}N^{18}O (blue), obtained at 10 K. Also shown are 'NO' minus '^{15}NO' (red) and 'NO' minus '^{15}N^{18}O' (blue) difference spectra.

5.4 Formation of [heme-NO • ON-Fe_B] trans-dinitrosyl complex in Fe_BMb

Further addition of NO to Fe^{II}-Fe_BMb(NO) results in a blue-shift of the Soret absorption from 420 to 406 nm and the appearance of a new absorption band at ~470 nm (Figure 5.8). The same complex was prepared by addition of 1 atm NO gas to the headspace of reduced Fe^{II}-Fe_BMb (Figure 5.8). The product of this reaction is stable as no additional changes occur in the UV-vis spectrum in the course of several hours. To determine whether the reaction of NO with Fe^{II}-Fe_BMb(NO) produces N_2O, we attempted to detect the asymmetric N-N-O stretch mode ν_3 of N_2O at 2231 cm^{-1} in the room temperature FTIR spectra from a Fe^{II}-Fe_BMb sample incubated with 2 mM NO produced from NONOate, but observed no significant N_2O production, even after 960 min (Figure 5.9). From comparison with standard samples, the intensity of the FTIR band at 2330 cm^{-1} reveals that less than 0.2 equiv of N_2O is produced per Fe^{II}-Fe_BMb protein. Another observation inconsistent with the occurrence of a NO reduction cycle at the diiron site is the detection of an intense IR band at 1760 cm^{-1} which is a good candidate for a ν(NO) from a non-heme $\{FeNO\}^7$ formed at the Fe_B site (vide infra).

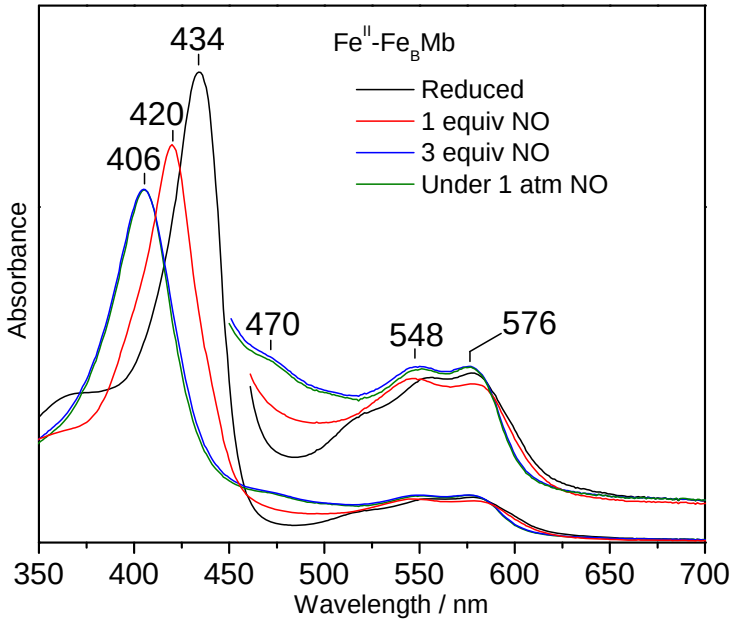

Figure 5.8 UV-vis absorption spectra of deoxy, 1 equiv, 3 equiv, and 1 atm NO adducts of Fe^{II}-Fe_BMb obtained at room temperature.

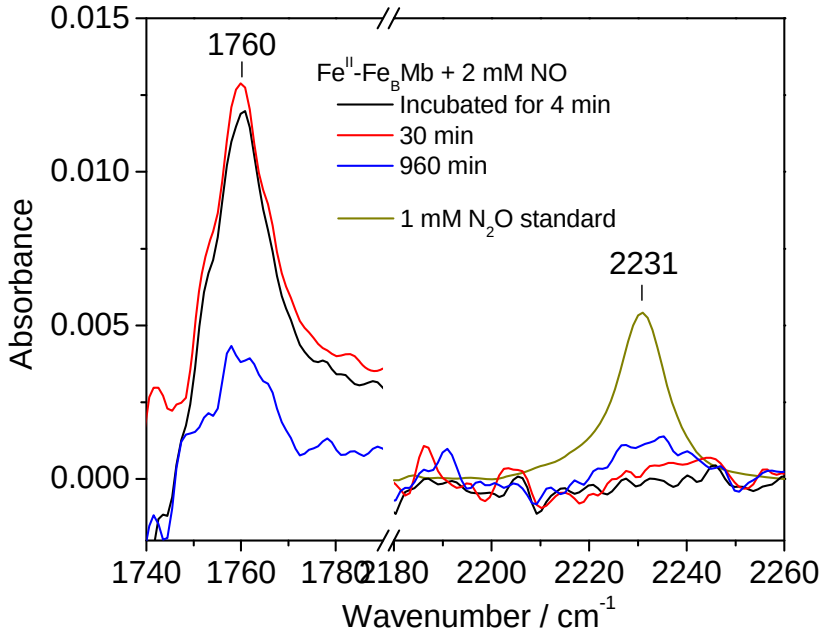

Figure 5.9 FTIR detection of N_2O produced by 0.7 mM Fe^{II}-Fe_BMb after incubation for 4, 30, 180, 960 min with 2 mM NO produced from NONOate. Also shown are average of two FTIR spectra of 1 mM N_2O standards obtained from multi-turnover reactions of reduced cytochrome *bo₃* (50 μM) and *ba₃* (50 μM) in presence of 10 mM ascorbate The IR spectra of Fe^{II}-Fe_BMb were normalized to 1 mM to facilitate the comparison.

The NO complex of Fe^{II}-Fe_BMb formed with excess NO is sufficiently stable to allow extended acquisition time and optimal RR characterization. The high-frequency RR spectra obtained with 413-nm excitation, show porphyrin skeletal modes ν_4, ν_3, ν_2, and ν_{10} at ~1375, ~1505, 1583, and ~1641 cm^{-1} consistent with a 5cLS heme-NO complex (Figure 5.10 A) (Yu *et al.*, 1994; Decatur *et al.*, 1996). These high-frequency RR spectra also reveal isotope sensitive bands at 1666 cm^{-1}, which downshifts to 1633 (-33) and 1596 (-70) cm^{-1} with ^{15}NO and $^{15}N^{18}O$, respectively. These isotope shifts are in perfect agreement with predicted value for isolated diatomic vibrations and consistent with ν(N-O) of a 5cLS heme-NO complex (Deinum *et al.*, 1996; Andrew *et al.*, 2001; Thomas *et al.*, 2001). In addition, the RR spectra reveal another isotope sensitive band at 1758 cm^{-1}, which downshifts to 1726 (-32) and 1685 (-73) cm^{-1} with ^{15}NO and $^{15}N^{18}O$, respectively (Figure 5.10A). The 1758 cm^{-1} frequency matches the intense IR band observed at 1760 cm^{-1} in Fe^{II}-Fe_BMb incubated with 2 mM NO (Figure 5.10 A and 5.9), and is less photolabile than the 5cLS heme-NO complexes at high laser power with static samples (data not shown). This signal is not observed in the RR spectra of wild type Mb incubated with 1 atm NO in the presence of 2 equiv Fe^{II} (Figure 5.10 A), and is assigned to the ν(N-O) of a $\{FeNO\}^7$ formed at the Fe_B site, since this frequency is in good agreement with the ν(NO) of other non-heme $\{Fe\text{-}NO\}^7$ complexes (Table 5.1) (Brown *et al.*, 1995; Feig *et al.*, 1996; Clay *et al.*, 2003; Lu *et al.*, 2004). Thus, excess NO addition to Fe^{II}-Fe_BMb results in the formation of a [heme Fe-NO • ON-Fe_B] *trans*-dinitrosyl complex.

The low-frequency RR spectra of Fe^{II}-Fe_BMb$(NO)_2$ reveal an isotope sensitive band at 515 cm^{-1}, which downshifts to 507 (-8) and 505 (-10) cm^{-1} with ^{15}NO and $^{15}N^{18}O$ respectively, and is assigned to the δ(Fe-NO) of the 5cLS heme-NO complex (Figure 5.10 B and Table 5.1) (Deinum *et al.*, 1996; Andrew *et al.*, 2001; Thomas *et al.*, 2001). Not surprisingly, the detection of low-frequency Fe-N-O vibrations from the $\{Fe_BNO\}^7$ complex is prevented by more intense porphyrin vibrations.

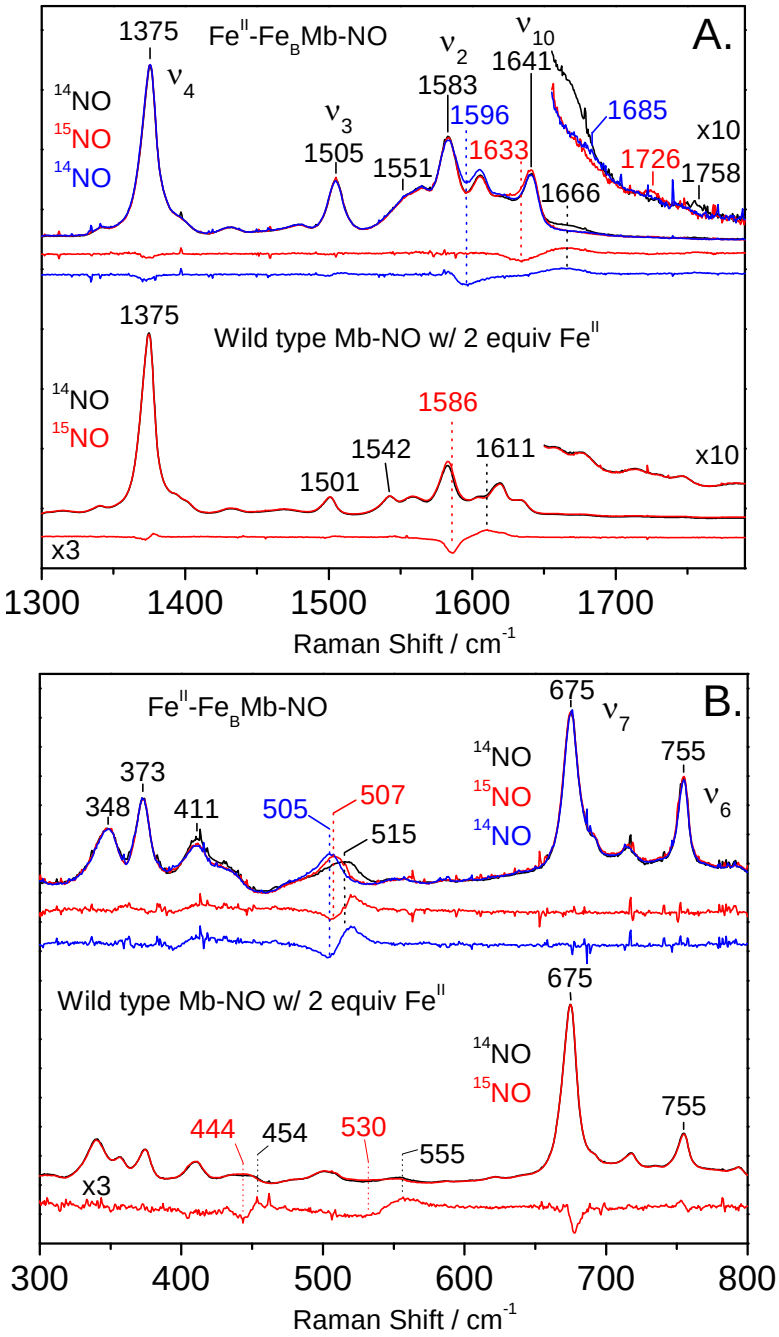

Figure 5.10 High- and Low-frequency RR spectra (A and B) of Fe^{II}-Fe_BMb and wild type Mb plus 2 equiv Fe^{II} NO adducts prepared with 1 atm NO (black), ^{15}NO (red), and $^{15}N^{18}O$ (blue), obtained with a 413-nm excitation at room temperature. Also shown are 'NO' minus '^{15}NO'(red) and 'NO' minus '$^{15}N^{18}O$'(blue) difference spectra.

Table 5.1 Vibrational frequencies of heme and non-heme $\{FeNO\}^7$ species

$\{FeNO\}^7$ species	ν (Fe-N-O) / cm^{-1} ($\Delta^{15}N$) (*$\Delta^{15}N^{18}O$)	ν(N-O) / cm^{-1} ($\Delta^{15}N$) (*$\Delta^{15}N^{18}O$)	References
6-coordinate heme $\{FeNO\}^7$			
Fe^{II}-Fe_BMb(NO)	577 (-25)	1549 (-22) (*-69)	this chapter
apo-Fe_BMb(NO)	560 (-24)	1601 (-29)	this chapter
swMb(NO)	560 (-28) (*-28)	1613 (- 26) (*-68)	(Miller *et al.*, 1997; Tomita *et al.*, 1999)
T.t. ba_3(NO)	539 (-17)	1622 (-32) (*-75)	Chapter 3, (Pinakoulaki *et al.*, 2005)
E.c. bo_3(NO)	534 (*-17) 440 (*-13)	1610 (-30)(*-70)	Chapter 4
5-coordinate heme $\{FeNO\}^7$			
Fe^{II}-Fe_BMb$(NO)_2$	515 (-7) (*-10)	1666 (-33) (*-70)	this chapter
H93G swMb(NO)	535 (-14)	1670 (-32)	(Thomas *et al.*, 2001)
*A. x.*cytochrome *c'*(NO)[a]	526 (-14)	1661 (-30)	(Andrew *et al.*, 2001)
Bovine sGC(NO)	525 (*-16)	1677 (*-70)	(Deinum *et al.*, 1996)
Non-heme $\{FeNO\}^7$			
Fe^{II}-Fe_BMb$(NO)_2$	Not observed	1758 (-32) (*-73)	this chapter
Deflavo-FDP$(NO)_2$	459 (-7)	1749 (-30)	Chapter 6
Wild-type R2$(NO)_2$	445 (-7)	1742 (-29)	(Haskin *et al.*, 1995; Lu *et al.*, 2004)
Fe(EDTA)(NO)	496 (-4)	1776 (-37)	(Orville and Lipscomb, 1993; Brown *et al.*, 1995)
$Fe_2(NO)_2$(EtHPTB) $(O_2CPh)(BF_4)_2$	490 (-5)	1785 (-35)	Hayashi *et al*. unpublished, (Feig *et al.*, 1996)

[a] *Alcaligenes xylosoxidans cytochrome c'*

5.5 Discussion

Stoichiometric addition of NO to fully reduced Fe^{II}-Fe_BMb results in the formation of a stable heme-NO complex. The UV-vis absorption spectra of this complex is very similar to that of apo-Fe_BMb and characteristic of 6cLS heme $\{FeNO\}^7$ species. The RR and FTIR characterization of this Fe^{II}-Fe_BMbNO complex reveal unusual δ(Fe-NO) and ν(NO) frequencies. The ν(NO) modes observed at 1549 cm^{-1} is the lowest ν(NO) frequencies ever reported for heme-nitrosyl complexes (Thomas *et al.*, 2001; Coyle *et al.*, 2003) while the δ(Fe-NO) is high (Table 5.1). Overall, these vibrational data are consistent with a small Fe-N-O angle which favors an $[Fe^{III}NO^-]$ resonance structure with increased backbonding from the Fe dπ electrons to the NO π* orbital (Vogel *et al.*, 1999; Coyle *et al.*, 2003). The presence of Fe^{II} at the Fe_B site is likely to stabilize this $[Fe^{III}\ NO^-]$ resonance structure, possibly via electrostatic interaction. Characterization of the Zn^{II}-Fe_BMb(NO) complex will be valuable to this interpretation. The interaction between the heme-bound NO and high-spin Fe_B^{II} is further evidenced by the EPR silent character of the complex which contrast with the g ~2 signal observed in apo-Fe_BMb(NO). Magnetic coupling between the $S = 1/2$ heme $\{FeNO\}^7$ and $S = 2$ high-spin Fe_B^{II} may results in a total spin of $S = 3/2$ or $S = 5/2$ and should be detectable at liquid helium temperature.

Further addition of NO to the Fe^{II}-Fe_BMb(NO) results in a further blue-shift of the Soret in the UV-vis spectrum, consistent with NO reacting with the 1 equiv NO adduct but do not produce N_2O, even after 16 hours incubation at room temperature. Our vibrational analysis shows that exposure to excess NO leads to a Fe^{II}-Fe_BMb$(NO)_2$ complex (Table 5.1 and Figure 5.11). This [5cLS heme Fe-NO • ON-Fe_B] *trans*-dinitrosyl complex is unreactive as previously observed in heme/non-heme diiron synthetic models by Karlin's group (Wasser *et al.*, 2005). Yet, others have assigned [heme Fe-NO • ON-Fe_B] *trans*-dinitrosyl complexes to NO reduction turnover (Kumita *et al.*, 2004; Collman *et al.*, 2008). Additional attempts to facilitate NO reduction turnover in Fe^{II}-Fe_BMb were unsuccessful. Varying the concentration of NO or protein, or the number of metal equivalent does not lead to NO reduction turnover. The reasons for this striking difference in reactivity of seemingly similar *trans*-dinitrosyl complexes are yet to be understood. One possible explanation is that the 5cLS heme-NO is less reactive

toward the second NO than a 6cLS heme-NO species. Indeed, decreased nucleophilicity of heme-bound NO of 5cLS species compared to that of 6cLS has been shown to be disadvantageous for N-N bond formation (Praneeth *et al.*, 2006).

The heme/non-heme diiron center of Fe_BMb is designed for the reductive coupling of two NO to produce N_2O by catalysis by approximation. However, the fact that we could not drive the reductive coupling of adjacent stable iron-nitrosyl complexes suggests that putative NO reduction mechanism of NORs may be over simplified and that other factors might also need to be considered, or that formation of *trans*-dinitrosyl complex is inhibitory. We are currently working on optimizing the reaction conditions that drive efficient NO reduction turnover. Different pH, presence of reduction agents, and incorporation of other metals at Fe_B site will be tested. The results of this study provide a clear framework for further structural-tuning of the NOR models and mechanistic insight into NO reduction by bacterial NORs.

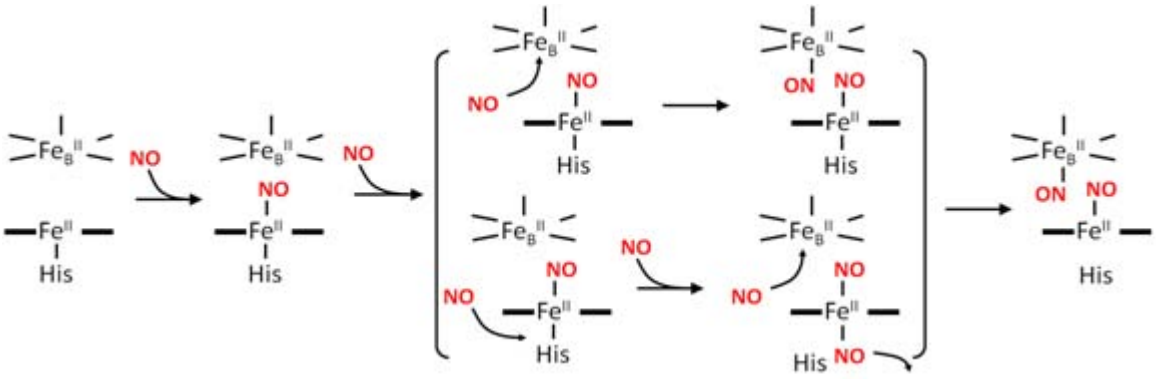

Figure 5.11 Summary of the NO reaction with the reduced Fe^{II}-Fe_BMb with NO based on results presented here.

CHAPTER 6
NO REDUCTION MECHANISM IN FLAVODIIRON PROTEINS

6.1 Flavodiiron proteins (FDPs); scavenging NO reductases

Flavodiiron proteins (FDPs) are widespread among bacteria, archaea, and some protozoan pathogens. FDPs are initially thought to be scavenging O_2 reductases, protecting air-sensitive microorganism against oxidative stress (Chen *et al.*, 1993; Gomes *et al.*, 1997; Frazao *et al.*, 2000). However, accumulated evidences suggest that, at least in some bacteria, FDPs also function as scavenging NO reductases (Gardner *et al.*, 2002; Gomes *et al.*, 2002).

FDPs are soluble cytoplasmic enzymes that are unrelated to the membrane-bound denitrifying NORs (see Chapter 1.3). The minimum functional unit of all structurally characterized FDPs is a 'head-to-tail' homodimer: the N-terminal domain of each subunit contains a non-heme diiron site (Fe1-Fe2 distance 3.2-3.6 Å), while the C-terminal domain binds a flavin mononucleotide (FMN) cofactor ~5 Å away from the diiron site in the opposite subunit (Figure 6.1). The non-heme iron center of the diiron site contains two histidine ligands, a terminal monodentate carboxylate ligand, and carboxylate- and oxo/hydroxo- briding ligands. These diiron centers are reminiscent of those of the non-heme carboxylate-bridged diiron proteins, including subunit R2 of ribonucleotide reductase (Nordlund *et al.*, 1990; Voegtli *et al.*, 2003), the hydroxylase component of soluble methane monooxygenase (MMOH) (Rosenzweig *et al.*, 1993; Whittington and Lippard, 2001), and the Δ^9-stearoyl-acyl carrier protein desaturase (Δ9D) (Lindqvist *et al.*, 1996), although there is no detectable amino acid sequence homology between any of these latter enzymes and FDPs.

---

*Material in this chapter has been published in this or similar form in *Biochemistry*, and is used here with permission of the American Chemical Society.

Hayashi T., Caranto J., Wampler A.D., Kurtz M.D., and Moënne-Loccoz P. (2010) Insight into the Nitric Oxide Reductase Mechanism of Flavodiiron Proteins from a Flavin-Free Enzyme. ***Biochemistry***, 49, 7040-7049.

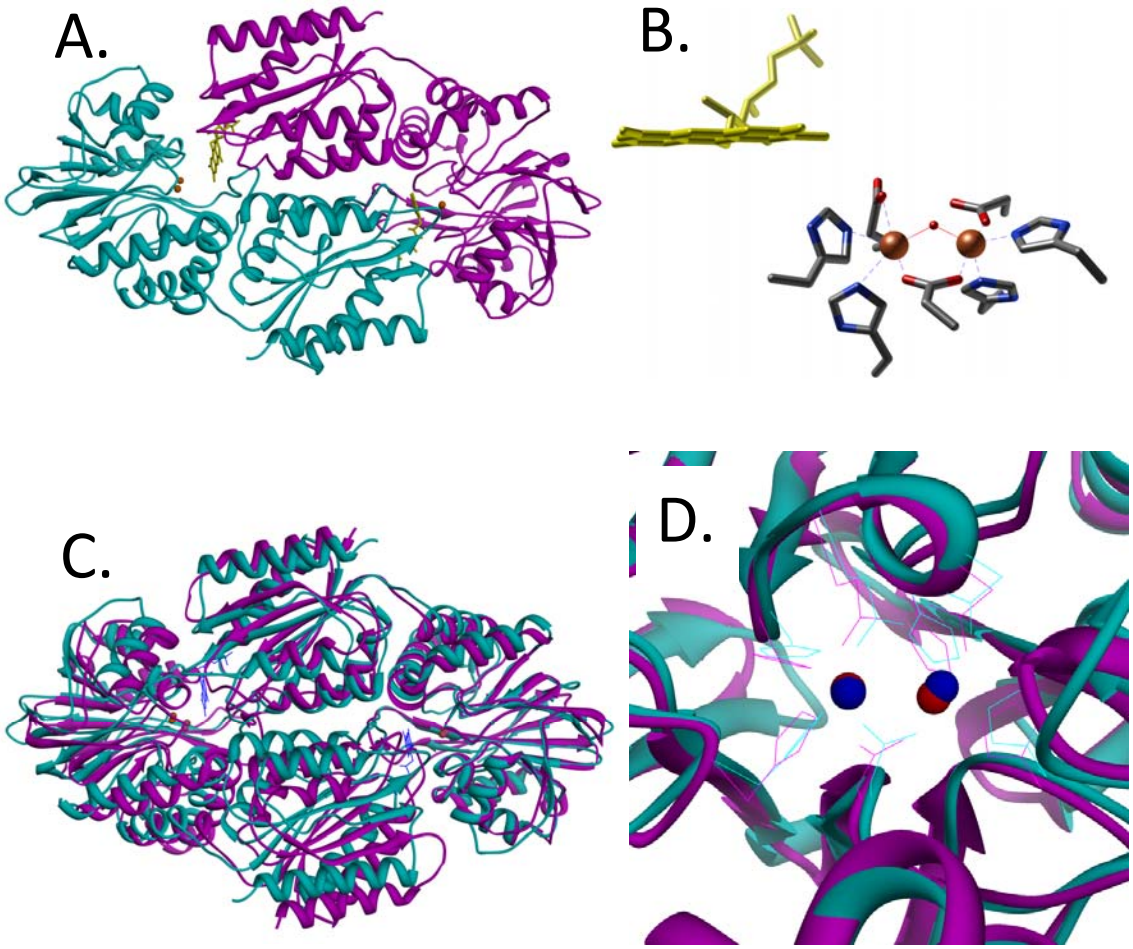

Figure 6.1 Overall structure (A) and zoom-in on the diiron center (B) of FDP from *Moorella thermoacetica*. Overall structure (C) and zoom-in on the diiron center (D) of *Mt* FDP (magenta) superposed with *Tm* FDP (cyan) which has no FMN bound. PDB ID for *Tm*FDP and *Mt*FDP are 1YCF and1VME, respectively.

6.2 Proposed NO reduction mechanisms for FDPs

Several NO reduction mechanisms have been proposed for FDPs (Kurtz, 2007). Super-reduction of a diferrous-dinitrosyl precursor to a diferrous-dinitroxyl, i.e. $[\{FeN(H)O\}^8]_2$, by the proximal $FMNH_2$ has been proposed to provide an energetically favorable route for proton delivery and N-N bond formation leading to the release of N_2O and water (Figure 6.2) (Silaghi-Dumitrescu *et al.*, 2005; Kurtz, 2007). A computational study, however, suggested an alternative mechanism involving a formally diferric-hyponitrite intermediate (Figure 6.2) (Blomberg *et al.*, 2007). An analogous hyponitrite pathway is also presumed to occur in the denitrifying NORs (Blomberg *et al.*, 2007; Moënne-Loccoz, 2007). Thus, in the super-reduction mechanism $FMNH_2$ is essential for turnover of the diferrous-dinitrosyl, whereas in the hyponitrite intermediate mechanism, protonation of the spontaneously formed diferric-hyponitrite intermediate leads directly to release of N_2O without participation of the FMN.

In principle these mechanisms could be distinguished by examining the reactivity of the diiron site with NO in the absence of the FMN cofactor. In 2004, a crystal structure of an FDP from the thermophilic bacteria, *Thermotoga maritima* (*Tm*) was deposited into the Protein Data Bank (PDB code: 1VME) by the Joint Center for Structural Genomics. The diiron site structure in *Tm* FDP is very similar to that in other FDPs (Figure 6.1), but the proximal FMN cofactor is absent in the deposited *Tm* FDP structure. This latter structure, thus, suggests the possibility of characterizing the reactivity of the diiron site in the flavin-free *Tm* FDP.

In order to test these alternative mechanisms, we examined a deflavinated FDP (deflavo-FDP) from *Thermotoga maritime* (*Tm*). The deflavo-FDP retains an intact diiron site but does not show multi-turnover NOR or O_2 reductase (O_2R) activity. Reactions of the reduced (diferrous) deflavo-FDP with NO were examined by UV-vis absorption, EPR, RR, and FTIR spectroscopies. Anaerobic addition of NO up to 1 NO:diferrous deflavo-FDP results in formation of a diiron-mononitrosyl complex. Further addition of NO results in two reaction pathways, one of which produces N_2O and the diferric site and the other of which produces a stable diiron-dinitrosyl complex. Both NO-treated and as-isolated deflavo-FDPs regain full NOR and O_2R activities upon simple addition of FMN. The production of N_2O upon addition of NO to the mononitrosyl deflavo-FDP supports

the hyponitrite mechanism. Yet, the concomitant formation of a stable diiron-dinitrosyl complex in the deflavo-FDP may be viewed as an alternate reaction path at high NO concentration conditions where the flavinated enzyme can function via a super-reduction mechanism. These two reaction pathways are discussed within the context of NO reduction by FDPs in general.

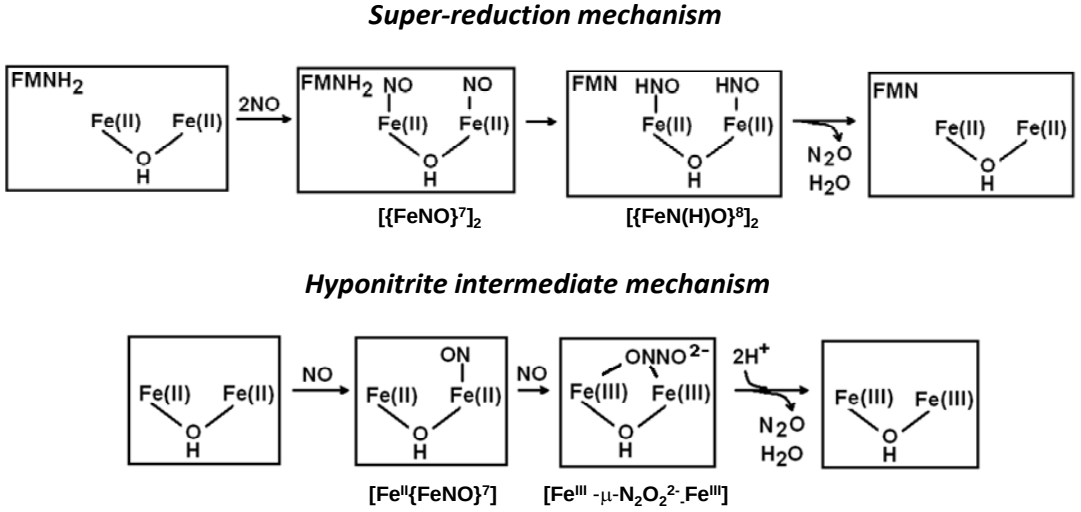

Figure 6.2 Proposed NO reduction mechanisms for FDPs. Super-reduction mechanism (top) and hyponitrite-intermediate mechanism (bottom).

6.3 Materials and methods

Protein preparations.

All protein concentrations are expressed either in monomers or, where indicated, on the basis of FMN content. The expression and purification of recombinant *Tm* FDP (GeneID TM0755), *Tm* rubredoxin (Rd), and *Tm* NADH:rubredoxin oxidoreductase (NROR) (Hillmann *et al.*, 2009), iron, protein and flavin analyses were carried out as described elsewhere.

FDP deflavination and reflavination.

Approximately 20 mg of as-isolated *Tm* FDP was applied to a 50-mL phenyl sepharose column (GE Healthcare) with buffer A (50 mM MOPS, 100 mM Na_2HPO_4, 100 mM $KC_2H_3O_2$ and 1.2 M NH_4SO_4 at pH 7.4) to immobilize the FDP. The column pH was then lowered using a 20-column-volume gradient from buffer A to buffer B (50 mM MOPS, 100mM Na_2HPO_4, 100 mM $KC_2H_3O_2$ and 1.2 M NH_4SO_4 at pH 2.5). FMN (yellow band) was eluted from the column at pH 2.5 with buffer B. The column pH was returned to pH 7.3 using a 20-column-volume gradient from buffer B to buffer A. The deflavinated FDP (deflavo-FDP) was eluted with 50 mM MOPS, pH 7.3. Excess salt was removed by washing the concentrated deflavo-FDP with 50 mM MOPS, pH 7.3 in an Amicon 30 kDa cutoff centrifugal filter unit (Millipore) and the protein was stored in 50 mM MOPS at pH 7.4. Deflavo-FDP was quantitatively reflavinated (reflavo-FDP) by incubating a 5 mole FMN:1 mole (in monomer) deflavo-FDP mixture ([approximate FDP] = 2 mM) at 37 ^oC for ~15 minutes. Excess FMN was removed by centrifugal filtration washing with 50 mM MOPS pH 7.3 until the flow-through was colorless.

O_2R/NOR activity assays and N_2O production measurements.

NADH-dependent O_2R and NOR activities were measured spectrophotometrically by monitoring NADH consumption rates (ε_{340} = 6220 $M^{-1}cm^{-1}$), as reported earlier. Assays were typically carried out in 50 mM MOPS pH 7.4 with 0.1 mM EDTA, and the sequential addition of NADH (100-200 μM), Rd (2-10 μM), NROR (0.1 μM for the O_2-reduction and 0.2 μM for the NO-reduction), and FDP (50 nM-1 μM for the O_2-reduction

and 9 to 17 μM for the NO-reduction (concentrations on an FMN or diiron basis). Small volumes of aqueous O_2- or NO-saturated stock solutions were injected into the initially anaerobic assay solutions to initiate the reactions. Alternatively, gaseous air or 0.1 atm NO was introduced into the headspace of the initially anaerobic UV-vis cuvette containing the assay solutions, which were stirred in order to maximize equilibration with the headspace gas. N_2O production measurements were performed as described in Chapter 4.2.

Preparation of NO adducts

Fully reduced deflavo-FDPenzyme was obtained either by titration to achieve a slight stoichiometric excess of sodium dithionite or by addition of excess dithionite followed by removal of the reducing agent with a desalting spin column (Zebra, Pierce).

Complete reduction of flavinated FDP (~100 μM in 50 mM MOPS pH 7.4) was achieved after 4 h incubation with 1 mM NADH, 4 μM Rd and 0.4 μM NROR. The NADH excess was removed using a spin column inside the glove box and the sample was concentrated down to reach 1 mM in diiron concentration. 1 equiv and excess NO addition to protein solution is achieved as described in Chapter 2.2.

Molecular spectroscopies.

UV-vis, RR, and FTIR spectroscopy were performed as described in Chapter 2.2. Typical enzyme concentrations for RR experiments were 1 mM. Approximately 15 μL of 1.2 mM protein solutions were loaded in FTIR cells with a 15-μm pathlength. The complete reversibility of the photolysis processes described below was confirmed by reproducing the same FTIR difference spectra after sample annealing process.

6.4 Characterization of Tm FDP and FMN-free *Tm*FDP (deflavo-FDP)

O_2R and NOR activities of *Tm*FDP were measured via NADH consumption using the *Tm* redox protein components, NROR and Rd (Figure 6.3). The turnover numbers of O_2R and NOR activities are determined to be >150 μM NADH / min-μM [E] and ~1 μM NADH / min-μM [E] (Figure 6.4). Neither activity is observed if any one of the protein components (FDP, NROR or Rd) is omitted from the assay solutions.

Complete removal of FMN from as-isolated *Tm* FDP is achieved by an acid-wash (pH 2.5) of the protein bound to phenyl sepharose prior to elution of deflavo-FDP at pH 7.3. The deflavo-FDP consistently retains 2 Fe per protein monomer. As expected, the UV-vis absorption features of FMN are absent from the spectrum of the *Tm* deflavo-FDP (Figure 6.4). The integrity of the diiron site in the absence of FMN is supported by the crystal structure of *Tm* FDP which has no FMN bound and shows a diiron site structure and overall protein fold very similar to those observed in the crystal structure of *Mt* FDP (Figure 6.1). The deflavo-FDP has no detectable multi-turnover O_2R or NOR activity (Figure 6.4), but the deflavo-FDP can be quantitatively reconstituted with FMN to show full restoration of O_2R and NOR activity.

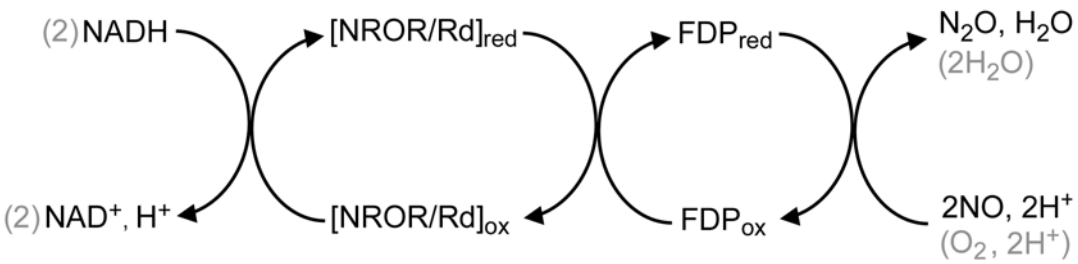

Figure 6.3 Schematic representation of electron transfer chain coupling NADH oxidation to O_2 or NO reduction by FDP. Rd; rebredoxin, NROR; NADH: rubredoxin oxidoreductase.

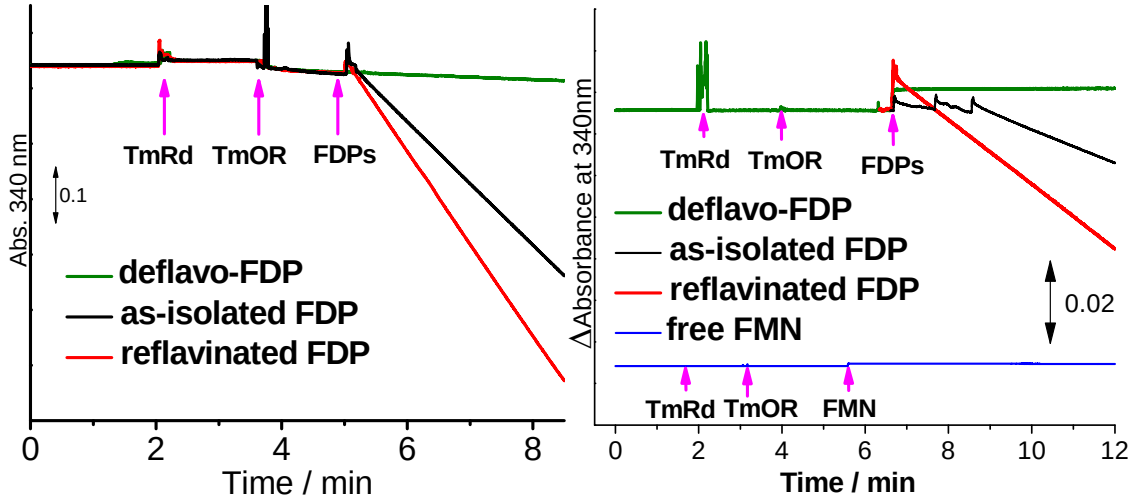

Figure 6.4 O_2R activity assay (top), and NOR activity assays (bottom) of deflavinated, as-isolated (~50% FMN occupancy), and reflavinated *Tm* FDP. Extinction coefficients are based on protein monomer. O_2R and NOR activities were determined in air-saturated solutions or NO solutions equilibrated with a headspace containing 0.1 atm NO partial pressure, as described in Materials and Methods. The arrows indicate times of additions of protein components or FMN. To facilitate comparison of O2R and NOR activities, all traces were normalized to 1 μM final concentration in protein monomer or FMN concentration.

6.5 The reaction of deflavo-FDP with NO

Reduction of deflavo-FDP with dithionite results in the loss of broad absorption features between 350 and 420 nm that originate from carboxylate and bridging oxo/hydroxo-to-iron^{III} LMCT transitions (Figure 6.5), and results in reduction of diferric to diferrous deflavo-FDP. Addition of up to 1 equiv NO to reduced deflavo-FDP produces a pale yellow color associated with absorption bands at 420, 455, and 638 nm (Figure 6.5). These absorption features are characteristic of nitrosyl-to-iron LMCT transitions of non-heme $\{FeNO\}^7$ complexes with O/N ligands (Table 6.1). At 1 equiv NO per diiron site, the 420/455-nm absorption corresponds to a $\varepsilon_{420/455\ nm} \sim 1{,}000\ M^{-1}\ cm^{-1}$ which is a good match for non-heme $\{FeNO\}^7$ species in proteins and synthetic model complexes (Table 6.1). The high absorbance at 420/455 nm reached with 1 equiv NO also suggests that the diiron(II) site binds NO with high affinity. We refer to this 1 equiv

NO:diiron complex as deflavo-FDP(NO) hereafter. Further addition of NO, up to 2 equiv, results in a significant loss of the nitrosyl-to-iron LMCT bands in favor of absorption increases below 420 nm (Figure 6.5). These absorption changes suggest that, above 1 equiv NO added per diiron site promotes the formation of oxidized, presumably diferric, deflavo-FDP. However, this conversion is incomplete, and further NO addition results in increased absorptions at 455 nm and 638 nm. These rising absorption features at high NO concentrations are assigned to a deflavo-FDP$(NO)_2$ complex that forms in parallel with oxidized deflavo-FDP (see below).

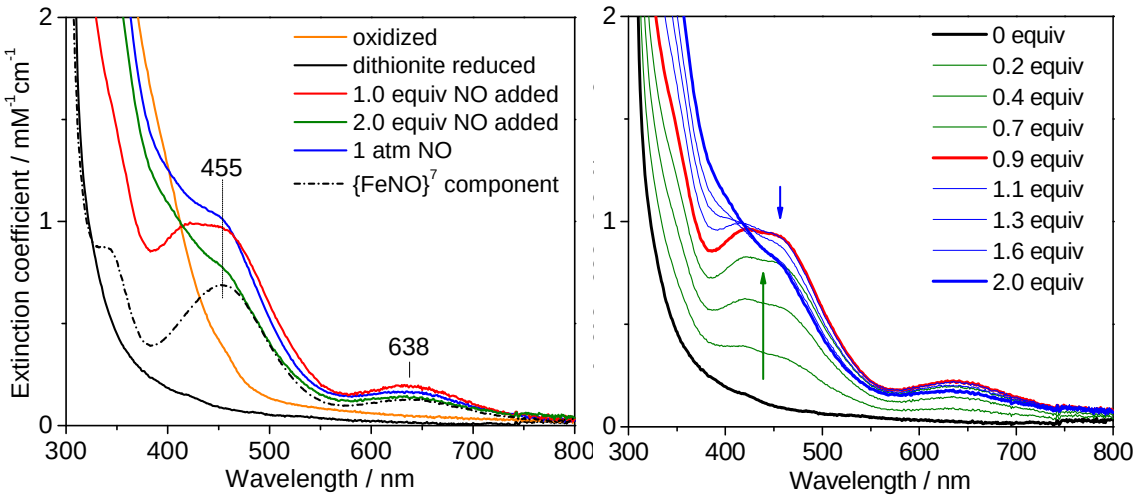

Figure 6.5 UV-vis spectra of oxidized (orange), dithionite reduced (black), and reduced deflavo-FDP after addition of 1 equiv (red), 2 equiv (green) and 1 atm NO (blue) at room temperature (top). Also shown is the difference spectrum [1-atm NO spectrum] – 0.65 [oxidized spectrum] (black dashed line). UV-vis spectra monitoring the titration of reduced deflavo-FDP with up to 2.0 equiv of NO (bottom). Protein concentration = 147 μM in 50 mM MOPS pH 7.4; extinction coefficient per diiron site.

Table 6.1 Spectroscopic properties of non-heme ferrous-nitrosyl complexes containing O/N ligands.

$\{FeNO\}^7$ species	λmax (nm) (ε in M^{-1} cm^{-1})[a]	ν(Fe-NO) ($\Delta^{15}N$) (cm^{-1})	δ(Fe-N-O) ($\Delta^{15}N$) (cm^{-1})	ν(N-O) ($\Delta^{15}N$) (cm^{-1})	References
Deflavo-FDP-(NO)	420, 455(1000)	451 (-9)		1680 (-28)	this work
Deflavo-FDP-$(NO)_2$	455 (1000)	459 (-7)	444 (-8)	1749 (-30)	this work
Wild-type R2-$(NO)_2$	450 (760)	445 (-7)	434 (-9)	1742 (-29)	(Haskin *et al.*, 1995; Lu *et al.*, 2004)
D84E-R2-$(NO)_2$	450 (1200)	454 (-8)	442 (-8)	1735 (-30)	(Lu *et al.*, 2004)
Hemerythrin-(NO)	408 (1000)	433 (-6)	421 (-6)	not obs.	(Nocek *et al.*, 1988)
Superoxide reductase-(NO)	475 (530)	475 (-7)		1721 (-31)	(Clay *et al.*, 2003)
Fe(EDTA)-(NO)	434 (900)	496 (-4)	493 (-10)	1776 (-37)	this work and (Orville and Lipscomb, 1993; Brown *et al.*, 1995)
$[Fe_2(NO)_2(\mu$-XDK$)(\mu$-$O_2CPh)(ImH)_2(O_2CPh)$-(MeOH)]	450 (1,000)	n.r.[b]	n.r.[b]	n.r.[b]	(Lu *et al.*, 2004)
$Fe_2(NO)_2$(Et-HPTB)$(O_2CPh)(BF_4)_2$	n.r.[b,c]	n.r.[b]	n.r.[b]	1785	(Feig *et al.*, 1996)

[a] per iron.

[b] not reported.

[c] obscured by ligand absorptions.

The NO adducts that form at high vs low added NO:protein ratios can be distinguished by their sensitivity towards dithionite. Specifically, when the deflavo-FDP(NO) complex is exposed to a 2-fold molar excess of dithionite at room temperature, the nitrosyl-to-iron LMCT transitions are bleached in a monotonous fashion and with a slow apparent $t_{1/2} \sim 15$ min (Figure 6.6A). In contrast, the 455-nm absorption due to the deflavo-FDP$(NO)_2$ complex formed with excess NO decays within the manual mixing time (Figure 6.6B). This rapid bleaching is accompanied by the slower reduction of the oxidized diiron sites; the residual absorption that decays at an even slower rate is likely to correspond to a small population of mixed-valent $Fe^{III}Fe^{II}$ sites (Figure 6.6B). This interpretation is supported by the UV-vis spectral changes observed for the reaction of 2 equiv dithionite with oxidized deflavo-FDP (Figure 6.6C). In this experiment, the spectrum obtained immediately after mixing is distinct from that of the oxidized deflavo-FDP, and the relative absorbance loss near 400 nm and gain at ~500 nm can be assigned to mixed-valent diiron contributions; subsequent traces show a slow bleaching of these visible absorptions that is equivalent to the later changes observed during dithionite reduction of the deflavo-FDP$(NO)_2$/oxidized deflavo-FDP mixture. Taken together, these data suggest that the bleaching of the deflavo-FDP(NO) complex by dithionite reflects the slow NO off-rate from the mononitrosyl complex as dithionite scavenges free NO from solution. The NO off-rate from the deflavo-FDP$(NO)_2$ is significantly higher as confirmed by the rapid decay of this complex within the manual mixing time in NO-free buffer (data not show). Thus, the reaction of deflavo-FDP$(NO)_2$ with dithionite most likely reflect this slow NO off-rate, but a 'super-reduction' of deflavo-FDP$(NO)_2$ by dithionite to produce N_2O cannot be ruled out. The fraction of oxidized deflavo-FDP present in the mixture produced by exposure of the reduced protein to high NO is re-reduced slowly by dithionite with formation of mixed-valent and diferrous states.

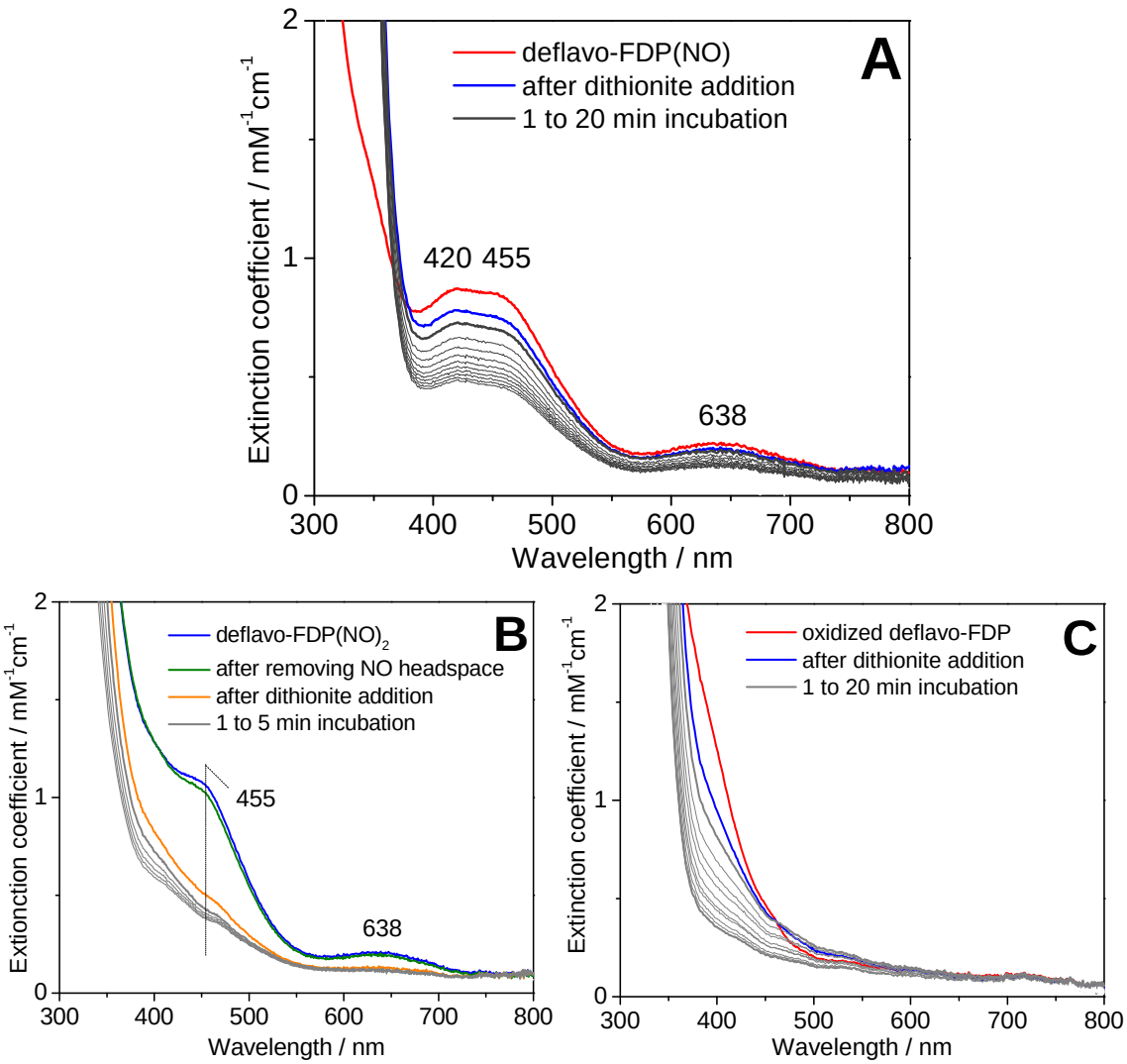

Figure 6.6 UV-vis spectra of deflavo-FDP(NO) (A), deflavo-FDP$(NO)_2$ (B), and oxidized deflavo-FDP (C), before and after addition of sodium dithionite (initial concentrations [FDP] = 60 μM, [dithionite] = 120 μM).

The picture that emerges from these experiments is that the deflavo-FDP diferrous site binds one NO molecule with relatively high affinity before further reaction with excess NO to produce a mixture of oxidized deflavo-FDP and unreactive $\{FeNO\}^7$ centers (Figure 6.7). Presuming the as-isolated spectrum is equivalent to the post-NO treated oxidized spectrum, we subtracted its contribution to the absorption spectra; the remaining spectra correspond to the fraction of non-heme $\{FeNO\}^7$ complexes with absorption bands at 455 and 638 nm (Figure 6.8). Using this analysis, the fraction of

oxidized protein resulting from the excess NO treatment was consistently reproducible for individual deflavo-FDP preparations, typically ranging from 60 to 70%, reaching 40% for one of the preparations (Figure 6.8). The origin of this variability is currently unclear. The remaining absorbance at 455 nm corresponds to a molar extinction coefficient of ~1,000 $M^{-1}cm^{-1}$ per iron. This value is again in good agreement with other non-heme $\{FeNO\}^7$ complexes (Table 6.1) and suggests that the diiron sites that do not proceed to the diiron(III) state instead form stable diferrous-dinitrosyl $[\{FeNO\}^7]_2$ clusters, as previously observed with reduced R2 exposed to excess NO (Haskin *et al.*, 1995; Lu *et al.*, 2004).

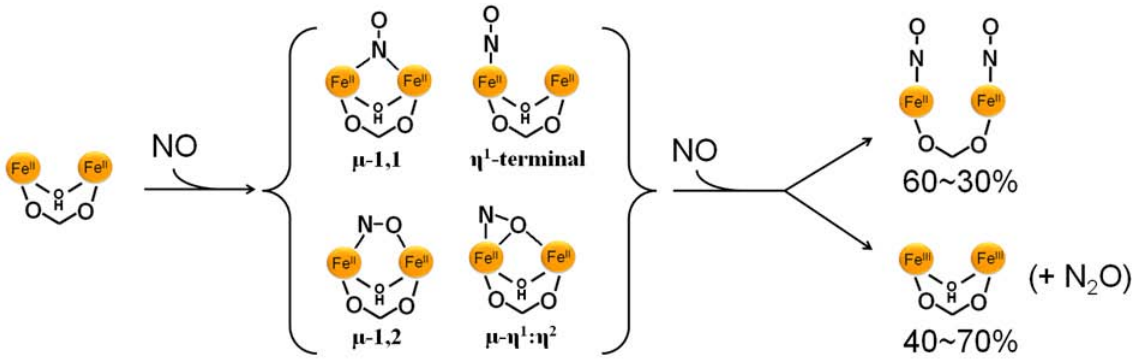

Figure 6.7 Schematic representations of the reaction of deflavo-FDP with NO based on the UV-vis results. Possible structures of one NO bound deflavo-FDP are also depicted. The solvent bridge is expected to be lost upon formation of the diferrous-dinitrosyl $[\{FeNO\}^7]_2$ complex (vide infra).

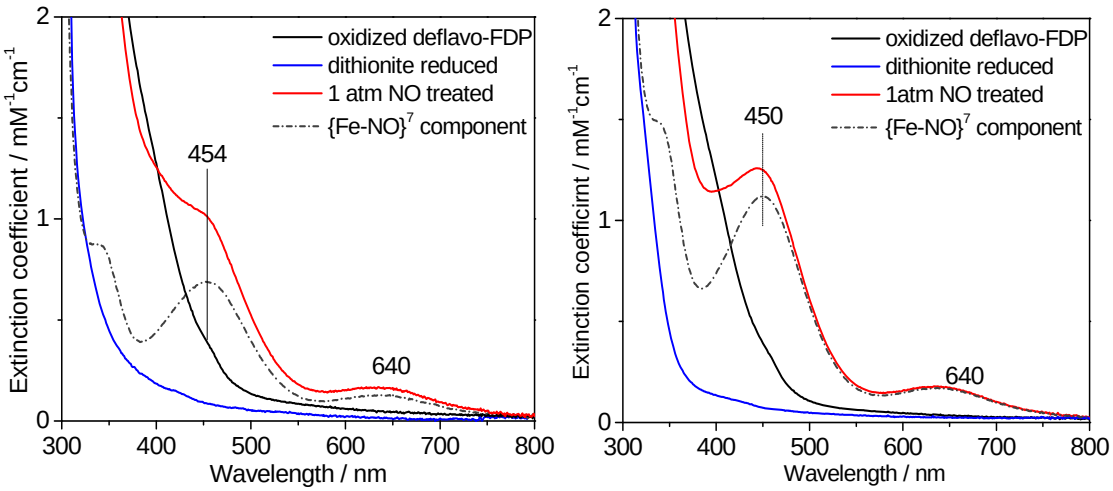

Figure 6.8 UV-vis spectra of oxidized (black), dithionite reduced (blue), and 1 atm NO treated (red) deflavo-FDP for two different preparations. Also shown, are the difference spectra generated after subtracting contributions from the diferric product spectra (0.65 and 0.4 subtraction factor for the upper and lower panels, respectively). The samples were in 50 mM MOPS pH 7.4 and the extinction coefficients are per diiron site.

6.6 FTIR evidence for N_2O production

Consistent with the preceding UV-vis absorption analysis, FTIR spectroscopy shows production of N_2O from the reaction of excess NO with reduced deflavo-FDP. Specifically, we detect the N-N stretching mode of N_2O at 2330 cm^{-1} in the FTIR spectra of deflavo-FDP samples and compare these measurements with data for myoglobin and terminal oxidases as negative and positive controls, respectively (Figure 6.9). The intensity of the FTIR band at 2330 cm^{-1} upon completion of the reaction reveals that ~0.7 equiv of N_2O is formed per deflavo-FDP diiron sites, which closely matches the estimated fraction of oxidized diferric deflavo-FDP from UV-vis absorption spectroscopy. A comparable FTIR experiment with fully reduced reflavinated FDP exposed to excess NO from NONOate shows ~2.0 equiv N_2O produced per FDP diiron site (Figure 6.9), which confirms that all reducing equivalents are used to produce N_2O.

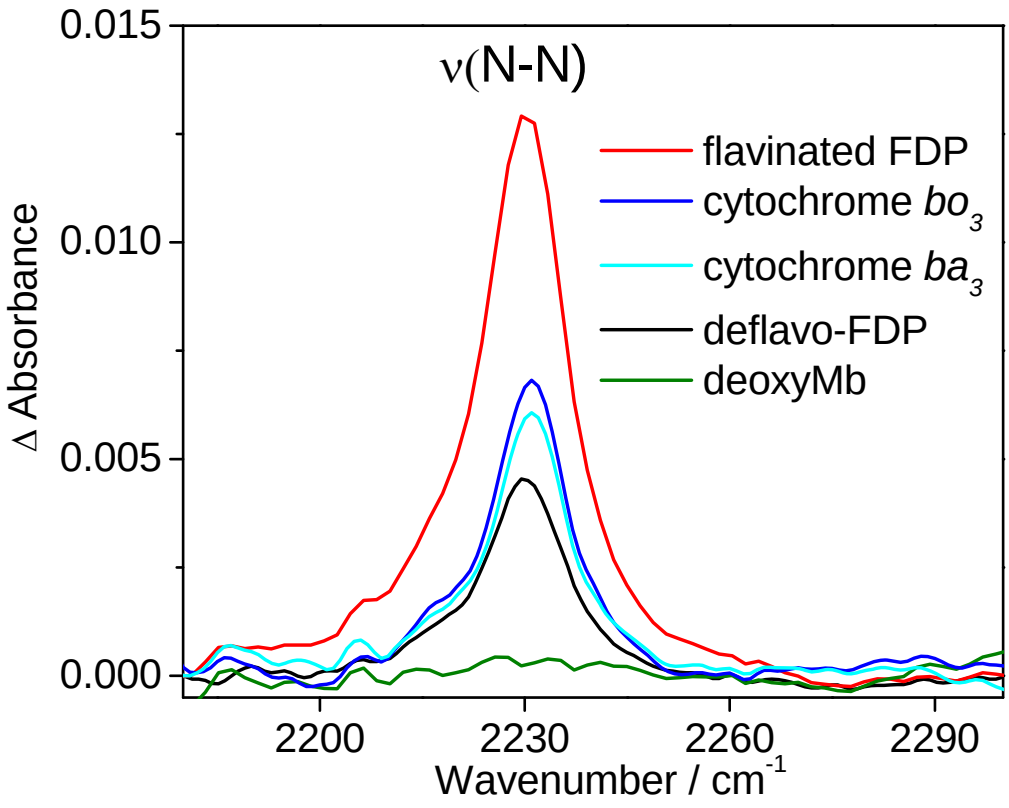

Figure 6.9 FTIR detection of N_2O produced by reduced flavinated FDP (red: 1 mM, 100 % FMN occupancy), reduced deflavo-FDP (black: 1 mM diiron) deoxymyoglobin (green: 2 mM) after incubation with excess NONOate to produce 4 mM NO. Also shown, are the FTIR spectra from multi-turnover reactions of reduced cytochrome bo_3 (blue: 50 μM) and ba_3 (light blue: 50 μM) in presence of 10 mM ascorbate and 0.1 mM TMPD and after incubation with 2 mM NO produced from NONOate.

6.7 Formation of $S = 1/2$ deflavo-FDP(NO) and $S = 3/2$ deflavo-FDP(NO)$_2$

As established earlier for native FDPs (Silaghi-Dumitrescu *et al.*, 2003; Vicente and Teixeira, 2005; Vicente *et al.*, 2009), the oxidized diiron site of deflavo-FDP is EPR silent as bridging solvent and carboxylate ligands promote antiferromagnetic coupling of the two non-heme iron(III) ions (Figure 6.10). The dithionite-reduced deflavo-FDP is also EPR silent, as expected for a fully reduced diiron(II) site with no evidence for the formation of mixed valent $Fe^{II} \bullet Fe^{III}$ cluster, as observed previously in redox titration of FDPs (Figure 6.10) (Vicente and Teixeira, 2005; Vicente *et al.*, 2009). Addition of 1 equiv of NO results in the appearance of a broad axial EPR signal centered at $g \sim 2$ which we assign to an $S = 1/2$ diiron-mononitrosyl species produced by antiferromagnetic coupling of an $S = 2$ Fe^{II} to an $S = 3/2$ $\{FeNO\}^7$ species (Figure 6.10). This EPR spectrum is reminiscent of the axial signals of hemerythrin-NO adducts with $g_{//}$ and $g_{\perp}$ near 2.8 and 1.8, respectively (Nocek *et al.*, 1988), although the anisotropic components of deflavo-FDP(NO) are more difficult to pinpoint since the splitting is small and the g strain on both $g_{//}$ and $g_{\perp}$ are relatively large. Double integrations of the EPR signal of deflavo-FDP(NO) against Cu^{II}EDTA standards indicate that the axial $g \sim 2$ signal represents 0.75 spin per diiron site. This deviation from stoichiometry is easily explained by some dissociation of NO from deflavo-FDP(NO) complex prior to freezing the EPR tubes since the complex is prepared without NO excess; a slight overshot in the NO addition, above 1 equiv, will also lower the deflavo-FDP(NO) content to produce a fraction of diferric deflavo-FDP. As expected from the UV-vis experiments, the $g \sim 2$ EPR signal from the diiron-mononitrosyl complex disappears upon addition of 2 equiv NO, concomitant with the appearance of new EPR resonances near $g \sim 4$ (Figure 6.10).

These EPR features at $g \sim 4$ are consistent with rhombic EPR signatures from $S = 3/2$ $\{FeNO\}^7$ species (Westre *et al.*, 1994; Brown *et al.*, 1995). Comparing double integrations of these signals with those of Fe^{II}EDTA(NO) standards shows that less than 3% of the total iron content contribute to this regions of the EPR spectra in deflavo-FDP samples treated with 2 equiv NO, but that this value rises to ~30% of the total iron when the free NO concentration is increased to 100 μM with an 0.05 atm NO_g headspace (Figure 6.10). Further increases in free NO concentration do not affect the intensity of the $g \sim 4$ signals (data not shown). The multiplicity of $g \sim 4$ resonances is readily assigned to

two distinct $S = 3/2$ $\{FeNO\}^7$ species, a more rhombic one with $g = 4.37, 3.68, 2.00$ and another with $g = 4.14, 3.93, 2.0$ (Figure 6.10). While the more rhombic signal represents a minor species at all NO concentrations, the more axial species becomes prominent at the higher NO concentration. The quantitation of the $g \sim 4$ signals matches well with the ~30% of diferrous-dinitrosyl $[\{FeNO\}^7]_2$ sites estimated from the UV-vis analysis. The EPR data, thus, imply that the remaining 30% of deflavo-FDP diiron sites form $\{FeNO\}^7$ centers that are magnetically uncoupled. This observation is in striking contrast with the magnetically coupled, EPR-silent diferrous-dinitrosyl $[\{FeNO\}^7]_2$ sites of $R2(NO)_2$ (Haskin *et al.*, 1995; Lu *et al.*, 2004).

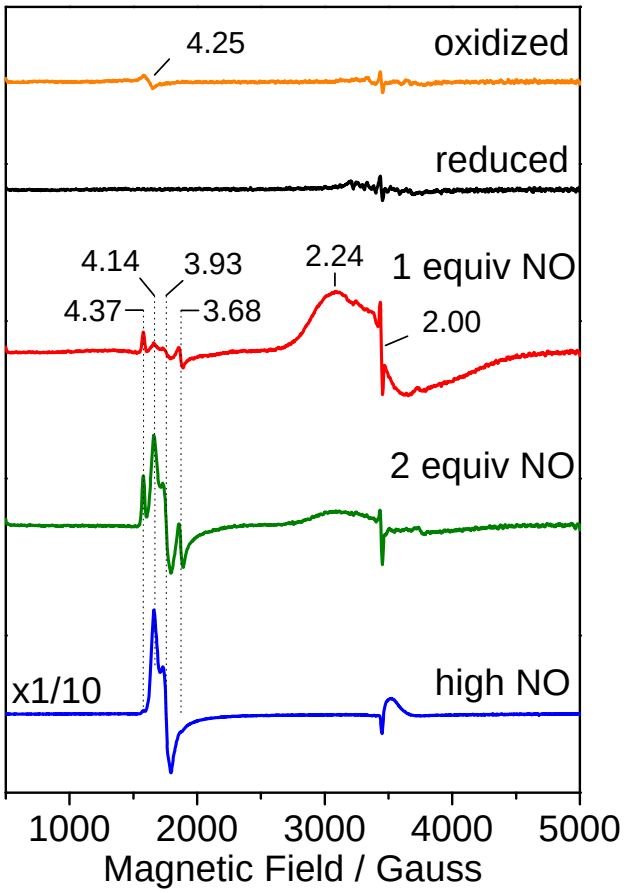

Figure 6.10 EPR spectra of oxidized deflavo-FDP (orange), dithionite-reduced deflavo-FDP (black), and reduced deflavo-FDP after the addition of 1 equiv (red), 2 equiv (green) and 0.05 atm NO headspace (blue) at 4.2 K. Conditions: protein concentration of 100 μM, 100 μM in 50 mM MOPS pH 7.4; microwave frequency, 9.66 GHz; microwave power, 2 mW; modulation amplitude, 10 G.

6.8 Vibrational characterization of deflavo-FDP NO complexes

The deflavo-FDP$(NO)_2$ complex prepared with excess NO is sufficiently stable to allow extended acquisition times for optimal RR spectral characterization. As expected, the RR spectra obtained with 458-nm laser excitation revealed enhancement of vibrational modes associated with the $\{FeNO\}^7$ unit (Figure 6.11 and Table 6.1). A band at 459 cm^{-1} that downshifts to 452 (-7) and 447 (-12) cm^{-1} with ^{15}NO and $^{15}N^{18}O$, respectively, is assigned to the ν(Fe-NO) mode. In the high frequency region, a band at 1749 cm^{-1} downshifts to 1719 (-30) and 1679 (-70) cm^{-1} with ^{15}NO and $^{15}N^{18}O$, respectively (Figure 6.10) and is readily assigned to the ν(N-O) mode. In addition to these two Fe-N-O vibrations, another isotope-sensitive RR band is observed at 903 cm^{-1} and shifts to 888 (-15) and 879 (-24) cm^{-1} with ^{15}NO and $^{15}N^{18}O$, respectively. Comparable RR signals in the 900-cm^{-1} region for the NO adduct of R2 were assigned to a combination of bending and stretching Fe-N-O modes (Lu *et al.*, 2004). An equivalent RR band and isotope dependence are observed for the mononuclear complex, Fe^{II}EDTA(NO) (Table 6.1), which rules out some alternative assignments, such as a bound hyponitrite (Varotsis *et al.*, 2007), for this mid-frequency vibration. All of these assignments are consistent with those in Table 1 for $\{FeNO\}^7$ units in other proteins and synthetic complexes, including the deduced Fe-N-O bending/stretching combination modes.

The $[\{FeNO\}^7]_2$ complex of deflavo-FDP can also be characterized by light-induced FTIR difference spectroscopy at low temperature. The 'dark' minus 'illuminated' difference spectra obtained at 30 K show a single ν(N-O) at 1751 cm^{-1} that shifts to 1721 (-30) cm^{-1} with ^{15}NO (Figure 6.11). These frequencies are in good agreement with those observed in the RR spectra and the isotope shift matches with the predicted value for isolated diatomic vibrations. These observations support the notion that the two $\{FeNO\}^7$ units experience similar environments within the protein matrix. Nitrosyl ligands, when photo-dissociated from metal centers at cryogenic temperatures, typically remain as free NO molecules trapped with the protein pocket, and typically exhibit very weak ν(N-O) modes between 1850 and 1860 cm^{-1} (Miller *et al.*, 1997; Lu *et al.*, 2004). Such vibrations should appear as negative band(s) in the FTIR difference spectra, but so far, we have not detected such signals in a reproducible fashion in the

light-induced difference spectra of deflavo-FDP$(NO)_2$. The empty FMN-binding site may provide a more expansive pocket with multiple docking sites for the dissociated NO, which may broaden these signals beyond detection.

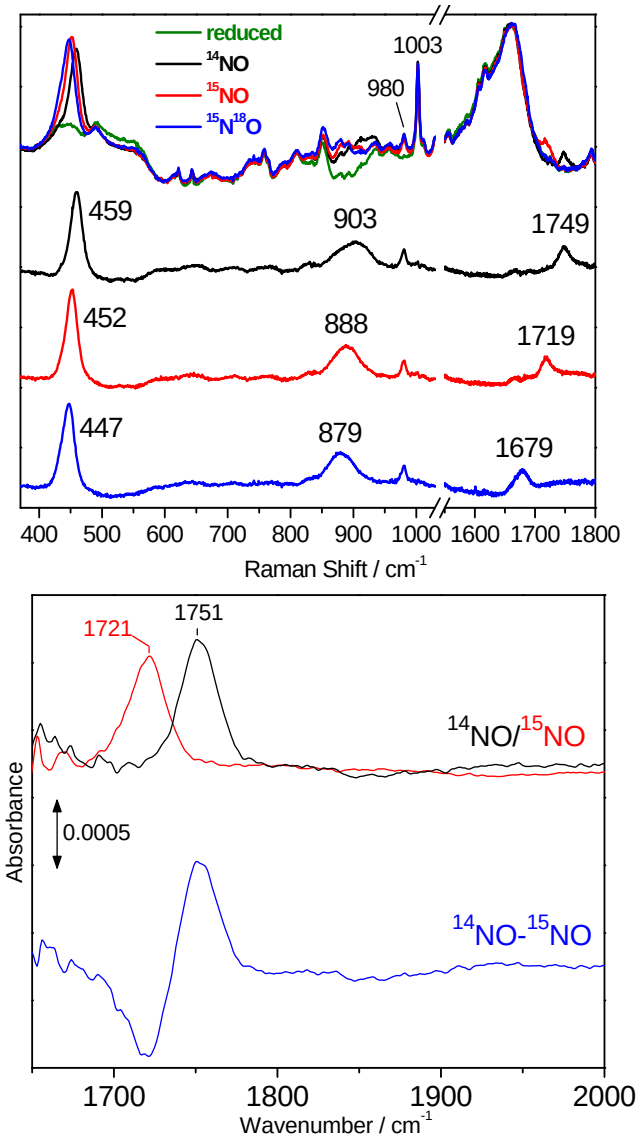

Figure 6.11 RR spectra of reduced deflavo-FDP before (green) and after exposure to excess NO (top black), ^{15}NO (top red), and $^{15}N^{18}O$ (top blue) obtained with 458-nm excitation and at room temperature (top). Also shown are 'NO complexes' minus 'reduced' difference spectra color-coded as for the top spectra. FTIR difference spectra ('dark' minus 'illuminated') of deflavo-FDP$(NO)_2$ (black) and deflavo-FDP$(^{15}N\ O)_2$ (red) obtained below 30 K (bottom).

The mononitrosyl deflavo-FDP(NO) complex forms without appreciable fractions of the dinitrosyl complex only when using ≤1 equiv NO:diiron site. Under these conditions significant dissociation and degassing of free NO can take place in RR capillaries. Nevertheless, RR spectra obtained with acquisition time of a few minutes reveal vibrational modes similar to those of the $[\{FeNO\}^7]_2$ complex, but at lower energy (Figure 6.12). A broad RR band centered at 451 cm^{-1} downshifts to 442(-9) cm^{-1} and 436(-15) cm^{-1} with ^{15}NO and $^{15}N^{18}O$, respectively. Changes in half-widths and bandshapes with different NO-isotopes in deflavo-FDP(NO) suggest that this broad band may be composed of more than one unresolved components and may reflect overlapped bending and stretching modes of the Fe-N-O unit. Due to the low signal-to-noise ratio of these RR spectra, no other vibrational modes could be clearly identified. As expected, additions of excess NO to the mononitrosyl complexes produce RR spectra equivalent to those of deflavo-FDP$(NO)_2$ (data not shown).

The light-induced FTIR difference spectroscopy at low temperature was also employed to further characterize the deflavo-FDP(NO) complex. The 'dark' minus 'illuminated' difference spectra of the NO and ^{15}NO adducts obtained at 10 K show positive and negative bands at 1680 and 1869 cm^{-1} which downshifts to 1652 (-28) and 1837 (-32) cm^{-1} with ^{15}NO, respectively (Figure 6.12). The isotope sensitivities of these bands are in good agreement with the predicted values for isolated diatomic vibrations and are consistent with ν(N-O) of the deflavo-FDP(NO) complex and free NO molecules trapped within the protein pocket.

With $^{15}N^{18}O$, the ν(N-O) splits to generate two bands with equally intensity at 1574 and 1624 cm^{-1}. These frequencies, below and above the predicted value for $^{15}N^{18}O$ of 1605 cm^{-1}, are indicative of a Fermi-coupling of ν(N-O) with another vibration of similar energy; a candidate for such vibration is an asymmetric stretching mode of bidentate carboxylate bridge which typically occurs near 1550 cm^{-1} (Gregoriou *et al.*, 1995; Costas *et al.*, 2003).

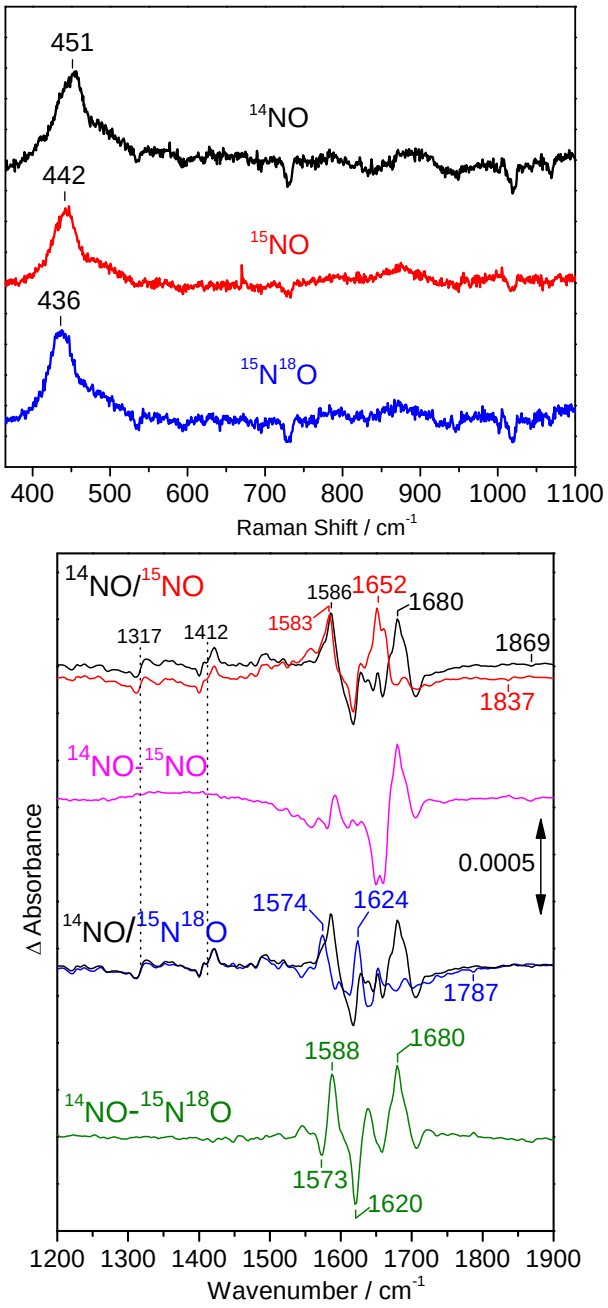

Figure 6.12 RR 'NO complexes' minus 'reduced' difference spectra of deflavo-FDP(NO) with NO (black), ^{15}NO (red), and ^{15}N^{18}O (blue) obtained with 458-nm excitation and at room temperature (top). FTIR 'dark' minus 'illuminated' difference spectra of deflavo-FDP(NO) with NO (black), ^{15}NO (red), and ^{15}N^{18}O (blue) obtained at 10 K (bottom). Also shown are differences of 'dark' minus 'illuminated' FTIR difference spectra. 'NO' minus '^{15}NO' (pink) and 'NO' minus '^{15}N^{18}O' difference spectra (green).

6.9 Formation and characterization of mononitrosyl reflavo-FDP(NO) Complex

In order to confirm the relevance of the mononitrosyl complex formed in deflavo-FDP to the native system, this complex was also prepared in reduced reflavo-FDP which contains FMN cofactor with 100% occupancy. Overnight reduction of reflavo-FDP with excess NADH in the presence of the redox partners results in loss of visible absorption, consistent with full (4 electron) reduction of reflavo-FDP (data not shown). Addition of up to 1 equiv NO to the reduced reflavo-FDP produces a pale yellow color associated with the absorption at ~500 nm, consistent with the formation of an iron nitrosyl complex. The EPR spectra of this chromophoric species reveal a broad and axial signal with $g_{//} = 2.38$ and $g_{\perp} = 1.90$, which is similar to, but distinct from the $S = 1/2$ diiron-mononitrosyl species observed in deflavo-FDP (Figrue 6.13 and 6.10). Double integrations of the EPR signal of reflavo-FDP(NO) against Cu^{II}EDTA standards indicate that the axial $g \sim 2$ signal represents .8 spin per diiron site. This deviation from stoichiometry is easily explained by the dissociation of NO as mentioned previously. As expected, the $g \sim 2$ EPR signal from the diiron-mononitrosyl complex disappears upon addition of 2 equiv NO, presumably due to oxidation of diiron center accompanied with N_2O production.

The 'dark' minus 'illuminated' difference spectra of reduced reflavo-FDP NO, ^{15}NO, and $^{15}N^{18}O$ adducts obtained at 10 K show the features nearly identical to those observed for the deflavo-FDP(NO) (Figure 6.13). The positive and negative bands at 1681 and 1869 cm^{-1} which downshifts to 1652 (-29) and 1837 (-32) cm^{-1} with ^{15}NO, readily assigned to ν(N-O) of reflavo-FDP(NO) complex and free NO molecules trapped within the protein pocket (Figure 6.14). As expected, the fermi-coupling also exits in reflavo-FDP(NO) and thus the ν(N-O) mode is best extracted from the $^{14}N^{16}O$ data.

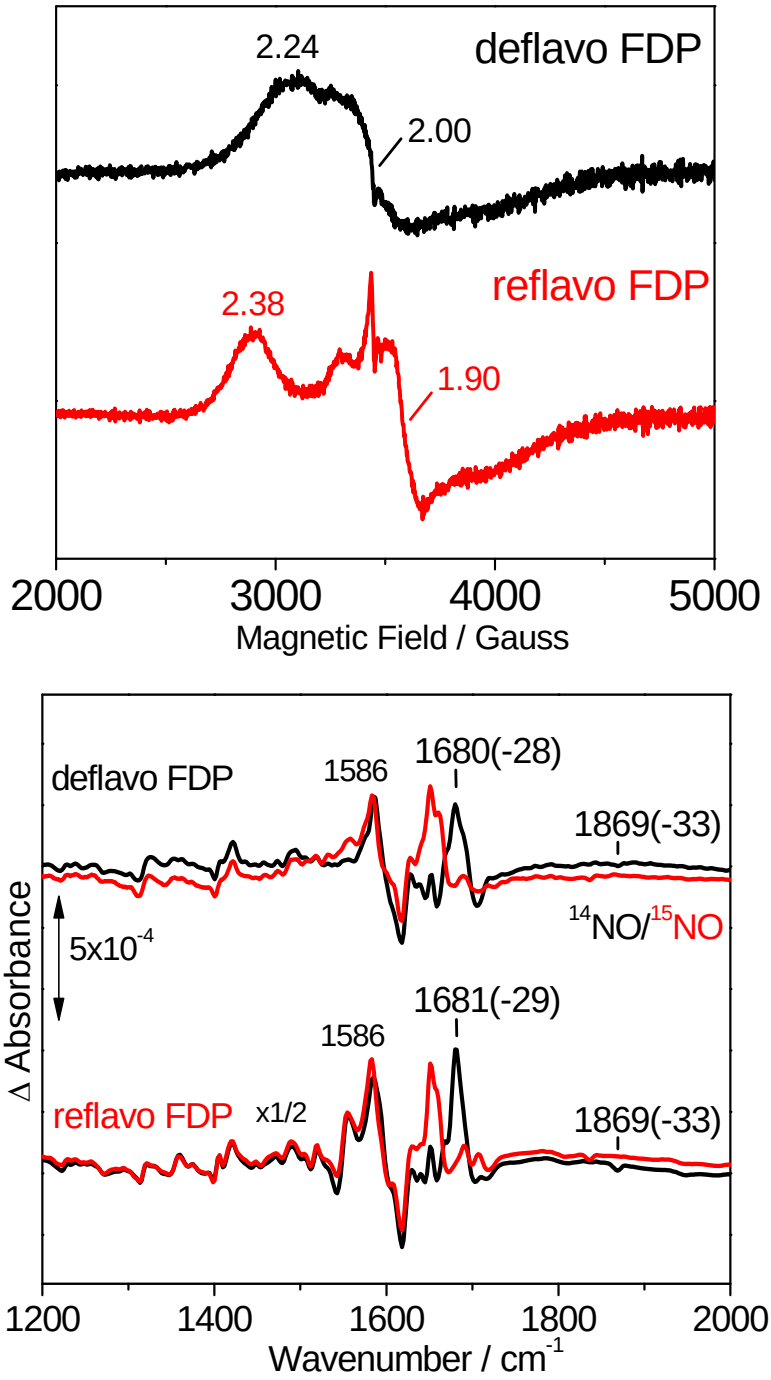

Figure 6.13 EPR spectra of 1 equiv NO adduct deflavo-FDP (black) and reflavo-FDP (red) at 4.2 K (Top). Conditions: protein concentration of 100 μM, 100 μM in 50 mM MOPS pH 7.4; microwave frequency, 9.66 GHz; microwave power, 2 mW; modulation amplitude, 10 G. FTIR 'dark' minus 'illuminated' difference spectra of deflavo-FDP(NO) (top) and reflavo-FDP(NO) (bottom) with NO (black) and ^{15}NO (red) obtained at 10 K (bottom).

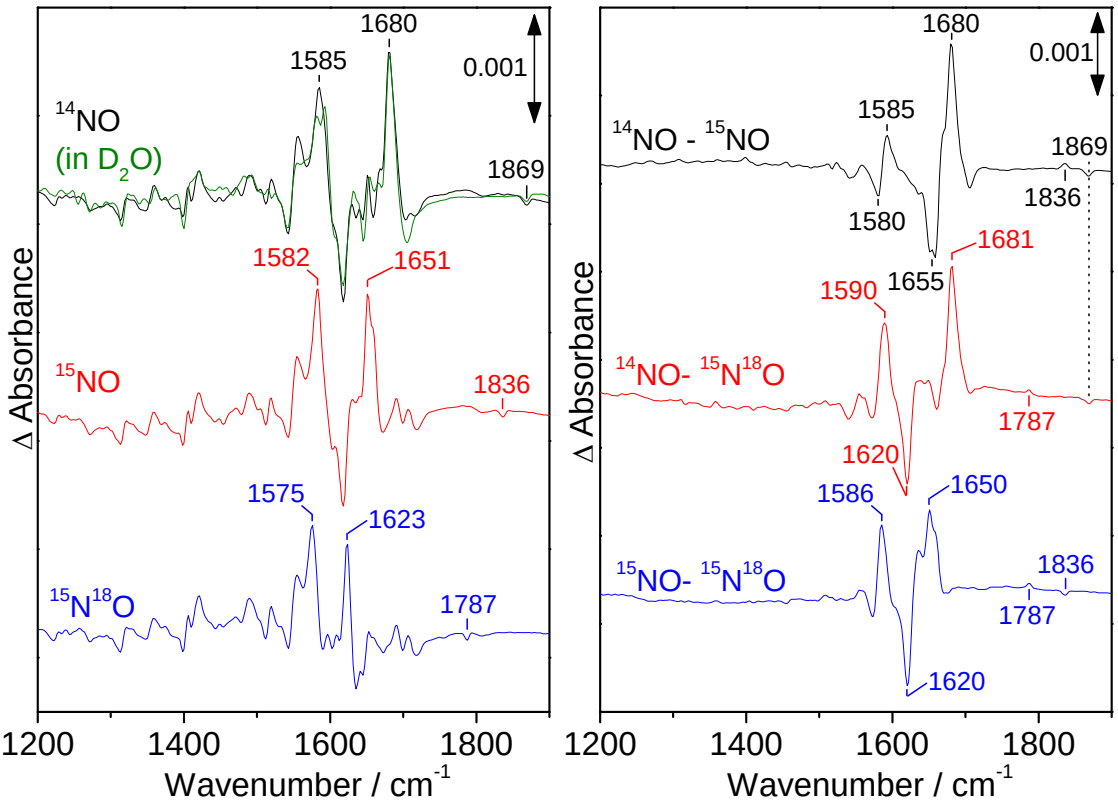

Figure 6.14 FTIR 'dark' minus 'illuminated' difference spectra of reflavo-FDP(NO) with NO (black), NO in D_2O (green), ^{15}NO (red), and $^{15}N^{18}O$ (blue) obtained at 10 K (left). Also shown are difference of 'dark' minus 'illuminated' FTIR difference spectra (right). 'NO' minus '^{15}NO' (black), 'NO' minus '$^{15}N^{18}O$', and '^{15}NO' minus '$^{15}N^{18}O$' difference spectra (blue).

6.10 Discussion

The heterologously expressed *Tm* FDP has full diiron site but only partial FMN occupancies. We found that the as-isolated protein has a high O_2R activity relative to NOR activity. The O_2R activity is consistent with its upregulation in *T. maritima* exposed to oxidative conditions (Le Fourn *et al.*, 2008). However, the relatively low NOR activity of the heterologously expressed *Tm* FDP is still significantly above background. Whether this NOR activity is physiologically relevant in *Thermotoga maritima* remains to be determined, but in other organism such as *E. coli*, *D. gigas,* and *D. vulgaris*, FDPs have been shown to confer both oxidative and nitrosative stress protection in vivo (Gardner *et al.*, 2002; Rodrigues *et al.*, 2006; Wildschut *et al.*, 2006).

In an attempt to distinguish between the two NOR mechanisms of FDPs (i.e., super-reduced and hyponitrite-intermediate mechanisms), we prepared *Tm* deflavo-FDP and characterized its reaction with NO. In agreement with the deposited X-ray crystal structure, the FMN cofactor can be removed from *Tm* FDP without irreversible disruption of the protein structure as well as the diiron site. As expected, the FMN-free FDP is catalytically inactive, but can be readily and quantitatively reconstituted with FMN.

Stoichiometric addition of NO to reduced deflavo-FDP results in the formation of a stable deflavo-FDP(NO) complex. The UV-vis absorption spectrum of this complex is characteristics of non-heme $\{FeNO\}^7$ complexes containing oxygen and nitrogen ligands. Further, the calculated extinction coefficient is in good agreement with values reported for other proteins and synthetic $\{FeNO\}^7$ complexes. Such $\{FeNO\}^7$ complexes are best described as $S = 3/2$ species characteristic EPR signals around $g \sim 4$ (Rodrigues *et al.*, 2006; Wildschut *et al.*, 2006). In the deflavo-FDP(NO) complex, antiferromagnetic coupling between the $\{FeNO\}^7$ $S = 3/2$ and the second iron(II) $S = 2$ produces an $S = 1/2$ $[Fe^{II} \bullet \{FeNO\}^7]$ species that exhibits a broad g ~ 2 signal, as previously observed in the NO adduct of hemerythrin (Nocek *et al.*, 1988). The double integration of this EPR signal suggests that the stoichiometric addition of NO nearly quantitatively converts the diiron(II) to $[Fe^{II} \bullet \{FeNO\}^7]$ sites. Most importantly, the same complex was also observed in reflavinated FDP, indicating that the formation of this complex is relevant to native system. To our knowledge this is the first example of a diferrous-mononitrosyl

complex formed in a diiron(II) protein or synthetic complex where the two metals share the same ligand sets.

The near-stoichiometric formation of the diferrous-mononitrosyl complex implies that, in both deflavo-FDP and reflavo-FDP, the first NO molecule binds with higher affinity than that of the second NO. This order of NO affinities seems in conflict with the cooperativity in NO binding inferred from the sigmoidal Michaelis-Menten plots for NOR activities of some other FDPs (Silaghi-Dumitrescu *et al.*, 2003; Silaghi-Dumitrescu *et al.*, 2005; Hillmann *et al.*, 2009). The relatively low NOR activity of flavinated *Tm* FDP may reflect a lack of cooperativity in NO binding. Relative NOR vs O_2R activities are also variable among FDPs for unknown reasons(Gardner *et al.*, 2002; Gomes *et al.*, 2002; Silaghi-Dumitrescu *et al.*, 2003; Saraiva *et al.*, 2004; Kurtz, 2007; Di Matteo *et al.*, 2008; Victor *et al.*, 2009).

Further addition of NO up to 2 equiv and beyond results in a change in the UV-vis absorption spectrum and the loss of the broad $g = 2$ EPR signal, consistent with NO reacting with the diferrous-mononitrosyl site. The product of this reaction is not homogenous: up to 70% of the diiron sites are catalytically competent and produce N_2O, as revealed by FTIR, while the remaining diiron sites form magnetically uncoupled $\{FeNO\}^7$ $S = 3/2$ species with characteristic $g \sim 4$ EPR signatures. Quantitative analyses of the UV-vis, FTIR, and EPR data all support these relative proportions for a given deflavo-FDP preparation, even though some variability in proportions of the two diiron products was observed from preparation to preparation.

The lack of magnetic coupling between the two $\{FeNO\}^7$ centers of deflavo-FDP$(NO)_2$ requires a major disruption of the efficient exchange coupling pathway provided by the oxo/hydroxo solvent bridge between the iron centers in the $[Fe^{III} \bullet Fe^{III}]$, mixed-valent $[Fe^{II} \bullet Fe^{III}]$ diiron sites, and in the diiron-mononitrosyl complex $[Fe^{II} \bullet \{FeNO\}^7]$ (Silaghi-Dumitrescu *et al.*, 2003; Vicente and Teixeira, 2005; Vicente *et al.*, 2009). Presumably, the solvent bridge is lost upon formation of the diferrous-dinitrosyl complex, but the bridging Asp carboxylate present in both reduced and oxidized FDP diiron sites may or may not remain in the diferrous-dinitrosyl complex. To our knowledge, there has been no report of synthetic analogs containing a carboxylate-bridged diiron site without at least one other supporting bridge. The only well-

characterized, carboxylate-bridged, non-heme, O/N-ligated diferrous-dinitrosyl synthetic complex, $Fe_2(NO)_2$(Et-HPTB)$(O_2CPh)(BF_4)_2$, includes an additional bridging alkoxo ligand (Feig *et al.*, 1996). This complex is EPR silent due to antiferromagnetic coupling between the two $\{FeNO\}^7$ centers. In the case of the diferrous-dinitrosyl adduct of ribonucleotide reductase R2 protein, the antiferromagnetic coupling between the two irons (and EPR silent character) may be due to the presence of both bidentate and monodentate carboxylate bridges, as observed in the diferrous R2 protein (Voegtli *et al.*, 2003). Dinuclear Mn^{II} sites in both proteins and synthetic complexes containing a bidentate carboxylate as the only bridging ligand have reportedly shown no evidence of magnetic exchange coupling (Samples *et al.*, 2005). A single bridging carboxylate with anti-syn configuration can accommodate metal-metal distance beyond 6.3 Å (Adams, 1995; Rodriguez-Martin, 2003), and the two $\{FeNO\}^7$ units could move further apart if the bridging carboxylate group adopt a non-bridging conformation. We view these data as evidence of conformational flexibility at the diiron site since uncoupling of the two irons at the active site is fully reversible and is not associated with iron loss. Indeed, the $[\{FeNO\}^7]_2$ species can be re-oxidized after exchanging the sample headspace, first with Ar then with O_2, re-reduced, and re-exposed to NO to regenerate the same fraction of $[\{FeNO\}^7]_2$ species, with no loss of iron (data not shown). Similarly, two consecutive redox-cyclings of deflavo-FDP$(NO)_2$ do not decrease the steady-state O_2R or NOR activity observed after FMN addition.

The vibrational characterization of the uncoupled $[\{FeNO\}^7]_2$ reveals a single set of Fe-N-O vibrations, suggesting that the individual $\{FeNO\}^7$ units adopt equivalent configurations. The Fe-N-O vibrations of deflavo-FDP$(NO)_2$ are similar to those observed previously in R2$(NO)_2$ (Lu *et al.*, 2004), which is not unexpected since the endogenous iron ligands are similar in both proteins. While the ν(Fe-NO) mode of deflavo-FDP(NO) is comparable to that of deflavo-FDP$(NO)_2$ (only ~8 cm^{-1} lower), the ν(N-O) mode is ~70 cm^{-1} lower than in the $[\{FeNO\}^7]_2$ complex. The observed ν(NO) mode is the lowest ν(NO) frequencies ever reported for of non-heme, non-sulfur $\{FeNO\}^7$ species repotted for proteins and model complexes (Table 6.1). One explanation for this exceptionally low ν(NO) frequency is that the Fe-N-O moiety interacts with the other iron center, leading to further reduction of nitrosyl to nitroxyl

anion. This result is reminiscent of the low ν(N-O) observed for Fe^{II}-bound $Fe_BMb(NO)$ (chapter 5). We viewed the low ν(N-O) as the heme-bound NO having more NO^- character due to electrostatic interaction with the Fe^{II} at the distal Fe_B site. Further, nitroxyl-like character of the mononitrosyl complex of FDPs is predicted by the computational calculation by Siegbahn et al. (Blomberg *et al.*, 2007).

The reactions of reduced deflavo-FDP with NO based on our results are summarized in Figure 6.15. Reduction of NO to N_2O by the reduced diiron site in the absence of FMN (pathway A in Figure 6.15), is consistent with the hyponitrite mechanism in Figure 6.2. While Figure 6.2, as suggested by the computational study by Siegbahn and coworkers (Blomberg *et al.*, 2007), indicates that the second NO reacts with the $\{FeNO\}^7$ species rather than the second iron(II), a magnetically coupled diferrous-dinitrosyl could be a transient intermediate in pathway A and in the hyponitrite mechanism. Thus, super-reduction of $\{FeNO\}^7$ units to nitroxyl $\{FeN(H)O\}^8$ species does not represent an absolute requisite step in the NOR reaction pathway in FDPs. The parallel pathway B in Scheme 3 leading to a stable magnetically uncoupled diferrous-dinitrosyl may be prevented in the flavinated enzyme via steric constraints. Alternatively, turnover of an $[\{FeNO\}^7]_2$ complex in FDP may require reduction by the proximal FMN cofactor, as proposed in the 'super-reduction' mechanism (Figure 6.2) (Silaghi-Dumitrescu *et al.*, 2005; Kurtz, 2007). Uncoupling of the two $\{FeNO\}^7$ units may also permit a reaction pathway in the flavinated enzyme where each iron center functions independently to form mononuclear hyponitrite complexes, thereby maximizing scavenging efficiency under high NO stress conditions. The results of this study provide a clear framework for further investigation of this unique family of enzymes.

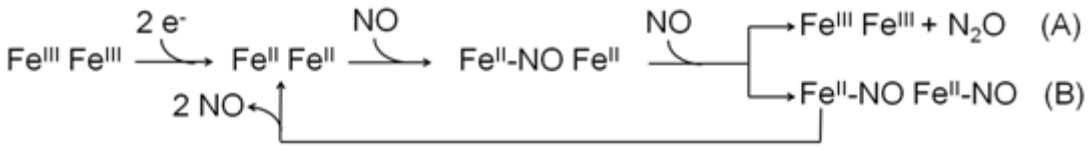

Figure 6.15 Schematic representations of the reaction of deflavo-FDP with NO based on our results.

CHAPTER 7
CONCLUSION AND FUTURE DIRECTIONS

7.1 The role of Cu_B in NO reduction by cytochrome *ba*$_3$ and *bo*$_3$

To investigate the possible involvement of a Cu-nitrosyl species during the NO reduction by HCOs, we studied ligand-dynamics in *ba*$_3$(NO), *bo*$_3$(NO), *ba*$_3$(CO)(NO), and *bo*$_3$(CO)(NO) using low-temperature photolysis experiments combined with UV-vis, EPR, FTIR, and RR spectroscopies. Interestingly, both *ba*$_3$ and *bo*$_3$ exhibit equivalent NO reduction turnover rates, and both fully-reduced enzymes bind a first NO molecule to form stable $S = 1/2$ 6cLS $\{FeNO\}^7$ species with similar spectroscopic features. However, cryogenic photolysis in *ba*$_3$(NO) generates a side-on Cu_B-NO complex, but in *bo*$_3$(NO), the photolyzed NO group is not capture by the Cu_B site. Furthermore, combined exposure of reduced *ba*$_3$ and *bo*$_3$ proteins to CO and NO resulted in the formation of a [heme-NO • OC-Cu_B] complex only in *bo*$_3$. We assigned these differences to a geometrical difference in the heme/copper center of *ba*$_3$ and *bo*$_3$. In *ba*$_3$, close vicinity between the heme *a*$_3$ and Cu_B ions allows transfer of the photolyzed NO, while a larger heme-copper distance permits concomitant binding of NO and CO in reduced *bo*$_3$. These results lead us to propose that the coordination of a second NO to Cu_B, after binding of a first NO to the heme iron, is not an essential step of the NO reduction reaction in these enzymes (Hayashi *et al.*, 2007; Hayashi *et al.*, 2009). Our preferred reaction mechanism is that the two electron reduction of NO to N_2O by *ba*$_3$ and *bo*$_3$ proceeds via the *cis*-heme mechanism (Figure 1.4).

7.2 NO activation mechanisms in the heme/non-heme diiron site of Fe_BMb

The reactivity of NO with Fe_BMb, a bioengineered model of the dinuclear active site of NORs, was examined with UV-vis, FTIR, EPR, RR, and FTIR spectroscopies. We have shown that 1 equiv NO addition to fully reduced Fe^{II}-Fe_BMb results in the formation of a 6cLS $\{FeNO\}^7$ complex that exhibits an exceptionally low NO stretching frequency which we assign to electrostatic interactions of the bound NO group with the distal non-heme Fe_B center. This low ν(NO) frequency suggests the heme-bound NO having an NO^- character, which could provide a nucleophile for N-N bond formation. Unexpectedly, this

complex reacts further with NO to produce a stable [5cLS heme-NO • ON-Fe_B] *trans*-dinitrosyl complex. The stability of this complex is consistent with the absence of N_2O production and we identify this species as a dead-end product. Despite this apparently negative outcome, a recent crystal structure of the cytochrome-*c*-dependent NOR from *Pseudomonas aeruginosa* (Hino *et al.*, 2010) reveals a heme/non-heme diiron center nearly identical to that of Fe_BMb (Figure 7.1). The reasons for this striking difference in reactivity towards NO of seemingly similar heme/non-heme diiron sites are yet to be elucidated. One possible explanation is that the 5cLS heme-NO is less reactive toward the second NO than a 6cLS heme-NO species due to the decreased nucleophilicity of heme-bound NO for 5cLS species compared to that of 6cLS (Praneeth *et al.*, 2006).

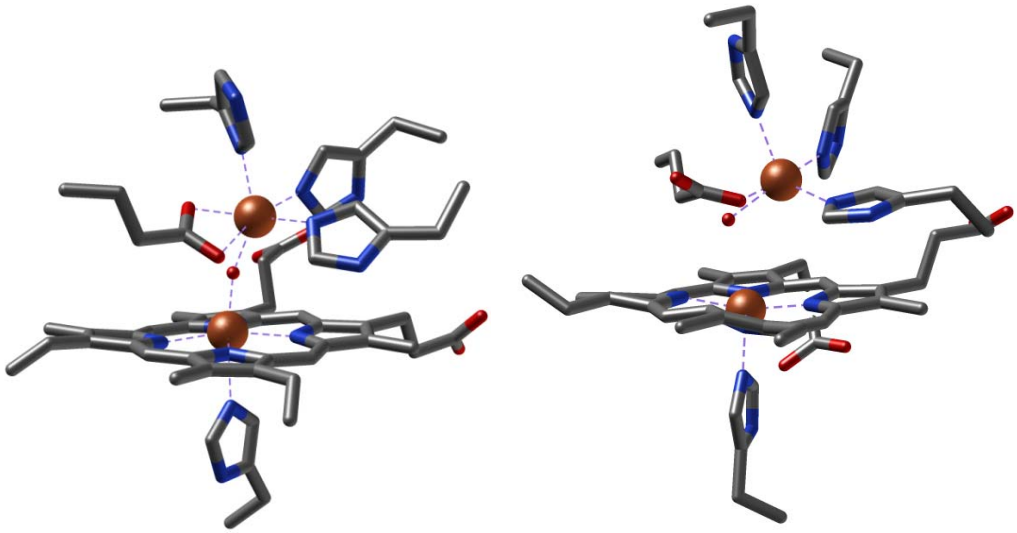

Figure 7.1 Heme/non-heme diiron active site of NOR from *Pseudomonas aeruginosa* (left) and of Fe_BMb (right) (PDB ID: 3O0R and 3M39).

Recently, Lu and coworkers have reported other active site models of NORs; I107E Fe_BMb (swMb L29H/F43H/V68E/I107E) (Lin *et al.*, 2010) and Fe_BMb(-His) (swMb L29H/F43H) (Lin *et al.*, 2010). Studying these NOR active site models would expand our knowledge in structure-reactivity relationship of heme/non-heme dinuclear iron center of NORs.

7.3 The roles of diiron center and FMN cofactor in the NO reduction by FDPs

In order to test the 'super-reduced' and 'hyponitrite-intermediate' mechanisms in

FDPs (Figure 6.2), we examined the reactivity of the FMN-free FDP enzyme from *Thermotoga maritima* towards NO using UV-vis, EPR, RR, and FTIR spectroscopies. Addition of up to 1 equiv NO to deflavo-FDP and reflavo-FDP results in formation of a stable $S = 1/2$ [Fe^{II} • $\{FeNO\}^7$] complex that exhibits an exceptionally low NO stretching frequency. As with $Fe_BMb(NO)$, we assign this low ν(N-O) to an NO^- character stabilized by electrostatic interaction with the non-coordinating Fe^{II} ion at the diiron site. Further addition of NO to the deflavo-FDP mononitrosyl complex results in two reaction pathways: one of which produces N_2O and the diferric center, and another which produces a stable diiron-dinitrosyl complex. The production of N_2O by deflavo-FDP supports the hyponitrite mechanism, whereas the concomitant formation of a stable diiron-dinitrosyl complex in the deflavo-FDP is suggestive of an inactive protein fraction, or of super-reduction pathway in the flavinated enzyme. However, since the reaction of four-electron reduced reflavo-FDP with excess NO results in the production of ~2 equiv of N_2O, the super-reduction of $\{FeNO\}^7$ units to nitroxyl $\{FeN(H)O\}^8$ species does not represent an absolute step in the reaction pathway. In conclusion, our data support the hyponitrite mechanism for NO reduction in FDPs with FMN's role limited to electron transfer to the diiron site and to prevent accumulation of uncoupled diiron-dinitrosyl complexes.

7.4 Future Direction

Characterization of mononitrosyl species in bacterial NORs and other FDPs

Reactivity of bacterial NORs and FDPs with NO has been investigated for years, however there are no published reports on monitoring the reaction of these enzymes with 1 equiv NO. We have shown in this thesis that either addition of 1 equiv NO or addition of slight excess NO in the presence of excess reducing agents results in the formation of stable mononitrosyl species in heme/copper center of ba_3 and bo_3, heme/non-heme center of Fe_BMb, and at the diiron center of FDP. The accumulation of such mononitrosyl species implies that the first NO molecule binds at the active site with significantly higher affinity than the second NO (Figure 7.2).

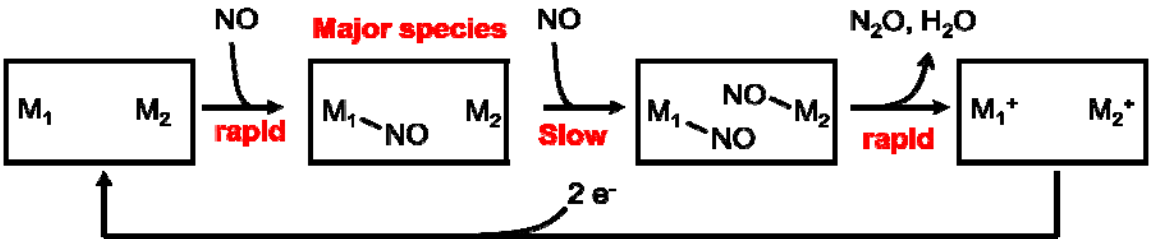

Figure 7.2 The reaction of dinuclear centers of 'slow NO reductases' with NO.

Steady-state kinetic analyses of NO reductase enzymes with high turnover rate show sigmoidal Michaelis-Menten plots that have been modeled by NO binding cooperativity (Girsch and de Vries, 1997; Silaghi-Dumitrescu *et al.*, 2003; Silaghi-Dumitrescu *et al.*, 2005). We will try to prepare mononitrosyl species in bacterial NORs and FDPs by addition of 1 equiv NO. If such complexes form in bacterial NORs and FDPs, we will define their vibrational signatures and correlate with the activity.

Detailed characterization of the reaction of Fe^{II}-Fe_BMb with NO and optimization of NO reaction conditions

In chapter 5, we have shown that further addition of NO to the 6cLS heme-NO species of Fe^{II}-Fe_BMb results in formation of a stable [5cLS heme-NO • ON-Fe_B] *trans*-dinitrosyl complex. We will define the detailed mechanisms of the conversion of 6cLS to 5cLS heme-NO species using stopped-flow and rapid freeze quench techniques. The alternative mechanisms include formation of either a [6cLS heme-NO • ON-Fe_B] *trans*-dinitrosyl complex or a [5cLS heme-NO • Fe_B] as a transient species (Figure 5.11). Definition of the reaction mechanisms allow us to propose chemical behaviors of NO in the heme/non-heme center of NORs, where the [5cLS heme-NO • ON-Fe_B] *trans*-dinitrosyl complex was observed as a millisecond intermediate (Kumita *et al.*, 2004).

Characterization of reaction intermediate species during NO reduction by FDPs

In previous chapter, we concluded that the NO reduction mechanism of FDPs is more consistent with the hyponitrite mechanism (Figure 6.2). However, our results did not show any evidence for the formation of a diferric-hyponitrite species as a reaction intermediate. In order to fully understand the catalytic mechanisms of FDPs, we will

characterize reaction intermediates of the reaction of diiron-mononitrosyl species with the second NO molecule using stopped-flow and rapid freeze quench techniques combined with EPR, FTIR, and RR spectroscopies. The expected intermediate species are a diferric-hyponitrite intermediate and a magnetically coupled diiron-dinitrosyl complex (Figure 7.3). Although these species are expected to be EPR silent, they can be differentiated by RR and FTIR spectroscopies. The diiron-hyponitrite is expected to exhibit ν(N-N) and ν(N-O) at ~1300 and 1100 cm^{-1} (Andrews and Liang, 2001; Varotsis *et al.*, 2007), respectively, whereas the magnetically coupled diiron-dinitrosyl complex is expected to exhibits a single ν(N-O) at ~1750 cm^{-1} due to the symmetric nature of complex (Lu *et al.*, 2004; Hayashi *et al.*, 2010).

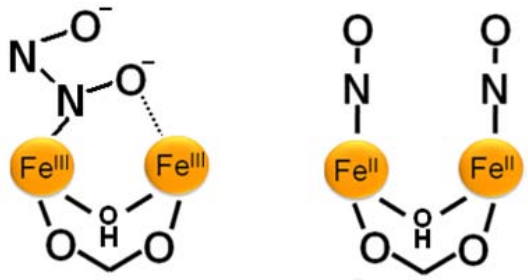

Figure 7.3 Schematic representations of possible intermediate species in the reaction of the diiron-mononitrosyl complex with the second NO; diiron-hyponitrite (left) and diiron-dinitrosyl (right).

Nitroxyl chemistry in dinuclear metalloproteins

Nitroxyl (HNO) is the one electron reduced form of NO, and is short-lived species in aqueous solution due to near diffusion-controlled dimerization (k = 8 x 10^6 $M^{-1}•s^{-1}$) (Shafirovich and Lymar, 2002). The involvement of a heme-nitroxyl species during the NO reduction have been proposed for both heme-based and non-heme iron based NO reductases (Blomberg *et al.*, 2006; Blomberg *et al.*, 2007). Further, a heme-nitroxyl intermediate has been spectroscopically characterized during turnover of the fungal NO reductase $P450_{nor}$ (Shiro *et al.*, 1995). We will characterize the reaction of HNO with NORs and FDPs using RR and FTIR spectroscopies. Further the reactivity of HNO complexes formed in those NO reductase enzymes will be studied.

So far we have carried out extensive characterization of the Mb-HNO $\{FeHNO^8\}$ complex, which can be generated by either one electron reduction of Mb(NO) $\{FeNO\}^7$

or addition of HNO donors to deoxy Mb (Sulc *et al.*, 2004; Immoos *et al.*, 2005). The FTIR difference spectra of Mb-HNO exhibit a positive band at 1380 cm^{-1}, which downshifts to 1357 and 1326 cm^{-1} with ^{15}NO and $^{15}N^{18}O$, assigned to ν(NO) of Mb-HNO (Figure 7.4) (Immoos *et al.*, 2005). The spectra also reveal two negative bands at 1546 and 2733 cm^{-1}, which downshifts to 1532 and 2728 cm^{-1} with ^{15}NO and to 1511 and 2727 cm^{-1} with $^{15}N^{18}O$, respectively (Figure 7.4). Based calculated shifts by DFT, diatomic oscillation, and sensitivity to H/D exchange (Linder and Rodgers, 2005), these bands are assigned to ν(NO) and ν(NH) of free HNO docked in a proteinaceous pocket. Further, RR spectra of Mb-HNO exhibit a H/D sensitive modes at 647 cm^{-1} which downshift to 611 cm^{-1} upon H/D exchange, readily assigned to ν(Fe-(H)N) (Figure 7.5).

We will monitor the reactivity of HNO with NORs and FDPs using RR and FTIR spectroscopies. Such studies would allow us to characterize reaction intermediate during the catalytic cycle of these enzymes.

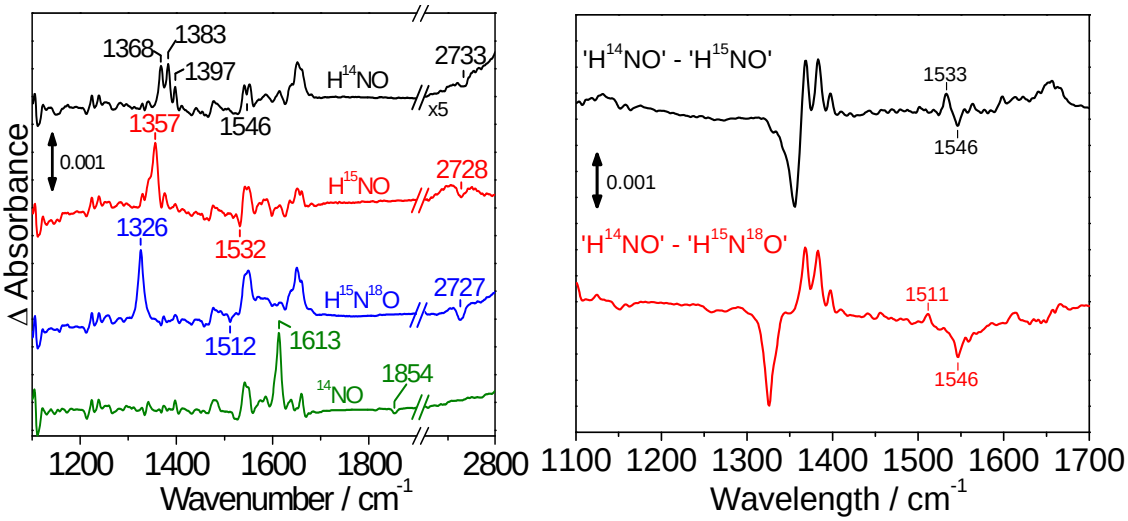

Figure 7.4 FTIR 'dark' minus 'illuminated' difference spectra of Mb-HNO (NO; black, ^{15}NO; red, $^{15}N^{18}O$; blue) and Mb(NO) (green) complex at 30 K (left). Difference of 'dark' minus 'illuminated' FTIR difference spectra obtained at 30 K (right). Top traces: Mb-HNO minus Mb-$H^{15}NO$ difference spectra (black) and the Mb-HNO minus Mb-$H^{15}N^{18}O$ difference spectra (red).

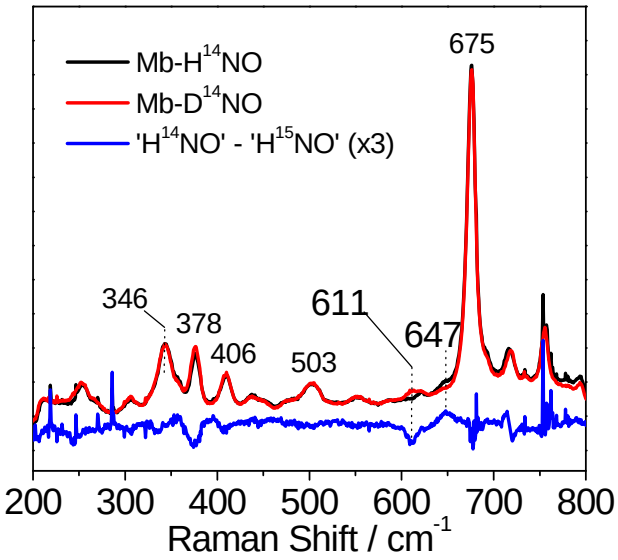

Figure 7.5 Low frequency RR spectra of Mb-HNO and Mb-DNO obtained with 413-nm excitation at room temperatures.

LITERATURE CITED

Abramson, J., Riistama, S., Larsson, G., Jasaitis, A., Svensson-Ek, M., Laakkonen, L., Puustinen, A., Iwata, S. and Wikstrom, M. (2000) The structure of the ubiquinol oxidase from *Escherichia coli* and its ubiquinone binding site. *Nat. Struct. Biol.* **7**: 910-917.

Adams, H., Bailey, N.A., Debaecher, N., Fenton, D.E., Kanda, W., Latour, J.-M., Okawa, H., and Sakiyama, H. (1995) A dinuclear (μ-carboxylato)manganese(II) complex derived from a macrocyclic ligand; a structural model for active site in natural systems. *Angew. Chem. Int. Ed. Engl.* **34**: 2535-2537.

Alben, J. O., Moh, P. P., Fiamingo, F. G. and Altschuld, R. A. (1981) Cytochrome oxidase a_3 heme and copper observed by low-temperature Fourier transform infrared spectroscopy of the CO complex. *Proc. Natl. Acad. Sci. U. S. A.* **78**: 234-237.

Alderton, W. K., Cooper, C. E. and Knowles, R. G. (2001) Nitric oxide synthases: structure, function and inhibition. *Biochem. J.* **357**: 593-615.

Andrew, C. R., Green, E. L., Lawson, D. M. and Eady, R. R. (2001) Resonance Raman studies of cytochrome *c′* support the binding of NO and CO to opposite sides of the heme: implications for ligand discrimination in heme-based sensors. *Biochemistry* **40**: 4115-4122.

Andrews, L. and Liang, B. (2001) Infrared spectrum of the hyponitrite dianion, $N_2O_2^{2-}$, isolated and insulated from stabilizing metal cations in solid argon. *J. Am. Chem. Soc.* **123**: 1997-2002.

Anjum, M. F., Stevanin, T. M., Read, R. C. and Moir, J. W. (2002) Nitric oxide metabolism in *Neisseria meningitidis*. *J. Bacteriol.* **184**: 2987-2993.

Antonyuk, S. V., Strange, R. W., Sawers, G., Eady, R. R. and Hasnain, S. S. (2005) Atomic resolution structures of resting-state, substrate- and product-complexed Cu-nitrite reductase provide insight into catalytic mechanism. *Proc. Natl. Acad. Sci. U.S.A.* **102**: 12041-12046.

Arciero, D. M. and Lipscomb, J. D. (1986) Binding of ^{17}O-labeled substrate and inhibitors to protocatechuate 4,5-dioxygenase-nitrosyl complex. Evidence for direct substrate binding to the active site Fe^{2+} of extradiol dioxygenases. *J. Biol. Chem.* **261**: 2170-2178.

Averill, B. A. (1996) Dissimilatory nitrite and nitric oxide reductases. *Chem. Rev.* **96**: 2951-2965.

Baenziger, J. E., Miller, K. W. and Rothschild, K. J. (1993) Fourier transform infrared difference spectroscopy of the nicotinic acetylcholine receptor: evidence for specific protein structural changes upon desensitization. *Biochemistry* **32**: 5448-5454.

Barman, B. G. and Tollin, G. (1972) Flavine-protein interactions in flavoenzymes. Thermodynamics and kinetics of reduction of *Azotobacter flavodoxin*. *Biochemistry* **11**: 4755-4759.

Beckman, J. S. and Koppenol, W. H. (1996) Nitric oxide, superoxide, and peroxynitrite: the good, the bad, and ugly. *Am. J. Physiol.* **271**: C1424-1437.

Benko, B. and Yu, N. T. (1983) Resonance Raman studies of nitric oxide binding to ferric and ferrous hemoproteins: detection of Fe(III)-NO stretching, Fe(III)-N-O bending, and Fe(II)-N-O bending vibrations. *Proc. Natl. Acad. Sci. U. S. A.* **80**: 7042-7046.

Blackmore, R. S., Greenwood, C. and Gibson, Q. H. (1991) Studies of the primary oxygen intermediate in the reaction of fully reduced cytochrome oxidase. *J. Biol. Chem.* **266**: 19245-19249.

Blokzijl-Homan, M. F. and van Gelder, B. F. (1971) Biochemical and biophysical studies on cytochrome aa_3. 3. The EPR spectrum of NO-ferrocytochrome a_3. *Biochim. Biophys. Acta* **234**: 493-498.

Blomberg, L. M., Blomberg, M. R. and Siegbahn, P. E. (2006) Reduction of nitric oxide in bacterial nitric oxide reductase–a theoretical model study. *Biochim. Biophys. Acta* **1757**: 240-252.

Blomberg, L. M., Blomberg, M. R. and Siegbahn, P. E. (2007) Theoretical study of the reduction of nitric oxide in an A-type flavoprotein. *J. Biol. Inorg. Chem.* **12**: 79-89.

Blomberg, L. M., Blomberg, M. R. and Siegbahn, P. E. (2006) A theoretical study on nitric oxide reductase activity in a ba_3-type heme-copper oxidase. *Biochim. Biophys. Acta* **1757**: 31-46.

Boelens, R., Rademaker, H., Pel, R. and Wever, R. (1982) EPR studies of the photodissociation reactions of cytochrome *c* oxidase-nitric oxide complexes. *Biochim. Biophys. Acta* **679**: 84-94.

Bou-Abdallah, F. and Chasteen, N. D. (2008) Spin concentration measurements of high-spin ($g' = 4.3$) rhombic iron(III) ions in biological samples: theory and application. *J. Biol. Inorg. Chem.* **13**: 15-24.

Brown, C. A., Pavlosky, M. A., Westre, T. E., Zhang, Y., Hedman, B., Hodgson, K. O. and Solomon, E. I. (1995) Spectroscopic and theoretical description of the electronic structure of $S = 3/2$ iron-nitrosyl complexes and their relation to O_2 activation by nonheme iron enzyme active sites. *J. Am. Chem. Soc.* **117**: 715-732.

Brudvig, G. W., Stevens, T. H. and Chan, S. I. (1980) Reactions of nitric oxide with cytochrome *c* oxidase. *Biochemistry* **19**: 5275-5285.

Brunori, M., Forte, E., Arese, M., Mastronicola, D., Giuffre, A. and Sarti, P. (2006) Nitric oxide and the respiratory enzyme. *Biochim. Biophys. Acta* **1757**: 1144-1154.

Buschmann, S., Warkentin, E., Xie, H., Langer, J. D., Ermler, U. and Michel, H. (2010) The structure of cbb_3 cytochrome oxidase provides insights into proton pumping. *Science* **329**: 327-330.

Butland, G., Spiro, S., Watmough, N. J. and Richardson, D. J. (2001) Two conserved glutamates in the bacterial nitric oxide reductase are essential for activity but not assembly of the enzyme. *J. Bacteriol.* **183**: 189-199.

Butler, C., Forte, E., Maria Scandurra, F., Arese, M., Giuffre, A., Greenwood, C. and Sarti, P. (2002) Cytochrome bo_3 from *Escherichia coli*: the binding and turnover of nitric oxide. *Biochem. Biophys. Res. Commun.* **296**: 1272-1278.

Butler, C. S., Seward, H. E., Greenwood, C. and Thomson, A. J. (1997) Fast cytochrome *bo* from *Escherichia coli* binds two molecules of nitric oxide at Cu_B. *Biochemistry* **36**: 16259-19266.

Calhoun, M. W., Lemieux, L. J., Thomas, J. W., Hill, J. J., Goswitz, V. C., Alben, J. O. and Gennis, R. B. (1993) Spectroscopic characterization of mutants supports the assignment of histidine-419 as the axial ligand of heme *o* in the binuclear center of the cytochrome *bo* ubiquinol oxidase from *Escherichia coli*. *Biochemistry* **32**: 13254-13261.

Carey, P. R. (1982) Biochemical Applications of Raman and Resonance Raman Spectroscopies. *Molecular Biology series, Academic Press* 71-153.

Chakravortty, D. and Hensel, M. (2003) Inducible nitric oxide synthase and control of intracellular bacterial pathogens. *Microbes. Infect.* **5**: 621-627.

Cheesman, M. R., Watmough, N. J., Pires, C. A., Turner, R., Brittain, T., Gennis, R. B., Greenwood, C. and Thomson, A. J. (1993) Cytochrome *bo* from *Escherichia coli*: identification of haem ligands and reaction of the reduced enzyme with carbon monoxide. *Biochem. J.* **289**: 709-718.

Chen, L., Liu, M. Y., Legall, J., Fareleira, P., Santos, H. and Xavier, A. V. (1993) Purification and characterization of an NADH-rubredoxin oxidoreductase involved in the utilization of oxygen by *Desulfovibrio gigas*. *Eur. J. Biochem.* **216**: 443-448.

Chen, Y., Hunsicker-Wang, L., Pacoma, R. L., Luna, E. and Fee, J. A. (2005) A homologous expression system for obtaining engineered cytochrome ba_3 from *Thermus thermophilus* HB8. *Protein Expr. Purif.* **40**: 299-318.

Cheng, L., Novozhilova, I., Kim, C., Kovalevsky, A., Bagley, K. A., Coppens, P. and Richter-Addo, G. B. (2000) First observation of photoinduced nitrosyl linkage isomers of iron nitrosyl porphyrins. *J. Am. Chem. Soc.* **122**: 7142-7143.

Chu, K., Vojtchovsky, J., McMahon, B. H., Sweet, R. M., Berendzen, J. and Schlichting, I. (2000) Structure of a ligand-binding intermediate in wild-type carbonmonoxy myoglobin. *Nature* **403**: 921-923.

Clay, M. D., Cosper, C. A., Jenney, F. E., Jr., Adams, M. W. and Johnson, M. K. (2003) Nitric oxide binding at the mononuclear active site of reduced *Pyrococcus furiosus* superoxide reductase. *Proc. Natl. Acad. Sci. U. S. A.* **100**: 3796-3801.

Coletta, M., Boffi, A., Ascenzi, P., Brunori, M. and Chiancone, E. (1990) A novel mechanism of heme-heme interaction in the homodimeric hemoglobin from *Scapharca inaequivalvis* as manifested upon cleavage of the proximal Fe-N epsilon bond at low pH. *J. Biol. Chem.* **265**: 4828-4830.

Collman, J. P., Dey, A., Yang, Y., Decreau, R. A., Ohta, T. and Solomon, E. I. (2008) Intermediates involved in the two electron reduction of NO to N_2O by a functional synthetic model of heme containing bacterial NO reductase. *J. Am. Chem. Soc.* **130**: 16498-16499.

Coppens, P., Novozhilova, I. and Kovalevsky, A. (2002) Photoinduced linkage isomers of transition-metal nitrosyl compounds and related complexes. *Chem. Rev.* **102**: 861-883.

Costas, M., Cady, C. W., Kryatov, S. V., Ray, M., Ryan, M. J., Rybak-Akimova, E. V. and Que, L., Jr. (2003) Role of Carboxylate Bridges in Modulating Nonheme Diiron(II)/O_2 Reactivity. *Inorg. Chem.* **42**: 7519-7530.

Coufal, D. E., Tavares, P., Pereira, A. S., Hyunh, B. H. and Lippard, S. J. (1999) Reactions of nitric oxide with the reduced non-heme diiron center of the soluble methane monooxygenase hydroxylase. *Biochemistry* **38**: 4504-4513.

Coyle, C. M., Vogel, K. M., Rush, T. S., 3rd, Kozlowski, P. M., Williams, R., Spiro, T. G., Dou, Y., Ikeda-Saito, M., Olson, J. S. and Zgierski, M. Z. (2003) FeNO structure in distal pocket mutants of myoglobin based on resonance Raman spectroscopy. *Biochemistry* **42**: 4896-4903.

Cruz-Ramos, H., Crack, J., Wu, G., Hughes, M. N., Scott, C., Thomson, A. J., Green, J. and Poole, R. K. (2002) NO sensing by FNR: regulation of the *Escherichia coli* NO-detoxifying flavohaemoglobin, Hmp. *EMBO J.* **21**: 3235-3244.

D'Autreaux, B., Horner, O., Oddou, J. L., Jeandey, C., Gambarelli, S., Berthomieu, C., Latour, J. M. and Michaud-Soret, I. (2004) Spectroscopic description of the two nitrosyl-

iron complexes responsible for fur inhibition by nitric oxide. *J. Am. Chem. Soc.* **126**: 6005-6016.

Das, T. K., Pecoraro, C., Tomson, F. L., Gennis, R. B. and Rousseau, D. L. (1998) The post-translational modification in cytochrome *c* oxidase is required to establish a functional environment of the catalytic site. *Biochemistry* **37**: 14471-14476.

Decatur, S. M., Franzen, S., DePillis, G. D., Dyer, R. B., Woodruff, W. H. and Boxer, S. G. (1996) Trans effects in nitric oxide binding to myoglobin cavity mutant H93G. *Biochemistry* **35**: 4939-4944.

Deinum, G., Stone, J. R., Babcock, G. T. and Marletta, M. A. (1996) Binding of nitric oxide and carbon monoxide to soluble guanylate cyclase as observed with Resonance raman spectroscopy. *Biochemistry* **35**: 1540-1547.

Di Matteo, A., Scandurra, F. M., Testa, F., Forte, E., Sarti, P., Brunori, M. and Giuffre, A. (2008) The O_2-scavenging flavodiiron protein in the human parasite *Giardia intestinalis*. *J. Biol. Chem.* **283**: 4061-4068.

Ding, X. D., Weichsel, A., Andersen, J. F., Shokhireva, T. K., Balfour, C., Pierik, A. J., Averill, B. A., Montfort, W. R. and Walker, F. A. (1999) Nitric oxide binding to the ferri- and ferroheme states of nitrophorin 1, a reversible NO-binding heme protein from the saliva of the blood-sucking insect, *Rhodnius prolixus*. *J. Am. Chem. Soc.* **121**: 128-138.

Einarsdottir, O., Killough, P. M., Fee, J. A. and Woodruff, W. H. (1989) An infrared study of the binding and photodissociation of carbon monoxide in cytochrome ba_3 from *Thermus thermophilus*. *J. Biol. Chem.* **264**: 2405-2408.

Enemark, J. H. and Feltham, R. D. (1974) Principles of structure, bonding, and reactivity for metal nitrosyl complexes. *Coord. Chem. Rev.* **13**: 339-406.

Feig, A. L., Bautista, M. T. and Lippard, S. J. (1996) A Carboxylate-Bridged Non-Heme Diiron Dinitrosyl Complex. *Inorg. Chem.* **35**: 6892-6898.

Findsen, E. W., Centeno, J., Babcock, G. T. and Ondrias, M. R. (1987) Cytochrome a_3 hemepocket relaxation susequent to ligand photolysis from cytochrome oxidase. *J. Am. Chem. Soc.* **109**: 5367-5372.

Fomitchev, D. V. and Coppens, P. (1996) X-ray Diffraction Analysis of Geometry Changes upon Excitation: The Ground-State and Metastable-State Structures of $K_2[Ru(NO_2)_4(OH)(NO)]$. *Inorg. Chem.* **35**: 7021-7026.

Fomitchev, D. V., Coppens, P., Li, T. S., Bagley, K. A., Chen, L. and Richter-Addo, G. B. (1999) Photo-induced metastable linkage isomers of ruthenium nitrosyl porphyrins. *J. Chem. Soc., Chem. Commun.* 2013-2014.

Frazao, C., Silva, G., Gomes, C. M., Matias, P., Coelho, R., Sieker, L., Macedo, S., Liu, M. Y., Oliveira, S., Teixeira, M., Xavier, A. V., Rodrigues-Pousada, C., Carrondo, M. A. and Le Gall, J. (2000) Structure of a dioxygen reduction enzyme from *Desulfovibrio gigas*. *Nat. Struct. Biol.* **7**: 1041-1045.

Fujiwara, T. and Fukumori, Y. (1996) Cytochrome *cb*-type nitric oxide reductase with cytochrome *c* oxidase activity from *Paracoccus denitrificans* ATCC 35512. *J. Bacteriol.* **178**: 1866-1871.

Gardner, A. M. and Gardner, P. R. (2002) Flavohemoglobin detoxifies nitric oxide in aerobic, but not anaerobic, *Escherichia coli*. Evidence for a novel inducible anaerobic nitric oxide-scavenging activity. *J. Biol. Chem.* **277**: 8166-8171.

Gardner, A. M., Helmick, R. A. and Gardner, P. R. (2002) Flavorubredoxin, an inducible catalyst for nitric oxide reduction and detoxification in *Escherichia coli*. *J. Biol. Chem.* **277**: 8172-8177.

Gardner, P. R., Gardner, A. M., Martin, L. A. and Salzman, A. L. (1998) Nitric oxide dioxygenase: an enzymic function for flavohemoglobin. *Proc. Natl. Acad. Sci. U. S. A.* **95**: 10378-10383.

Gerscher, S., Hildebrandt, P., Buse, G. and Soulimane, T. (1999) The active site structure of ba_3 oxidase from *Thermus thermophilus* studied by resonance raman spectroscopy. *Biospectroscopy* **5**: S53-63.

Girsch, P. and de Vries, S. (1997) Purification and initial kinetic and spectroscopic characterization of NO reductase from *Paracoccus denitrificans*. *Biochim. Biophys. Acta* **1318**: 202-216.

Giuffre, A., Stubauer, G., Sarti, P., Brunori, M., Zumft, W. G., Buse, G. and Soulimane, T. (1999) The heme-copper oxidases of *Thermus thermophilus* catalyze the reduction of nitric oxide: evolutionary implications. *Proc. Natl. Acad. Sci. U.S.A.* **96**: 14718-14723.

Goldstein, S. and Merenyi, G. (2008) The chemistry of peroxynitrite: implications for biological activity. *Methods Enzymol.* **436**: 49-61.

Gomes, C. M., Giuffre, A., Forte, E., Vicente, J. B., Saraiva, L. M., Brunori, M. and Teixeira, M. (2002) A novel type of nitric-oxide reductase *Escherichia coli* flavorubredoxin. *J. Biol. Chem.* **277**: 25273-25276.

Gomes, C. M., Silva, G., Oliveira, S., LeGall, J., Liu, M. Y., Xavier, A. V., Rodrigues-Pousada, C. and Teixeira, M. (1997) Studies on the redox centers of the terminal oxidase from *Desulfovibrio gigas* and evidence for its interaction with rubredoxin. *J. Biol. Chem.* **272**: 22502-22508.

Gomes, C. M., Vicente, J. B., Wasserfallen, A. and Teixeira, M. (2000) Spectroscopic studies and characterization of a novel electron-transfer chain from *Escherichia coli* involving a flavorubredoxin and its flavoprotein reductase partner. *Biochemistry* **39**: 16230-16237.

Gregoriou, V. G., Jayaraman, V., Hu, X. and Spiro, T. G. (1995) FT-IR difference spectroscopy of hemoglobins A and Kempsey: evidence that a key quaternary interaction induces protonation of Asp beta 99. *Biochemistry* **34**: 6876-6882.

Haskin, C. J., Ravi, N., Lynch, J. B., Münck, E. and Que, L., Jr. (1995) Reaction of NO with the reduced R2 protein of ribonucleotide reductase from *Escherichia coli*. *Biochemistry* **34**: 11090-110908.

Hassett, D. J., Cuppoletti, J., Trapnell, B., Lymar, S. V., Rowe, J. J., Yoon, S. S., Hilliard, G. M., Parvatiyar, K., Kamani, M. C., Wozniak, D. J., Hwang, S. H., McDermott, T. R. and Ochsner, U. A. (2002) Anaerobic metabolism and quorum sensing by Pseudomonas aeruginosa biofilms in chronically infected cystic fibrosis airways: rethinking antibiotic treatment strategies and drug targets. *Adv. Drug. Deliv. Rev.* **54**: 1425-1443.

Hayashi, T., Caranto, J. D., Wampler, D. A., Kurtz, D. M. and Moënne-Loccoz, P. (2010) Insights into the nitric oxide reductase mechanism of flavodiiron proteins from a flavin-free enzyme. *Biochemistry* **49**: 7040-7049.

Hayashi, T., Lin, I. J., Chen, Y., Fee, J. A. and Moënne-Loccoz, P. (2007) Fourier transform infrared characterization of a Cu_B-nitrosyl complex in cytochrome ba_3 from *Thermus thermophilus*: relevance to NO reductase activity in heme-copper terminal oxidases. *J. Am. Chem. Soc.* **129**: 14952-14958.

Hayashi, T., Lin, M. T., Ganesan, K., Chen, Y., Fee, J. A., Gennis, R. B. and Moënne-Loccoz, P. (2009) Accommodation of two diatomic molecules in cytochrome bo_3: insights into NO reductase activity in terminal oxidases. *Biochemistry* **48**: 883-890.

Hill, J., Goswitz, V. C., Calhoun, M., Garcia-Horsman, J. A., Lemieux, L., Alben, J. O. and Gennis, R. B. (1992) Demonstration by FTIR that the *bo*-type ubiquinol oxidase of *Escherichia coli* contains a heme-copper binuclear center similar to that in cytochrome *c* oxidase and that proper assembly of the binuclear center requires the cyoE gene product. *Biochemistry* **31**: 11435-11440.

Hille, R., Olson, J. S. and Palmer, G. (1979) Spectral transitions of nitrosyl hemes during ligand binding to hemoglobin. *J. Biol. Chem.* **254**: 12110-12120.

Hillmann, F., Riebe, O., Fischer, R. J., Mot, A., Caranto, J. D., Kurtz, D. M., Jr. and Bahl, H. (2009) Reductive dioxygen scavenging by flavo-diiron proteins of *Clostridium acetobutylicum*. *FEBS Lett.* **583**: 241-245.

Hino, T., Matsumoto, Y., Nagano, S., Sugimoto, H., Fukumori, Y., Murata, T., Iwata, S. and Shiro, Y. (2010) Structural Basis of Biological N_2O Generation by Bacterial Nitric Oxide Reductase. *Science* 1666-1670.

Householder, T. C., Fozo, E. M., Cardinale, J. A. and Clark, V. L. (2000) Gonococcal nitric oxide reductase is encoded by a single gene, norB, which is required for anaerobic growth and is induced by nitric oxide. *Infect. Immun.* **68**: 5241-5246.

Hunsicker-Wang, L. M., Pacoma, R. L., Chen, Y., Fee, J. A. and Stout, C. D. (2005) A novel cryoprotection scheme for enhancing the diffraction of crystals of recombinant cytochrome ba_3 oxidase from *Thermus thermophilus*. *Acta Crystallogr.* **D61**: 340-343.

Immoos, C. E., Sulc, F., Farmer, P. J., Czarnecki, K., Bocian, D. F., Levina, A., Aitken, J. B., Armstrong, R. S. and Lay, P. A. (2005) Bonding in HNO-myoglobin as characterized by X-ray absorption and resonance raman spectroscopies. *J. Am. Chem. Soc.* **127**: 814-815.

Iwata, S., Ostermeier, C., Ludwig, B. and Michel, H. (1995) Structure at 2.8 Å resolution of cytochrome *c* oxidase from *Paracoccus denitrificans*. *Nature* **376**: 660-669.

Jackson, T. A., Yikilmaz, E., Miller, A. F. and Brunold, T. C. (2003) Spectroscopic and computational study of a non-heme iron $[Fe\text{-}NO]^7$ system: exploring the geometric and electronic structures of the nitrosyl adduct of iron superoxide dismutase. *J. Am. Chem. Soc.* **125**: 8348-8363.

Jasinski, M. J., Hayton, J., Kadziola, Z., Wos, S. and Sosnowski, A. W. (2002) Hemodynamic performance after stented vs. stentless aortic valve replacement. *J. Cardiovasc. Surg. (Torino)* **43**: 313-317.

Keightley, J. A., Zimmermann, B. H., Mather, M. W., Springer, P., Pastuszyn, A., Lawrence, D. M. and Fee, J. A. (1995) Molecular genetic and protein chemical characterization of the cytochrome ba_3 from *Thermus thermophilus* HB8. *J. Biol. Chem.* **270**: 20345-20358.

Kumita, H., Matsuura, K., Hino, T., Takahashi, S., Hori, H., Fukumori, Y., Morishima, I. and Shiro, Y. (2004) NO reduction by nitric oxide reductase from denitrifying bacterium *Pseudomonas aeruginosa*: characterization of reaction intermediates that appear in the single turnover cycle. *J. Biol. Chem.* **279**: 55247-55254.

Kurtz, D. M. (2007) Flavo-diiron enzymes: Nitric oxide or dioxygen reductases? *Dalton Trans.* 4115-4121.

Le Fourn, C., Fardeau, M. L., Ollivier, B., Lojou, E. and Dolla, A. (2008) The hyperthermophilic anaerobe *Thermotoga Maritima* is able to cope with limited amount of oxygen: insights into its defence strategies. *Environ. Microbiol.* **10**: 1877-1887.

Lehnert, N., Sage, J. T., Silvernail, N., Scheidt, W. R., Alp, E. E., Sturhahn, W. and Zhao, J. (2010) Oriented single-crystal nuclear resonance vibrational spectroscopy of [Fe(TPP)(MI)(NO)]: quantitative assessment of the trans effect of NO. *Inorg. Chem.* **49**: 7197-7215.

Li, M., Bonnet, D., Bill, E., Neese, F., Weyhermuller, T., Blum, N., Sellmann, D. and Wieghardt, K. (2002) Tuning the electronic structure of octahedral iron complexes [FeL(X)] (L = 1-alkyl-4,7-bis(4-tert-butyl-2-mercaptobenzyl)-1,4,7-triazacyclononane, X = Cl, CH_3O, CN, NO). The S = 1/2 <=> 3/2 Spin equilibrium of [FeL(Pr)(NO)]. *Inorg. Chem.* **41**: 3444-34456.

Lin, R., Immoos, C. E. and Farmer, P. J. (2000) Unusual voltammetry of manganese-substituted myoglobin in surfactant film: evidence for two redox pathways. *J. Biol. Inorg. Chem.* **5**: 738-747.

Lin, Y. W., Yeung, N., Gao, Y. G., Miner, K. D., Lei, L., Robinson, H. and Lu, Y. (2010) Introducing a 2-His-1-Glu nonheme iron center into myoglobin confers nitric oxide reductase activity. *J. Am. Chem. Soc.* **132**: 9970-9972.

Lin, Y. W., Yeung, N., Gao, Y. G., Miner, K. D., Tian, S., Robinson, H. and Lu, Y. (2010) Roles of glutamates and metal ions in a rationally designed nitric oxide reductase based on myoglobin. *Proc. Natl. Acad. Sci. U. S. A.* **107**: 8581-8586.

Linder, D. P. and Rodgers, K. R. (2005) Structural, electronic, and vibrational characterization of Fe-HNO porphyrinates by density functional theory. *Inorg. Chem.* **44**: 8259-825964.

Lindqvist, Y., Huang, W., Schneider, G. and Shanklin, J. (1996) Crystal structure of Δ^9 stearoyl-acyl carrier protein desaturase from castor seed and its relationship to other di-iron proteins. *EMBO J.* **15**: 4081-4092.

Liu, B., Chen, Y., Doukov, T., Soltis, S. M., Stout, C. D. and Fee, J. A. (2009) Combined microspectrophotometric and crystallographic examination of chemically reduced and X-ray radiation-reduced forms of cytochrome ba_3 oxidase from *Thermus thermophilus*: structure of the reduced form of the enzyme. *Biochemistry* **48**: 820-826.

Lu, S., Libby, E., Saleh, L., Xing, G., Bollinger, J. M., Jr. and Moënne-Loccoz, P. (2004) Characterization of NO adducts of the diiron center in protein R2 of *Escherichia coli* ribonucleotide reductase and site-directed variants. Implications for the O_2-activation mechanism. *J. Biol. Inorg. Chem.* **9**: 818-827.

Lu, S., Suharti, de Vries, S. and Moënne-Loccoz, P. (2004) Two CO molecules can bind concomitantly at the diiron site of NO reductase from *Bacillus azotoformans*. *J. Am. Chem. Soc.* **126**: 15332-15333.

Marletta, M. A. and Spiering, M. M. (2003) Trace elements and nitric oxide function. *J. Nutr.* **133**: 1431S-1433S.

Mascarenhas, R., Wei, Y. H., Scholes, C. P. and King, T. E. (1983) Interaction in cytochrome *c* oxidase between cytochrome a_3 ligated with nitric oxide and cytochrome *a*. *J. Biol. Chem.* **258**: 5348-5351.

Maxwell, J. C. and Caughey, W. S. (1976) An infrared study of NO bonding to heme B and hemoglobin A. Evidence for inositol hexaphosphate induced cleavage of proximal histidine to iron bonds. *Biochemistry* **15**: 388-396.

Miller, L. M., Pedraza, A. J. and Chance, M. R. (1997) Identification of conformational substates involved in nitric oxide binding to ferric and ferrous myoglobin through difference Fourier transform infrared spectroscopy (FTIR). *Biochemistry* **36**: 12199-12207.

Moënne-Loccoz, P. (2007) Spectroscopic characterization of heme iron-nitrosyl species and their role in NO reductase mechanisms in diiron proteins. *Natl. Prod. Rep.* **24**: 610-620.

Moënne-Loccoz, P., Richter, O.-M. H., Huang, H. W., Wasser, I. M., Ghiladi, R. A., Karlin, K. D. and de Vries, S. (2000) Nitric oxide reductase from *Paracoccus denitrificans* contains an oxo-bridged heme/non-heme diiron center. *J. Am. Chem. Soc.* **122**: 9344-9345.

Mogi, T., Minagawa, J., Hirano, T., Sato-Watanabe, M., Tsubaki, M., Uno, T., Hori, H., Nakamura, H., Nishimura, Y. and Anraku, Y. (1998) Substitutions of conserved aromatic amino acid residues in subunit I perturb the metal centers of the *Escherichia coli bo*-type ubiquinol oxidase. *Biochemistry* **37**: 1632-1639.

Montenegro, A. C., Amorebieta, V. T., Slep, L. D., Martin, D. F., Roncaroli, F., Murgida, D. H., Bari, S. E. and Olabe, J. A. (2009) Three redox states of nitrosyl: NO^+, $NO^\bullet$, and NO^-/HNO interconvert reversibly on the same pentacyanoferrate(II) platform. *Angew. Chem. Int. Ed. Engl.* **48**: 4213-4216.

Nakamoto, K. (1997) Infrared and Raman spectroscopy of inorganic and coordination compounds. John Wiley and Sons, Inc. New York.A-B

Nelson, M. J. (1987) The nitric oxide complex of ferrous soybean lipoxygenase-1. Substrate, pH, and ethanol effects on the active-site iron. *J. Biol. Chem.* **262**: 12137-12142.

Nienhaus, K., Lamb, D. C., Deng, P. and Nienhaus, G. U. (2002) The effect of ligand dynamics on heme electronic transition band III in myoglobin. *Biophys. J.* **82**: 1059-1067.

Nocek, J. M., Kurtz, D. M., Jr., Sage, J. T., Xia, Y.-M., Debrunner, P., Shiemke, A. K., Sanders-Loehr, J. and Loehr, T. M. (1988) Nitric oxide adducts of the binuclear iron site of hemerythrin: spectroscopy and reactivity. *Biochemistry* **27**: 1014-1024.

Nordlund, P., Sjöberg, B.-M. and Eklund, H. (1990) Three-dimensional structure of the free radical protein of ribonucleotide reductase. *Nature* **345**: 593-598.

Novozhilova, I. V., Coppens, P., Lee, J., Richter-Addo, G. B. and Bagley, K. A. (2006) Experimental and density functional theoretical investigations of linkage isomerism in six-coordinate $\{FeNO\}^6$ iron porphyrins with axial nitrosyl and nitro ligands. *J. Am. Chem. Soc.* **128**: 2093-2104.

Obayashi, E., Takahashi, S. and Shiro, Y. (1998) Electronic structure of reaction intermediate of cytochrome P450nor in its nitric oxide reduction. *J. Am. Chem. Soc.* **120**: 12964-12965.

Oertling, W. A., Surerus, K. K., Einarsd'ottir, O., Fee, J. A., Dyer, R. B. and Woodruff, W. H. (1994) Spectroscopic characterization of cytochrome ba_3, a terminal oxidase from *Thermus thermophilus*: comparison of the a_3/Cu_B site to that of bovine cytochrome aa_3. *Biochemistry* **33**: 3128-3141.

Ohta, K., Muramoto, K., Shinzawa-Itoh, K., Yamashita, E., Yoshikawa, S. and Tsukihara, T. (2010) X-ray structure of the NO-bound Cu_B in bovine cytochrome *c* oxidase. *Acta Crystallogr. Sect. F Struct. Biol. Cryst. Commun.* **66**: 251-253.

Ohta, T., Kitagawa, T. and Varotsis, C. (2006) Characterization of a bimetallic-bridging intermediate in the reduction of NO to N_2O: a density functional theory study. *Inorg. Chem.* **45**: 3187-3190.

Orville, A. M. and Lipscomb, J. D. (1993) Simultaneous binding of nitric oxide and isotopically labeled substrates or inhibitors by reduced protocatechuate 3,4-dioxygenase. *J. Biol. Chem.* **268**: 8596-8607.

Ostermann, A., Waschipky, R., Parak, F. G. and Nienhaus, G. U. (2000) Ligand binding and conformational motions in myoglobin. *Nature* **404**: 205-208.

Ostermeier, C., Harrenga, A., Ermler, U. and Michel, H. (1997) Structure at 2.7 Å resolution of the *Paracoccus denitrificans* two-subunit cytochrome c oxidase complexed with an antibody FV fragment. *Proc. Natl. Acad. Sci. U.S.A.* **94**: 10547-10553.

Pearce, L. L., Bominaar, E. L., Hill, B. C. and Peterson, J. (2003) Reversal of cyanide inhibition of cytochrome *c* oxidase by the auxiliary substrate nitric oxide: an endogenous antidote to cyanide poisoning? *J. Biol. Chem.* **278**: 52139-52145.

Pereira, M. M., Sousa, F. L., Verissimo, A. F. and Teixeira, M. (2008) Looking for the minimum common denominator in haem-copper oxygen reductases: towards a unified catalytic mechanism. *Biochim. Biophys. Acta* **1777**: 929-934.

Pilet, E., Nitschke, W., Liebl, U. and Vos, M. H. (2007) Accommodation of NO in the active site of mammalian and bacterial cytochrome *c* oxidase aa_3. *Biochim. Biophys. Acta* **1767**: 387-392.

Pilet, E., Nitschke, W., Rappaport, F., Soulimane, T., Lambry, J. C., Liebl, U. and Vos, M. H. (2004) NO binding and dynamics in reduced heme-copper oxidases aa_3 from *Paracoccus denitrificans* and ba_3 from *Thermus thermophilus*. *Biochemistry* **43**: 14118-14127.

Pinakoulaki, E., Ohta, T., Soulimane, T., Kitagawa, T. and Varotsis, C. (2005) Detection of the His-heme Fe^{2+}-NO species in the reduction of NO to N_2O by ba_3-oxidase from *Thermus thermophilus*. *J. Am. Chem. Soc.* **127**: 15161-15167.

Pinakoulaki, E., Stavrakis, S., Urbani, A. and Varotsis, C. (2002) Resonance Raman detection of a ferrous five-coordinate nitrosylheme b_3 complex in cytochrome cbb_3 oxidase from *Pseudomonas stutzeri*. *J. Am. Chem. Soc.* **124**: 9378-9379.

Praneeth, V. K., Nather, C., Peters, G. and Lehnert, N. (2006) Spectroscopic properties and electronic structure of five- and six-coordinate iron(II) porphyrin NO complexes: Effect of the axial N-donor ligand. *Inorg. Chem.* **45**: 2795-2811.

Praneeth, V. K., Neese, F. and Lehnert, N. (2005) Spin density distribution in five- and six-coordinate iron(II)-porphyrin NO complexes evidenced by magnetic circular dichroism spectroscopy. *Inorg Chem* **44**: 2570-2572.

Proshlyakov, D. A., Pressler, M. A., DeMaso, C., Leykam, J. F., DeWitt, D. L. and Babcock, G. T. (2000) Oxygen activation and reduction in respiration: involvement of redox-active tyrosine 244. *Science* **290**: 1588-1591.

Puustinen, A., Bailey, J. A., Dyer, R. B., Mecklenburg, S. L., Wikstrom, M. and Woodruff, W. H. (1997) Fourier transform infrared evidence for connectivity between Cu_B and glutamic acid 286 in cytochrome bo_3 from *Escherichia coli*. *Biochemistry* **36**: 13195-13200.

Reddy, K. S., Angiolillo, P. J., Wright, W. W., Laberge, M. and Vanderkooi, J. M. (1996) Spectral splitting in the alpha ($Q_{0,0}$) absorption band of ferrous cytochrome *c* and other heme proteins. *Biochemistry* **35**: 12820-12830.

Reimann, J., Flock, U., Lepp, H., Honigmann, A. and Adelroth, P. (2007) A pathway for protons in nitric oxide reductase from *Paracoccus denitrificans*. *Biochim. Biophys. Acta* **1767**: 362-373.

Rein, H., Ristau, O. and Scheler, W. (1972) On the influence of allosteric effectors on the electron paramagnetic spectrum of nitric oxide hemoglobin. *FEBS Lett.* **24**: 24-26.

Rodrigues, R., Vicente, J. B., Felix, R., Oliveira, S., Teixeira, M. and Rodrigues-Pousada, C. (2006) *Desulfovibrio gigas* flavodiiron protein affords protection against nitrosative stress *in vivo*. *J. Bacteriol.* **188**: 2745-2751.

Rodriguez-Martin, Y., Hernandez-Molina, M., Sanchiz, J., Ruiz-Perez, C., Lloret, F., and Julve, M., (2003) Crystal structure and magnetic properties of two- and three-dimentioanl malonato-bridged manganese(II) complexes. *Dalton. Trans.* 2359-2365.

Rosenzweig, A. C., Frederick, C. A., Lippard, S. J. and Nordlund, P. (1993) Crystal structure of a bacterial non-heme iron hydroxylase that catalyzes the biological oxidation of methane. *Nature* **366**: 537-543.

Ruggiero, C. E., Carrier, S. M., Antholine, W. E., Whittaker, J. W., Cramer, C. J. and Tolman, W. B. (1993) Synthesis and structural and spectroscopic characterization of mononuclear copper nitrosyl complexes: models for nitric oxide adducts of copper proteins and copper-exchanged zeolites. *J. Am. Chem. Soc.* **115**: 11285-11298.

Rumbley, J. N., Furlong Nickels, E. and Gennis, R. B. (1997) One-step purification of histidine-tagged cytochrome bo_3 from *Escherichia coli* and demonstration that associated quinone is not required for the structural integrity of the oxidase. *Biochim. Biophys. Acta.* **1340**: 131-142.

Samples, C. R., Howard, T., Raushel, F. M. and DeRose, V. J. (2005) Protonation of the binuclear metal center within the active site of phosphotriesterase. *Biochemistry* **44**: 11005-11013.

Saraiva, L. M., Vicente, J. B. and Teixeira, M. (2004) The role of the flavodiiron proteins in microbial nitric oxide detoxification. *Adv. Microb. Physiol.* **49**: 77-129.

Schlichting, I. and Chu, K. (2000) Trapping intermediates in the crystal: ligand binding to myoglobin. *Curr. Opin. Struct. Biol.* **10**: 744-752.

Schneider, J. L., Carrier, S. M., Ruggiero, C. E., Young, V. G., Jr. and Tolman, W. B. (1998) Influences of ligand environment on the spectroscopic properties and disproportionation reaction of copper-nitrosyl complexes. *J. Am. Chem. Soc.* **120**: 11408-11418.

Serres, R. G., Grapperhaus, C. A., Bothe, E., Bill, E., Weyhermuller, T., Neese, F. and Wieghardt, K. (2004) Structural, spectroscopic, and computational study of an octahedral, non-heme $\{Fe\text{-}NO\}^{6\text{-}8}$ series: $[Fe(NO)(cyclam\text{-}ac)]^{2+/+/0}$. *J. Am. Chem. Soc.* **126**: 5138-5153.

Shafirovich, V. and Lymar, S. V. (2002) Nitroxyl and its anion in aqueous solutions: spin states, protic equilibria, and reactivities toward oxygen and nitric oxide. *Proc. Natl. Acad. Sci. U. S. A.* **99**: 7340-7345.

Shiro, Y., Fujii, M., Iizuka, T., Adachi, S., Tsukamoto, K., Nakahara, K. and Shoun, H. (1995) Spectroscopic and kinetic studies on reaction of cytochrome P450nor with nitric oxide - Implication for Its nitric oxide reduction mechanism. *J. Biol. Chem.* **270**: 1617-1623.

Silaghi-Dumitrescu, R., Coulter, E. D., Das, A., Ljungdahl, L. G., Jameson, G. N., Huynh, B. H. and Kurtz, D. M., Jr. (2003) A flavodiiron protein and high molecular weight rubredoxin from *Moorella thermoacetica* with nitric oxide reductase activity. *Biochemistry* **42**: 2806-2815.

Silaghi-Dumitrescu, R., Kurtz, D. M., Jr., Ljungdahl, L. G. and Lanzilotta, W. N. (2005) X-ray crystal structures of *Moorella thermoacetica* FprA. Novel diiron site structure and mechanistic insights into a scavenging nitric oxide reductase. *Biochemistry* **44**: 6492-6501.

Silaghi-Dumitrescu, R., Ng, K. Y., Viswanathan, R. and Kurtz, D. M., Jr. (2005) A flavo-diiron protein from *Desulfovibrio vulgaris* with oxidase and nitric oxide reductase activities. Evidence for an in vivo nitric oxide scavenging function. *Biochemistry* **44**: 3572-3579.

Soulimane, T., Buse, G., Bourenkov, G. P., Bartunik, H. D., Huber, R. and Than, M. E. (2000) Structure and mechanism of the aberrant ba_3-cytochrome *c* oxidase from *Thermus thermophilus*. *EMBO J.* **19**: 1766-1776.

Stevanin, T. M., Moir, J. W. and Read, R. C. (2005) Nitric oxide detoxification systems enhance survival of *Neisseria meningitidis* in human macrophages and in nasopharyngeal mucosa. *Infect. Immun.* **73**: 3322-3329.

Stevens, T. H., Brudvig, G. W., Bocian, D. F. and Chan, S. I. (1979) Structure of cytochrome a_3-Cu_B couple in cytochrome *c* oxidase as revealed by nitric oxide binding studies. *Proc. Natl. Acad. Sci. U.S.A.* **76**: 3320-3324.

Stong, J. D., Burke, J.M., Daly, P., Wright, P., and Spiro, T.G. (1980) Resonance Raman Spectra of Nitrosyl Heme Proteins and of Porphyrin Analogues. *J. Am. Chem. Soc.* **102**: 5815-5819.

Strube, K., de Vries, S. and Cramm, R. (2007) Formation of a dinitrosyl iron complex by NorA, a nitric oxide-binding di-iron protein from *Ralstonia eutropha* H16. *J. Biol. Chem.* **282**: 20292-20300.

Sulc, F., Immoos, C. E., Pervitsky, D. and Farmer, P. J. (2004) Efficient trapping of HNO by deoxymyoglobin. *J. Am. Chem. Soc.* **126**: 1096-1101.

Svensson-Ek, M., Abramson, J., Larsson, G., Tornroth, S., Brzezinski, P. and Iwata, S. (2002) The X-ray crystal structures of wild-type and EQ(I-286) mutant cytochrome *c* oxidases from *Rhodobacter sphaeroides*. *J. Mol. Biol.* **321**: 329-339.

Szabo, A. and Perutz, M. F. (1976) Equilibrium between six- and five-coordinated hemes in nitrosylhemoglobin: interpretation of electron spin resonance spectra. *Biochemistry* **15**: 4427-4428.

Thomas, J. W., Calhoun, M. W., Lemieux, L. J., Puustinen, A., Wikström, M., Alben, J. O. and Gennis, R. B. (1994) Site-directed mutagenesis of residues within helix VI in subunit I of the cytochrome bo_3 ubiquinol oxidase from *Escherichia coli* suggests that tyrosine 288 may be a Cu_B ligand. *Biochemistry* **33**: 13013-13021.

Thomas, M. R., Brown, D., Franzen, S. and Boxer, S. G. (2001) FTIR and resonance Raman studies of nitric oxide binding to H93G cavity mutants of myoglobin. *Biochemistry* **40**: 15047-15056.

Tocheva, E. I., Rosell, F. I., Mauk, A. G. and Murphy, M. E. P. (2004) Side-on copper-nitrosyl coordination by nitrite reductase. *Science* **304**: 867-870.

Tomita, T., Hirota, S., Ogura, T., Olson, J. S. and Kitagawa, T. (1999) Resonance Raman Investigation of Fe-N-O Structrue of Nitrosylheme in Myoglobin and Its Mutants. *J. Phys. Chem. B* **103**: 7044-7054.

Tsubaki, M. and Yu, N. T. (1982) Resonance Raman investigation of nitric oxide bonding in nitrosylhemoglobin A and -myoglobin: detection of bound N-O stretching and Fe-NO stretching vibrations from the hexacoordinated NO-heme complex. *Biochemistry* **21**: 1140-1144.

Tsukihara, T., Aoyama, H., Yamashita, E., Tomizaki, T., Yamaguchi, H., Shinzawa, I.-K., Nakashima, R., Yaono, R. and Yoshikawa, S. (1996) The whole structure of the 13-subunit oxidized cytochrome *c* oxidase at 2.8 Å. *Science* **272**: 1136-1144.

Varotsis, C., Ohta, T., Kitagawa, T., Soulimane, T. and Pinakoulaki, E. (2007) The structure of the hyponitrite species in a heme Fe-Cu binuclear center. *Angew. Chem. Int. Ed. Engl.* **46**: 2210-2214.

Vicente, J. B. and Teixeira, M. (2005) Redox and spectroscopic properties of the *Escherichia coli* nitric oxide-detoxifying system involving flavorubredoxin and its NADH-oxidizing redox partner. *J. Biol. Chem.* **280**: 34599-34608.

Vicente, J. B., Testa, F., Mastronicola, D., Forte, E., Sarti, P., Teixeira, M. and Giuffre, A. (2009) Redox properties of the oxygen-detoxifying flavodiiron protein from the human parasite *Giardia intestinalis*. *Arch. Biochem. Biophys.* **488**: 9-13.

Victor, B. L., Baptista, A. M. and Soares, C. M. (2009) Dioxygen and nitric oxide pathways and affinity to the catalytic site of rubredoxin:oxygen oxidoreductase from *Desulfovibrio gigas*. *J. Biol. Inorg. Chem.* **14**: 853-862.

Voegtli, W. C., Sommerhalter, M., Saleh, L., Baldwin, J., Bollinger, J. M., Jr. and Rosenzweig, A. C. (2003) Variable coordination geometries at the diiron(II) active site of ribonucleotide reductase R2. *J. Am. Chem. Soc.* **125**: 15822-15830.

Vogel, K. M., Kozlowski, P. M., Zgierski, M. Z. and Spiro, T. G. (1999) Determinants of the FeXO (X = C, N, O) vibrational frequencies in heme adducts from experiment and density function theory. *J. Am. Chem. Soc.* **121**: 9915-9921.

Vos, M. H., Borisov, V. B., Liebl, U., Martin, J. L. and Konstantinov, A. A. (2000) Femtosecond resolution of ligand-heme interactions in the high-affinity quinol oxidase *bd*: A di-heme active site? *Proc. Natl. Acad. Sci. U. S. A.* **97**: 1554-1559.

Vos, M. H., Lipowski, G., Lambry, J. C., Martin, J. L. and Liebl, U. (2001) Dynamics of nitric oxide in the active site of reduced cytochrome *c* oxidase aa_3. *Biochemistry* **40**: 7806-7811.

Wang, J., Takahashi, S., Hosler, J. P., Mitchell, D. M., Ferguson-Miller, S., Gennis, R. B. and Rousseau, D. L. (1995) Two conformations of the catalytic site in the aa_3-type cytochrome *c* oxidase from *Rhodobacter sphaeroides*. *Biochemistry* **34**: 9819-9825.

Wasser, I. M., de Vries, S., Moënne-Loccoz, P., Schroder, I. and Karlin, K. D. (2002) Nitric oxide in biological denitrification: Fe/Cu metalloenzyme and metal complex NO_x redox chemistry. *Chem. Rev.* **102**: 1201-1234.

Wasser, I. M., Huang, H. W., Moënne-Loccoz, P. and Karlin, K. D. (2005) Heme/non-heme diiron(II) complexes and O_2, CO, and NO adducts as reduced and substrate-bound models for the active site of bacterial nitric oxide reductase. *J. Am. Chem. Soc.* **127**: 3310-3320.

Watmough, N. J., Butland, G., Cheesman, M. R., Moir, J. W., Richardson, D. J. and Spiro, S. (1999) Nitric oxide in bacteria: synthesis and consumption. *Biochim. Biophys. Acta* **1411**: 456-474.

Wayland, B. B. and Olson, L. W. (1974) Spectroscopic studies and bonding model for nitric oxide complexes of iron porphyrins. *J. Am. Chem. Soc.* **96**: 6037-6041.

Westre, T. E., Di Cicco, A., Filipponi, A., Natoli, C. R., Hedman, B., Solomon, E. I. and Hodgson, K. O. (1994) Determination of the Fe-N-O Angle in $\{FeNO\}^7$ Complexes Using Multiple-Scattering EXAFS Analysis by GNXAS. *J. Am. Chem. Soc.* **116**: 6757-6768.

Whittington, D. A. and Lippard, S. J. (2001) Crystal structures of the soluble methane monooxygenase hydroxylase from *Methylococcus capsulatus* (Bath) demonstrating geometrical variability at the dinuclear iron active site. *J. Am. Chem. Soc.* **123**: 827-838.

Wildschut, J. D., Lang, R. M., Voordouw, J. K. and Voordouw, G. (2006) Rubredoxin:oxygen oxidoreductase enhances survival of *Desulfovibrio vulgaris* hildenborough under microaerophilic conditions. *J. Bacteriol.* **188**: 6253-6260.

Yap, L. L., Samoilova, R. I., Gennis, R. B. and Dikanov, S. A. (2007) Characterization of mutants that change the hydrogen bonding of the semiquinone radical at the QH site of the cytochrome bo_3 from *Escherichia coli*. *J. Biol. Chem.* **282**: 8777-8785.

Yap, L. L., Samoilova, R. I., Gennis, R. B. and Dikanov, S. A. (2006) Characterization of the exchangeable protons in the immediate vicinity of the semiquinone radical at the QH site of the cytochrome bo_3 from *Escherichia coli*. *J. Biol. Chem.* **281**: 16879-16887.

Yeung, N., Lin, Y. W., Gao, Y. G., Zhao, X., Russell, B. S., Lei, L., Miner, K. D., Robinson, H. and Lu, Y. (2009) Rational design of a structural and functional nitric oxide reductase. *Nature* **462**: 1079-1082.

Yonetani, T., Yamamoto, H., Erman, J. E., Leigh, J. S., Jr. and Reed, G. H. (1972) Electromagnetic properties of hemoproteins. V. Optical and electron paramagnetic resonance characteristics of nitric oxide derivatives of metalloporphyrin-apohemoprotein complexes. *J. Biol. Chem.* **247**: 2447-2455.

Yoshida, S., Hori, H. and Orii, Y. (1980) Photodissociation of cytochrome oxidase-nitric oxide at low temperatures. *J. Biochem. (Tokyo)* **88**: 1623-1627.

Yoshikawa, S., Shinzawa-Itoh, K., Nakashima, R., Yaono, R., Yamashita, E., Inoue, N., Yao, M., Fei, M. J., Libeu, C. P., Mizushima, T., Yamaguchi, H., Tomizaki, T. and Tsukihara, T. (1998) Redox-coupled crystal structural changes in bovine heart cytochrome *c* oxidase. *Science* **280**: 1723-1729.

Yu, A. E., Hu, S., Spiro, T. G. and Burstyn, J. N. (1994) Resonance Raman spectroscopy of soluble guanylyl cyclase reveals displacement of distal and proximal heme ligands by NO. *J. Am. Chem. Soc.* **116**: 4117-4118.

Zhang, Y., Pavlosky, M. A., Brown, C. A., Westre, T. E., Hedman, B., Hodgson, K. O. and Solomon, E. I. (1992) Spectroscopic and theoretical description of the electronic structure of the $S = 3/2$ nitrosyl complex of non-heme iron enzymes. *J. Am. Chem. Soc.* **114**: 9189-9191.

Zhao, X. J., Sampath, V. and Caughey, W. S. (1995) Cytochrome *c* oxidase catalysis of the reduction of nitric oxide to nitrous oxide. *Biochem. Biophys. Res. Commun.* **212**: 1054-1060.

Zhao, X. J., Sampath, V. and Caughey, W. S. (1994) Infrared characterization of nitric oxide bonding to bovine heart cytochrome *c* oxidase and myoglobin. *Biochem. Biophys. Res. Commun.* **204**: 537-543.

Zumft, W. G. and Frunzke, K. (1982) Discrimination of ascorbate-dependent nonenzymatic and enzymatic, membrane-bound reduction of nitric oxide in denitrifying *Pseudomonas perfectomarinus*. *Biochim. Biophys. Acta* **681**: 459-468.

BIOGRAPHICAL SKETCH

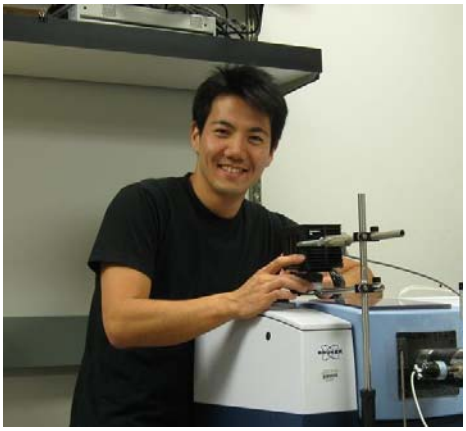

Takahiro Hayashi was born on July 19th, 1983, in Shizuoka prefecture, Japan. In 2006, he received B.S. degree in Biotechnology with emphasis in synthetic chemistry from Tokyo University of Agriculture of Technology. In the summer of 2006, he began his graduate studies in the Division of Environmental and Biomolecular Systems at Oregon Health and Science University.

Publications:

Hayashi T., Miner K.D., Yeung N., Lin Y-W., Lu Y., and Moënne-Loccoz P. Spectroscopic Characterization of Mononitrosyl Complexes in Heme-nonheme Diiron Centers within the Myoglobin Scaffold (Fe_BMb): Relevance to Denitrifying NO Reductase. *In preparation.*

Tran N.G., Kalyvas H., Skodje K.M., Hayashi T., Moënne-Loccoz P., Callan P.E., Shearer J., Kirschenbaum L.J., and Kim E. (2011) Phenol Nitration Induced by an $\{Fe(NO)_2\}^{10}$ Dinitrosyl Iron Complex. *J. Am. Chem. Soc.* **133**: 1184-1187.

Kommineni S., Yukl E., Hayashi T., Delepine J., Geng H., Moënne-Loccoz P., and Nakano M.M. (2010) Nitric Oxide Sensitive and Insensitive Interaction of *Bacillus subtillis* NsrR with a ResDE-controlled promoter. *Mol. Microbiol.* **78**: 1280-1293.

Hayashi T., Caranto J.D., Wampler D.A., Kurtz Jr. D.M., and Moënne-Loccoz P. (2010) Insights into the Nitric Oxide Reductase Mechanism of Flavo-diiron Proteins from a Flavin-free Enzyme. *Biochemistry,* **49**: 7040-7049.

Do L.H., Hayashi T., Moënne-Loccoz P., and Lippard S.J. (2010) Carboxylate as the Protonation Site in (Peroxo)diiron(III) Model Complexes of Soluble Methane Monooxygenase and Related Diiron Proteins. *J. Am. Chem. Soc.* **132**: 1273-1275.

Namuswe F., Hayashi T., Yunbo J., Kasper G.D., Narducci Sarjeant A.A., Moënne-Loccoz P., and Goldberg D.P. (2010) Influence of the Nitrogen Donors on Non-Heme

Iron Models of Superoxide Reductase: High-Spin Fe^{III}-OOR Complexes. *J. Am. Chem. Soc.* **132**: 157-167.

Friedle S., Kodanko J.J., Morys A.J., Hayashi T., Moënne-Loccoz P., and Lippard S.J. (2009) Modeling the Syn Disposition of Nitrogen Donors in Non-Heme Diiron Enzymes. Synthesis, Characterization, and Hydrogen Peroxide Reactivity of Diiron(III) Complexes with the Syn *N*-Donor Ligand H_2BPG_2DEV. *J. Am. Chem. Soc.* **131**: 14508-14520.

Jiang Y., Sivaramakrishnan S., Hayashi T., Cohen S., Moënne-Loccoz P., Shaik S., and Ortiz de Montellano P.R., (2009) Calculated and experimental spin state of seleno cytochrome P450. *Angew. Chem. Int. Ed.* **48**: 7193-7195.

Hayashi T., Lin M.T., Ganesan K., Chen Y., Fee J.A., Gennis R.B., and Moënne-Loccoz P. (2009) Accommodation of two diatomic molecules in cytochrome *bo_3*: insights into NO reductase activity in terminal oxidases. *Biochemistry* 48: 883-890.

Alontaga A.Y., Rodriguez J.C., Schönbrunn E., Becker A., Funke T., Yukl E.T., Hayashi T., Stobaugh J., Moënne-Loccoz P., and Rivera M. (2009) Structural characterization of the hemophore HasAp from *Pseudomonas aeruginosa*: NMR spectroscopy reveals protein-protein interactions between Holo-HasAp and hemoglobin. *Biochemistry* 48: 96-109.

Namuswe F., Kasper G.D., Sarjeant A.A., Hayashi T., Krest C.M., Green M.T., Moënne-Loccoz P., and Goldberg D.P. (2008) Rational tuning of the thiolate donor in model complexes of superoxide reductase: direct evidence for a trans influence in Fe(III)-OOR complexes. *J. Am. Chem. Soc.* 130: 14189-14200.

Tamada M., Ueda S., Hayashi T., and Ohno H. (2008) Thermally stable polymer gel electrolytes composed of branched polyimide and ionic liquid/zwitterion mixture prepared by in situ polycondensation. *Chem. Lett.* **37**: 86-87.

Hayashi T., Lin I.J., Chen Y., Fee J.A., and Moënne-Loccoz P. (2007) Fourier transform infrared characterization of a Cu_B-nitrosyl complex in cytochrome *ba_3* from *Thermus thermophilus*: relevance to NO reductase activity in heme-copper terminal oxidases. *J. Am. Chem. Soc.* **129**: 14952-14958.

Tamada M., Hayashi T., and Ohno H. (2007) Improved solubilization of pyromellitic dianhydride and 4,4'-oxydianiline in ionic liquid by the addition of zwitterion and their polycondensation. *Tetrahedron Lett.* **48**: 1553-1557.